
Università degli Studi di Udine
Dottorato di Ricerca in
Scienze dell'Ingegneria Energetica e Ambientale
XXXVI Ciclo

Technische Universität Wien
Doktoratsstudium der
Technische Wissenschaften Maschinenbau


# Direct numerical simulation of capillary waves forced by hydrodynamic turbulence


**Georgios Giamagas**


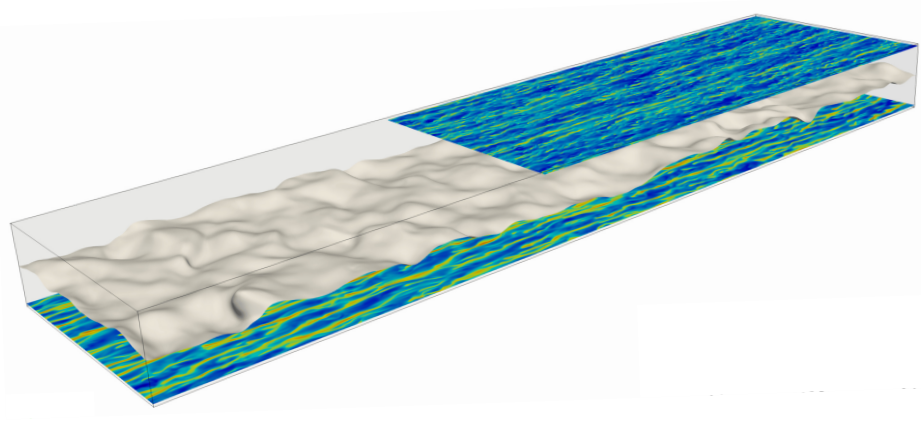

**BOARD MEMBERS**

| | |
|---|---|
| Prof. Guillaume Ducrozet | Reviewer |
| Prof. Luc Deike | Reviewer |
| Prof. Miguel Onorato | Committee member |
| Prof. Vasilis Bontozoglou | Committee member |
| Prof. Cristian Marchioli | Supervisor |
| Dr. Francesco Zonta | Supervisor |
| Prof. Alfredo Soldati | Co-Supervisor |

Author's e-mail:
giamagas.georgios@spes.uniud.it
george.giamagas@tuwien.ac.at

Author's address:
Dipartimento Politecnico di Ingegneria e Architettura
Università degli Studi di Udine
Via delle Scienze, 206
33100 Udine, Italy
Web: diegm- University of Udine

Institute of Fluid Mechanic and Heat Transfer
Technische Universität Wien
Getreidemarkt 9/E322
1060 Wien, Austria
Web: ISW - TU Wien

Cover:
Snapshot of the interface deformation and the flow topology from a two-layer turbulent flow simulation. Capillary waves can be seen at the interface between the two immiscible layers. The fluid in the upper half of the channel has a viscosity that is 50 % lower than that of the fluid in the lower half of the channel. The near-wall turbulence streaks are also made visible through a colormap that is based on the value of the streamwise component of the velocity vector. The streaks near the top wall of the channel are shorter and closer to each other compared to those near the bottom wall. This increase of turbulence activity in the top layer compared to the bottom layer is a direct effect of the viscosity mismatch between the two layers.

# Abstract

In this thesis, the turbulent flow of two liquid layers inside a wall-bounded domain is investigated by means of numerical simulation. The main interest of this work lies on the interaction between the capillary waves that are generated at the interface between the two liquid layers and the surrounding hydrodynamic turbulence. The flow field is resolved by means of Direct Numerical Simulation (DNS) with resolution down to the smallest flow scale (Kolmogorov scale). The interface deformation is captured using a Phase-Field Method (PFM). The first case that is examined is that of a pressure-driven flow of two liquids occupying the same volume inside a rectangular channel. Two parametric studies are preformed in order to study, first the effects of the viscosity contrast between the two fluid layers and second the effects of the surface tension at the interface. The capillary wave regimes that emerge at the interface are analysed by means of space-time spectral analysis and the results are compared to previous theoretical and experimental predictions of the spectral slope across different scales. Two-dimensional frequency-wavenumber spectra show that the waves propagate according to the linear dispersion relation. One-dimensional frequency and wavenumber spectra show that at larger wave scales, where turbulent forcing is not present, a scaling indicating an equipartition of energy between wave modes takes place. This observation is in agreement with the theoretical prediction for the behaviour of the capillary wave spectrum at scales larger than the forcing scale. At smaller scales, where turbulent forcing takes place, an early departure from the theoretically predicted inertial range slope to a steeper slope indicating a sharp decrease of wave energy at the shorter waves scales occurs near the Kolmogorov-Hinze scale, which expresses the local balance between inertial and surface tension forces. The second case that is examined is that of the pressure-driven flow of a thin laminar layer over a thick turbulent layer inside a rectangular channel. In this case, a single parametric study is performed to study the effect of the viscosity ratio, which is increased up to two orders of magnitude compared to the reference case with matched viscosities between the layers. This dramatic increase in the viscosity of the thin layer is catalytic to the shape and dynamics of the waves. In particular, instead of a set of waves of different wavelengths that propagate according to the linear dispersion relation that are observed in the matched viscosity case, the waves in the high viscosity cases are regular and two-dimensional, while they are purely advected with the mean velocity of the flow. Finally, a multiple resolution strategy is also presented. This technique allows for a selective increase of the resolution level of the phase-field transport equation, while keeping the resolution level of the momentum equations constant. This approach is validated and tested with both a two-dimensional and a three-dimensional flow configuration and is found to significantly increase the computation efficiency in terms of time and memory usage.

# Contents

# Introduction

## Introduction

Waves at the interface between two fluids are a common occurrence in every day life. These dynamic oscillations of the fluid-fluid interface are the result of the perturbation of the initially undisturbed interface caused by an external force and of a restoring force, which acts to restore the interface back to its equilibrium position. In nature, waves can be generated by the perturbation of the interface by random oscillations of the pressure field in the vicinity of the interface induced by the turbulent flow in the bulk of one or both of the fluid phases, like in the case of wind wave generation at the air-sea interface. Another example is that of waves generated due to the perturbations of the interface induced by the oscillation of a solid body, such as the wave maker of a wave tank during a laboratory experiment. In general, waves can be classified in two categories depending on the nature of the restoring force. Capillary waves are those waves for which the dominant restoring force is the surface tension force, while gravity waves are those waves for which the dominant restoring force is gravity. When the wind begins to blow above the surface of the ocean, short wave ripples of few centimetres appear first. At these small scales the effect of surface tension is dominant and that of gravity negligible. These are capillary waves. If the wind continuous to blow, the waves grow longer until gravity forces become predominant. The effect of surface tension is negligible compared to that of gravity for waves with lengths of the order of one meter. Another case, where the effect of gravity can be negligible or even absent regardless of the wave size is that of the waves forming at the interface between two liquids, where unlike in the air-water case, the densities of the two fluids are very similar. The most characteristic example of two such fluids is that of oil and water. In such a setting, surface tension can act as the sole restoring force, in which case the waves are pure capillary waves. The study of capillary waves generated at the interface of a two-layer oil-water flow, due to forcing by hydrodynamic turbulence in the bulk of the two layers, is the main focus of the present work.

Many applications of the petroleum industry are based on the two-phase flow of oil and water. Oil and water are a particular case of liquid-liquid flow given that the density mismatch between the two is rather low. In many practical instances, crude oil flows together with water inside pipelines/channels, since water is not only used to lift up crude oil from wells, but also directly injected into oil pipelines so to lubricate the flow and favour the oil transportation [1, 2, 3, 4]. In this case, at high flow rates, the flow becomes dispersed with droplets of oil forming inside the water layer and droplets of water inside the oil layer. However, at lower flow rates the flow remains stratified and the interface is characterized by the presence of capillary waves [5, 6, 7]. To optimise the process of oil transportation pipelines must be designed to ensure large flowrates, and at the same time limiting the friction losses and preventing the oil-water mixing (which would require more intense process/separation operations). A fundamental un-

derstanding of the interaction between capillary waves and hydrodynamic turbulence is a critical milestone towards this goal.

The experimental work on stratified oil-water flow inside pipes and channels is vast and old. However, most of these investigations are limited to the measurement of integral flow properties, such as pressure gradient and flow rate, without a detailed time and space description of the entire flow field and at the same time of the liquid-liquid interface deformation [8]. Indeed, the development of optical methods that are able to distinguish among the different phases and thus track the interface deformation, while at the same time providing measurements of the three-dimensional velocity fields is a formidable task. Despite these difficulties, significant progress has been made over the years thanks to the advancement of experimental techniques and the carefully designed experiments [9, 5]. On the other hand, the nonlinear interaction among short capillary ripples of different lengths on a gas-liquid interface (typically air-water) has been extensively studied experimentally [10, 11, 12, 13, 14]. However, in all of these studies the waves are generated by means of mechanical forcing induced by wave makers, in carefully controlled quiescent background flow environments, so to prevent any hydrodynamic turbulence, either in the air or in the water side, from perturbing the interface.

Numerical simulations offer an alternative path to study this type of problem. Many different Computational Fluid Dynamics (CFD) techniques have been used in the past, mainly in the context of petroleum engineering, to study stratified oil-water flow [15, 16, 17, 18]. Most of these approaches are based on Reynolds Averaged Navier-Stokes (RANS) or Large Eddy Simulation (LES), which are able to capture only the mean or integral properties of the flow field, while lacking the resolution level required to fully characterize the two-phase flow system interactions at the interface deformation scales, a shortcoming that is often bypassed via the use of empirical or phenomenological models [19, 20, 21]. However, it is precisely the interaction at those scales that determines the amount of momentum, mass and heat transfer between the two phases. In addition, while the interaction among random waves of different scales (so called wave-turbulence) has received a lot of attention it has been mostly studied (similarly to the experimental works) in isolation from the effect of a surrounding turbulent flow. In particular, a commonly employed approach to study wave-turbulence is the use of potential flow theory, which neglects any effects of realistic dissipation and/or forcing on the wave field. Indeed, wave-turbulence has been studied in the past by means of simulations based on potential flow theory solvers [23] or expansions of the hamiltonian of the free surface [22]. An exception to this is the study of Deike et al. [24], which reports the solution of the fully-resolved Navier-Stokes equations for two phases of air and water. However, even in this case the interface excitation is assumed to be the result of narrow-band low frequency forcing in an initially quiescent surrounding flow configuration. Finally, preliminary fully-resolved simulations of two-phase turbulent flow giving rise to interfacial waves have been performed in a limited number of studies [25, 26, 27, 28, 29], which are all related to the air-water flow scenario. Therefore, the interaction between hydrodynamic turbulence and waves is a field that remains largely unexplored, especially so in liquid-liquid flows, where a complete space-time description of the wave dynamics is still lacking in literature.

Direct Numerical Simulation (DNS) comes as an alternative tool to the experimental

study and to potential flow theory based solvers. The numerical databases obtained by means of DNS are oftentimes more complete than experimental data, since they give access to space-time descriptions of the flow and wave fields. More importantly, DNS with accurate description of both the turbulent flow field and the wave properties is perhaps the only presently available tool for exploring the dynamics of the interaction between waves and hydrodynamic turbulence, while considering realistic forcing and dissipation conditions. However, performing DNS of multiphase or multicomponent systems is extremely challenging. In particular, the physical mechanisms that control the dynamic evolution of the flow are intriguing, since they are driven by the interplay between inertial, capillary and viscous forces over multiple time and length scales. From a numerical point of view, the dynamics of a deformable interface that continuously changes shape must be captured/described. Thanks to the availability of computational resources and the advancement of numerical methods during recent years, the simulation of two-phase flows at moderate Reynolds numbers has become feasible [30, 4, 31, 32]. In literature, different methods are available that can describe the interface topology and the evolution of a multiphase flow system with a satisfying level of accuracy [33]. These methods can be roughly divided into two categories: interface tracking methods, such as the Front-Tracking (FT) method and the Immersed Boundary Method (IBM), and interface capturing methods, such as the Volume Of Fluid (VOF) method, the Level-Set (LS) method and the Phase-Field Method (PFM). Each of these methods has its own strength/weakness points. In this work, the problem of wall-bounded turbulent flows of two immiscible liquid layers is explored using a coupled DNS-PFM approach, in order to resolve the Navier-Stokes equations down to the smallest flow scale and to capture the deformation of the interface.

# Thesis outline

## Thesis outline

- **Chap. 1: Methodology**
  The theoretical framework of the Phase-Field Method (PFM) that is used to capture the interface deformation is introduced. The coupling of the phase-field transport equation to the governing equations of the fluid flow is described. The solution procedure, based on the Direct Numerical Simulation (DNS) of the Navier-Stokes equations, is presented together with the numerical scheme used to discretize the equations in space and in time. A memory and time efficient multiple resolution strategy for the selective increase of the resolution level of the phase-field transport equation is also presented. The code implementation in terms of parallelization strategies and techniques to obtain time and space resolved interface statistics is discussed. Finally, the validation of the code via simulation benchmarks is reported.

- **Chap. 2: Capillary waves in two-layer oil-water channel flow**
  The problem of two-layer oil-water turbulent flow in a rectangular channel is examined. Two parametric studies are performed, the first based on the variation of the viscosity of one fluid layer and the second based on the variation of surface tension. The generated capillary wave regimes are studied by means of space-time spectral analysis. The energy of the mean and fluctuating flow field is studied by means of an energy-box analysis. Finally, the wave energy is studied by means of an estimation of the total wave energy and an energy balance for the estimation of the energy flux across the wave spectrum is proposed.

- **Chap. 3: Channel flow of thick turbulent layer over thin laminar layer**
  The flow of a thick turbulent layer over a thin laminar layer in a channel at a variable viscosity ratio is examined. The mean and the fluctuating flow field modifications due to the change of viscosity are studied by means of space-time averaged statistics. The interface deformation is studied by means of space-time spectral analysis.

# 1

# Methodology

**Reproduced in part from:**
M. Schenk, G. Giamagas, A. Roccon, F. Zonta & A. Soldati, (2023) *Computationally efficient and interface accurate dual-grid phase-field simulation of turbulent drop-laden flows*, J. Fluids Eng. (in preparation)

In this chapter, the methodology employed for the simulation of the dynamics of turbulent multiphase flow systems is presented. The simulations performed in this thesis are based on an in-house code [34, 35, 31], in which Direct Numerical Simulation (DNS) of turbulence is coupled with a Phase-Field Method (PFM), which is used to account for the presence of more than one fluid phases. The code, which employs a pseudo-spectral technique to solve the governing equations of the fluid motion, is written in Fortran 2003 and is parallelised using a pure Message Passing Interface (MPI) paradigm. This method guarantees accurate solutions, and the possibility of using massively parallel solvers. High Performance Computing (HPC) with a large number of processors (cores) can thus be utilized to complete simulations within reasonable amounts of time. The following sections constitute a review of the main features of the method. In particular, in Sect. 1.1 the main framework and equations of the PFM that is used to capture the deformation of the interface between different fluids are introduced, while in Sect. 1.2 the governing equations of the flow hydrodynamics, as well as their coupling to the PFM equations is presented. After dimensionless equations are obtained in Sec. 1.3, the discretization of the equations and the solution procedure are presented in Sect. 1.4. In Sect. 1.5 the key elements of the multiple grid resolution strategy, which has been developed in order to increase the time and memory performance of the method are presented. Sect. 1.6 discusses the key features of the code implementation in terms of parallelization strategy and the techniques employed for the reconstruction of the interface during the simulation run time. Finally, in the last section, Sect. 1.7, two benchmarks for the validation of the code are reported, namely a two-layer pressure-driven laminar flow of fluids with different thermophysical properties and the deformation of a single droplet subjected in a shear laminar flow.

## 1.1 Interface capturing via phase-field method

The Phase-Field Method (PFM) belongs to the family of interface capturing methods, other members of this family being the Volume of Fluid (VoF) [36] and the Level Set (LS) method [37]. In contrast to interface tracking methods, such as the Front Tracking (FT) method [38], which track explicitly the interface deformation using Lagrangian point markers, interface capturing methods define the interface implicitly via a marker (colour) function representing the local concentration of each phase in the domain. This approach is purely Eulerian, which makes this class of methods more efficient in terms of algorithm parallelization and scalability. The marker function in the PFM is called phase-field, $\phi$. For the case of two-phase flow, $\phi$ takes constant values in the bulk of the two phases and undergoes a continuous transition across a transition layer of finite thickness between the phases. The PFM was initially developed by Cahn and Hillard [39, 40, 41] to study the spontaneous separation of two immiscible fluid phases, a process known as "spinodal decomposition" and it was later generalized for the study of incompressible multiphase flow systems by introducing an advection term and therefore coupling the phase-field to the flow field [42, 43]. The modified Cahn-Hillard equation after the addition of the advection term, used to describe the transport of the phase-field, is expressed as:

$$\frac{\partial \phi}{\partial t} + \mathbf{u} \cdot \nabla \phi = \mathcal{M}_\phi \nabla^2 \mu_\phi \tag{1.1}$$

where $\mathbf{u} = (u, v, w)$ is the velocity vector. $\mathcal{M}_\phi$ is the mobility (Onsager) coefficient and $\mu_\phi$ is the chemical potential. The chemical potential is obtained as the variational derivative of a Ginzburg-Landau free-energy functional, $\mathcal{F}[\phi, \nabla\phi]$[44, 43].

$$\mu_\phi = \frac{\delta \mathcal{F}[\phi, \nabla\phi]}{\delta \phi} \tag{1.2}$$

For a system of two immiscible fluids (e.g. oil and water) the free energy functional can be expressed as the sum of two contributions, the first representing the bulk free energy, $f_0$, which is associated to the tendency of the fluids to separate in pure phases, and the mixing free energy, $f_i$, which is the energy stored in the transition layer.

$$\mathcal{F}[\phi, \nabla\phi] = \int_\Omega (f_0(\phi) + f_i(\nabla\phi)) d\Omega \tag{1.3}$$

where $\Omega$ stands for the domain considered.
The two contributions can be expressed as functions of the phase-field, $\phi$, as follows:

$$f_0(\phi) = \frac{\alpha}{4}\left(\phi - \sqrt{\frac{\beta}{\alpha}}\right)^2 \left(\phi + \sqrt{\frac{\beta}{\alpha}}\right)^2 \tag{1.4}$$

$$f_i(\nabla\phi) = \frac{\kappa}{2}|\nabla\phi|^2 \tag{1.5}$$

with the two parameters $\alpha$ and $\beta$ being both constant and depending on the thermodynamic properties of the bulk phases. Eq. 1.4 is a double-well potential function with its two minima at $\phi = \pm\sqrt{\beta/\alpha}$, as shown in Fig. 1.1a. Eq. 1.5 shows that the mixing

term is proportional to the gradient of the phase, $\phi$ and therefore it is maximum at the interface and zero in the bulk of the phases, as shown in Fig. 1.1b. The positive constant $\kappa$ determines the magnitude of surface tension.

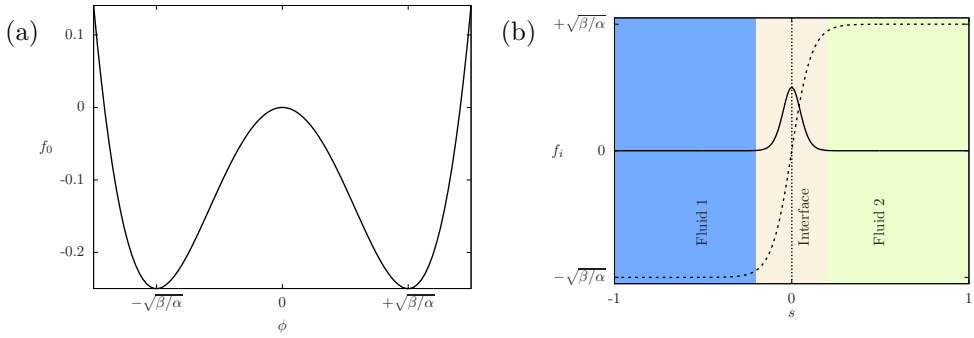


FIGURE 1.1 – In panel (a) the bulk free energy, $f_0$ is shown as a function of $\phi$. The two minima are located at $\phi = \pm\sqrt{\beta/\alpha}$ corresponding to the bulk concentrations of the two phases. In panel (b) the mixing free energy, $f_i$ is shown as a function of the interface normal coordinate $s$. The equilibrium profile of the phase-field is also shown with a black dashed line. The interface between the two fluids, which is identified as the $\phi = 0$ iso-contour, is located at $s = 0$ and is shown with a black dotted line.

The chemical potential can thus be expressed as a function of the phase-field by taking the variational derivative of the free energy functional, $\mathcal{F}[\phi, \nabla\phi]$.

$$\mu_\phi = \frac{\delta\mathcal{F}\left[\phi, \nabla\phi\right]}{\delta\phi} = \alpha\phi^3 - \beta\phi - \kappa\nabla^2\phi. \tag{1.6}$$

Thermodynamic equilibrium is established when the chemical potential is constant throughout the whole domain or $\nabla\mu_\phi = 0$. The corresponding equilibrium profile of the phase-field for a flat interface is then determined as:

$$\phi = \sqrt{\frac{\beta}{\alpha}}\tanh\left(\frac{s}{\sqrt{2}\xi}\right) \tag{1.7}$$

where $\xi = \sqrt{\kappa/\beta}$ is a measure of the thickness of the transition layer and $s$ is a coordinate normal to the interface. The equilibrium profile shows that the phase-field is constant in the bulk of the phases ($s \to \pm\infty$) and undergoes a smooth transition according to a hyperbolic tangent profile across the transition layer.
Finally, the surface tension, $\sigma$ for the two-fluid system is obtained based on the integral of the free energy functional across the transition layer [44, 43, 45].

$$\sigma = \frac{\beta\kappa}{\alpha}\int_{-\infty}^{+\infty}\mathcal{F}[\phi, \nabla\phi]ds \tag{1.8}$$

where upon using the equilibrium profile described by Eq. 1.7 , the integration yields:

$$\sigma = \frac{2\sqrt{2}}{3}\frac{\beta\kappa}{\alpha\xi} \tag{1.9}$$

The main advantage of the PFM is the accurate description of the interface topology and curvature without relying on specific advection schemes to reconstruct the interface shape after each computational step [46]. In addition, the method can implicitly handle arbitrary topological changes of the interface shape, such as breakup and coalescence phenomena. The main disadvantages of the method are coarsening, shrinkage and misrepresentation of thermo-physical properties. Coarsening is associated with the continuous interface assumption, since thanks to the finite-thickness transition layer between the different phases, all topological changes taking place at a scale smaller than the transition layer thickness are not completely captured. In addition, phenomena like molecular diffusion that naturally take place at scales of the order of $O(10^{-8}m)$ are introduced into a larger scale. In the case of multiphase turbulent flow simulations, the smallest resolved scale is close to the smallest flow scale, which is of the order of the Kolmogorov scale, $O(10^{-4}m)$ [47]. Therefore, the smooth transition of the thermo-physical properties and surface tension forces across the interface layer should ideally occur at a sharp interface limit with respect to the flow scales. Note that this is mainly a drawback of using the PFM in the context of multiphase turbulent flow simulations, where the limited available computational resources need to be focused on the resolution of the flow scales ranging from the integral scale of the problem down to the Kolmogorov scale. Shrinkage is associated to mass leakages between the different phases due to the deviation of the phase-field from the equilibrium profile followed by numerical diffusion of one phase into the other in order to restore the profile [49, 50]. Misrepresentation of thermophysical properties is another effect of the deviation of the phase-field from its equilibrium profile, since the properties of each fluid are dependent on the local concentration of the phase-field, fluctuations of the phase-field are also propagated to the local values of the thermophysical properties. Despite these drawbacks, the method has shown convergence to the sharp interface limit for problems involving turbulent multiphase flow, mixing, nucleation, enhanced heat transport, and liquid-vapor phase separation [48]. In the present formulation of the method, mass conservation can be enforced in two ways, by a straight-forward increase of the grid resolution and thus the reduction of the transition layer thickness and/or by applying special techniques that correct the equilibrium profile across the transition layer during the course of the simulation [51, 52]. More generally, shrinkage can also be alleviated with the adoption of different bulk free energy functionals, such as the one proposed by Van der Waals [53], which goes to infinity moving further from the value of the bulk concentrations of the two phases. This approach however, introduces discontinuities that can lead to less stable numerical schemes. A multiple resolution strategy to improve the performance of the DNS-PFM scheme by selectively increasing the grid resolution of the phase-field transport equation is presented in Sec. 1.5.

## 1.2 Hydrodynamics

Solving the phase-field transport equation, the temporal and spatial behaviour of the phase-field, $\phi$ is determined. However, the Cahn-Hilliard equation is coupled to the flow field, $\mathbf{u}$ through the advection term and therefore the solution of the phase-field implies an a-priori knowledge of the flow velocity. Therefore the governing equations of

the incompressible fluid flow, which are the continuity and the Navier-Stokes equations need to be solved in advance. Note that the validity of the continuity equation for the flow field can also be demonstrated in the case of a two-phase fluid system [54]. These equations are expressed as follows:

$$\nabla \cdot \mathbf{u} = 0 \tag{1.10}$$

$$\rho(\phi)\left(\frac{\partial \mathbf{u}}{\partial t} + \mathbf{u} \cdot \nabla \mathbf{u}\right) = -\nabla p + \nabla \cdot \left[\mu(\phi)\left(\nabla \mathbf{u} + \nabla \mathbf{u}^T\right)\right] + \rho(\phi)\,\mathbf{g} + \nabla \cdot (\overline{\tau_{\mathbf{c}}}\kappa) \tag{1.11}$$

where $\mathbf{u} = (u, v, w)$ is the velocity vector and $\nabla p$ is the pressure gradient. $\mathbf{g}$ is the accelaration due to gravity. $\mu(\phi)$ and $\rho(\phi)$ are the dynamic viscosity and the density distribution inside the domain, respectively. An one-fluid approach is adopted here, where the Navier-Stokes equations are solved over the whole domain, which includes both fluid phases [31]. In this way, the boundary conditions at the interface between the two fluids, namely the continuity of the shear stress, as well as the jump condition for the normal stress due to the action of surface tension, are implicitly satisfied. The latter is achieved via the introduction of an additional term at the right hand side of Eq. 1.11, accounting for capillary forces at the interface between the two fluids. Note that this term further couples the Navier-Stokes equations to the Cahn-Hilliard equation. $\overline{\tau_{\mathbf{c}}} = |\nabla\phi|^{\mathbf{2}} - \nabla\phi \otimes \nabla\phi$ is the Korteweg tensor, which accounts for the interface shape and curvature [55] and the positive constant $\kappa$ defines the magnitude of surface tension. The density and the viscosity are defined as linear functions of the phase-field. Hence, they are constant in the bulk of the two phases and undergo a smooth transition following the hyperbolic tangent phase-field profile across the transition layer between the phases. The following ratios between the bulk properties of the two fluids, $\mu_1, \rho_1$ and $\mu_2, \rho_2$, can be defined:

$$\rho_r = \frac{\rho_1}{\rho_2} \quad , \quad \mu_r = \frac{\mu_1}{\mu_2} \tag{1.12}$$

The viscosity and density profiles as functions of the phase-field and the above ratios are then given by:

$$\rho(\phi) = \rho_2\left[1 + \frac{\rho_r - 1}{2}\left(\frac{\phi}{\sqrt{\beta/\alpha}} + 1\right)\right] \tag{1.13}$$

$$\mu(\phi) = \mu_2\left[1 + \frac{\mu_r - 1}{2}\left(\frac{\phi}{\sqrt{\beta/\alpha}} + 1\right)\right] \tag{1.14}$$

A typical viscosity profile as function of the interface-normal coordinate, $s$ is sketched in Fig. 1.2 for two different values of the viscosity ratio.

## 1.3 Dimensional analysis

All simulations in this work are performed considering a three-dimensional plane channel geometry, a two-dimensional view of which is shown in Fig. 1.3. The channel is

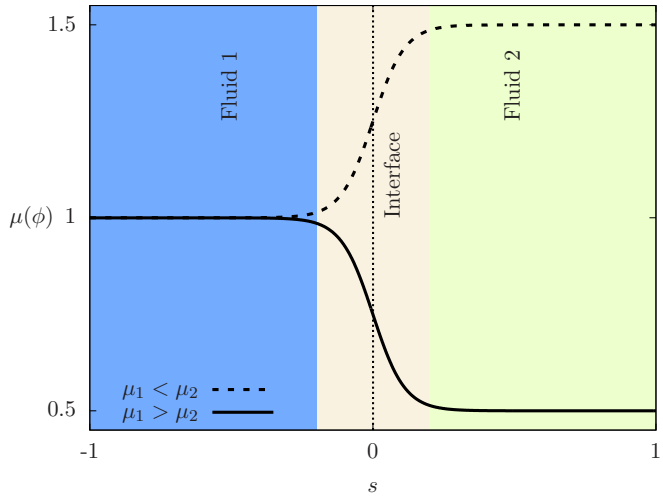


FIGURE 1.2 – Viscosity profile across the two fluid phases separated by a flat interface as a function of the interface normal coordinate $s$, for two different values of the viscosity ratio.

bounded by two parallel walls located at $z = \pm h$, with $h$ being the half height of the channel. The channel half height is selected to be the characteristic length scale of the problem. A characteristic velocity scale can be chosen depending on the flow scenario at hand. For shear-driven flow (Couette flow) with either one or two channel walls moving at a constant speed, the wall velocity, $u_w$ can be used as reference, while for pressure-driven flow (Poiseuille flow) the friction velocity, $u_\tau$ is commonly used, defined as $u_\tau = \sqrt{\tau_w/\rho_2}$, with $\tau_w$ being the shear stress at the wall and $\rho_2$ the density of the reference fluid phase. The absolute value of the phase-field at the bulk of the two phases can be used to non-dimensionalize the phase-field. The following dimensionless quantities can then be introduced:

$$\mathbf{x}^- = \frac{\mathbf{x}}{h}, \qquad \mathbf{u}^- = \frac{\mathbf{u}}{u_\tau}, \qquad t^- = \frac{t u_\tau}{h}, \qquad \phi^- = \frac{\phi}{\sqrt{\beta/\alpha}} \tag{1.15}$$

where $\mathbf{x} = (x, y, z)$ is the position, $\mathbf{u} = (u, v, w)$ is the fluid velocity and $t$ is time. The minus superscript is used to denote dimensionless quantities.
The above scaling system is typically referred to as outer units system. Another system that is commonly used in the context of wall-bounded turbulent flows is the inner or wall units scaling system [56], where the kinematic viscosity of the reference fluid, $\nu = \mu_2/\rho_2$ is used to obtain non-dimensional quantities as follows:

$$\mathbf{x}^+ = \frac{\mathbf{u}_\tau \mathbf{x}}{\nu}, \qquad \mathbf{u}^+ = \frac{\mathbf{u}}{u_\tau}, \qquad t^+ = \frac{t u_\tau^2}{\nu}, \qquad \phi^+ = \frac{\phi}{\sqrt{\beta/\alpha}} \tag{1.16}$$

Both of these systems are used throughout this work. All equations are solved in outer units, while wall units are used to renormalize quantities that are associated with the statistics of the turbulent flow fields.
The non-dimensional fluid viscosity and density are defined as:

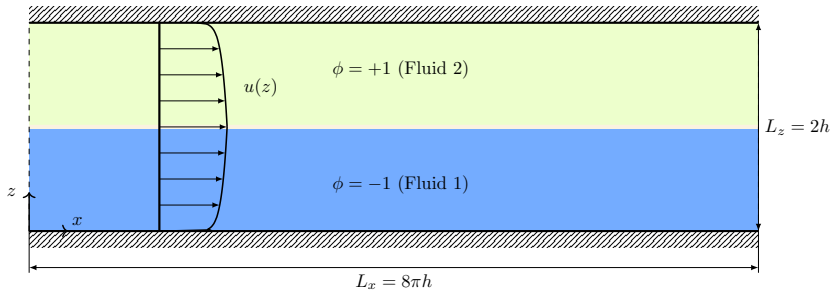


FIGURE 1.3 – Geometry of the channel used in the simulations. Two walls are present along the $z$ axis, wall-normal direction. The channel height is $L_z = 2h$, its length is $L_x = 8\pi h$ and its width $L_y = 2\pi h$ (not shown here). Periodic boundary conditions are applied along the $x$ and $y$ directions, while no-slip boundary conditions are applied on the two walls.

$$\rho^-(\phi^-) = \frac{\rho(\phi)}{\rho_2} = 1 + \frac{\rho_r - 1}{2}\left(\phi^- + 1\right) \tag{1.17}$$

$$\mu^-(\phi^-) = \frac{\mu(\phi)}{\mu_2} = 1 + \frac{\mu_r - 1}{2}\left(\phi^- + 1\right) \tag{1.18}$$

The continuity equation and the Navier-Stokes equations are expressed in dimensionless form as:

$$\nabla \cdot \mathbf{u}^- = 0 \tag{1.19}$$

$$\begin{aligned} \rho^-(\phi^-)\left(\frac{\partial \mathbf{u}^-}{\partial t^-} + \mathbf{u}^- \cdot \nabla \mathbf{u}^-\right) &= -\nabla p^- + \frac{1}{Re_\tau}\nabla \cdot \left[\mu^-(\phi^-)\left(\nabla \mathbf{u}^- + \nabla \mathbf{u}^{-T}\right)\right] + \\ &+ \frac{1}{Fr^2}\rho^-(\phi^-)\mathbf{g}^- + \frac{3}{\sqrt{8}}\frac{Ch}{We}\nabla \cdot \left(\overline{\tau_c}^-\right) \end{aligned} \tag{1.20}$$

where the pressure is made dimensionless as $p^- = p/\rho u_\tau^2$. The following dimensionless parameters appear in Eq. 1.20:

$$Re_\tau = \frac{\rho_2 u_\tau h}{\mu_2}, \qquad Fr = \frac{u_\tau}{gh}, \qquad We = \frac{\rho_2 u_\tau^2 h}{\sigma}, \qquad Ch = \frac{\xi}{h} \tag{1.21}$$

where $g$ is the magnitude of the acceleration of gravity. These dimensionless parameters are: the shear Reynolds number expressing the ratio between inertial and viscous forces, the Froude number expressing the ratio between inertial and gravity forces, the Weber number expressing the ratio between inertial and surface tension forces and finally the Cahn number expressing the non-dimensional thickness of the transition layer between the two phases.

The Cahn-Hilliard equation in its dimensionless form is expressed as:

$$\frac{\partial \phi^-}{\partial t^-} + \mathbf{u}^- \cdot \nabla \phi^- = \frac{1}{Pe} \nabla^2 (\phi^{-3} - \phi^- - Ch^2 \nabla^2 \phi^-) \tag{1.22}$$

where the two dimensionless parameters that appear in the equation are the Peclet number, $Pe = u_\tau h / (\mathcal{M}_\phi \beta)$, which controls the interface relaxation time and expresses a ratio between the convective time scale and the diffusive time scale of the phase-field and the Cahn number, $Ch$, defined before.
Finally, after the dimensionless treatment, the phase-field assumes the values $\phi^- = \pm 1$ in the bulk of the two phases and the equilibrium profile across the transition layer can be expressed in dimensionless form as:

$$\phi^- = \tanh\left(\frac{s^-}{\sqrt{2} Ch}\right) \tag{1.23}$$

In the following, the minus superscript will be dropped and dimensionless quantities will be used without any superscript. In this way, the dimensionless equations are summarized as:

$$\nabla \cdot \mathbf{u} = 0 \tag{1.24}$$

$$\begin{aligned} \rho(\phi)\left(\frac{\partial \mathbf{u}}{\partial t} + \mathbf{u} \cdot \nabla \mathbf{u}\right) &= -\nabla p + \frac{1}{Re_\tau} \nabla \cdot \left[\mu(\phi)\left(\nabla \mathbf{u} + \nabla \mathbf{u}^T\right)\right] + \\ &+ \frac{\rho(\phi)}{Fr^2} \mathbf{g} + \frac{3}{\sqrt{8}} \frac{Ch}{We} \nabla \cdot (\overline{\tau_c}) \end{aligned} \tag{1.25}$$

$$\rho(\phi) = 1 + \frac{\rho_r - 1}{2}(\phi + 1) \tag{1.26}$$

$$\mu(\phi) = 1 + \frac{\mu_r - 1}{2}(\phi + 1) \tag{1.27}$$

$$\frac{\partial \phi}{\partial t} + \mathbf{u} \cdot \nabla \phi = \frac{1}{Pe} \nabla^2 (\phi^3 - \phi - Ch^2 \nabla^2 \phi) \tag{1.28}$$

The non-dimensional numbers, Reynolds, Weber and Froude determine the relative balance of forces in the channel and consequently determine the dynamics of the system. In particular, the Reynolds number controls the ratio between inertial and viscous forces, the Weber number the ratio between inertial and surface tension forces and the Froude number the ratio between inertial and gravity forces. The other two non-dimensional numbers are numerical parameters that are used to achieve convergence of the phase-field to the sharp interface limit. The Cahn number, which is the measure of the non-dimensional transition layer thickness is set to the minimum possible value allowed by the available grid resolution. In general, at least three grid points across the interface are necessary in order to accurately capture the gradients of the phase-field and the other parameters. The Peclet number is set based on the Cahn number according to the scaling $Pe \sim Ch^{-1}$ [57, 58].

## 1.4 Numerical method

In this section, the solution procedure for the dimensionless system of the momentum and the phase-field transport equations inside the channel (see Fig. 1.3) is presented. The momentum equations are solved in the so-called velocity-vorticity formulation in order to avoid the time-consuming step of solving a Poisson equation for the pressure at every time-step [59, 60]. The Cahn-Hilliard equation is solved in its original form, however a split of the Laplace operator is applied in order to improve the stability of the numerical scheme [44, 61].
First, the Navier-Stokes equations are rewritten in a more compact form as:

$$\frac{\partial \mathbf{u}}{\partial t} = \mathbf{S} + \frac{1}{Re_\tau}\nabla^2\mathbf{u} - \nabla p', \tag{1.29}$$

where the pressure term, $p$ is split into a mean and a fluctuating part, $p = \overline{p} + p'$. The mean pressure gradient, $\Pi = \nabla\overline{p}$, together with all the nonlinear terms are collected in the single nonlinear term:

$$\begin{aligned}\mathbf{S} = \; - \;& \mathbf{u}\cdot\nabla\mathbf{u} - \frac{\rho_r - 1}{2}(\phi+1)\left(\frac{\partial \mathbf{u}}{\partial t} + \mathbf{u}\cdot\nabla\mathbf{u}\right) - \Pi + \\ + \;& \frac{1}{Re_\tau}\nabla\cdot\left[\frac{\mu_r - 1}{2}(\phi+1)\left(\nabla\mathbf{u} + \nabla\mathbf{u}^T\right)\right] + \frac{\rho(\phi)}{Fr^2}\mathbf{g} + \frac{3}{\sqrt{8}}\frac{Ch}{We}\nabla\cdot\overline{\tau_c}\end{aligned} \tag{1.30}$$

The same procedure is applied to the Cahn-Hilliard equations, however in this case the term, $\nabla^2\phi$ is split into two parts, one of which is added to the nonlinear term. This technique is employed for the sake of an increased stability of the numerical scheme by integrating a part of the term explicitly and another implicitly (the time-integration schemes are discussed in Sec. 1.4.1).

$$\frac{\partial \phi}{\partial t} = S_\phi + \frac{s}{Pe}\nabla^2\phi - \frac{Ch^2}{Pe}\nabla^4\phi \tag{1.31}$$

$$S_\phi = -\mathbf{u}\cdot\nabla\phi + \frac{1}{Pe}\left[\nabla^2\phi^3 - (s+1)\nabla^2\phi\right] \tag{1.32}$$

where the splitting coefficient, $s$ depends on the time discretization step, $\Delta t$.

$$s = \sqrt{\frac{4PeCh^2}{\Delta t}} \tag{1.33}$$

A transport equation for the vorticity, $\boldsymbol{\omega}$ is obtained by taking the curl, $\nabla\times$ of Eq. 1.29.

$$\frac{\partial \boldsymbol{\omega}}{\partial t} = \nabla\times\mathbf{S} + \frac{1}{Re_\tau}\nabla^2\boldsymbol{\omega} \tag{1.34}$$

where the identity $\nabla\times\nabla p' = 0$ has been used to eliminate the fluctuating pressure gradient term. A fourth-order equation for the velocity is obtained by taking the curl, $\nabla\times$ of Eq. 1.34.

$$\frac{\partial\left(\nabla^2\mathbf{u}\right)}{\partial t} = \nabla^2\mathbf{S} - \nabla(\nabla\cdot\mathbf{S}) + \frac{1}{Re_\tau}\nabla^4\mathbf{u} \tag{1.35}$$

Taking the wall-normal projections of Eq. 1.34 and 1.35, together with the continuity equation, the definition of the wall-normal vorticity and the Cahn-Hilliard equation, leads to a system of five equations with five unknowns, namely the three components of the velocity field, $u, v, w$, the wall-normal vorticity, $\boldsymbol{\omega}\cdot\mathbf{n}_z$, where $\mathbf{n}_z$ is the wall-normal unit vector and the phase-field, $\phi$.

$$\begin{cases} \nabla\cdot\mathbf{u} = 0 \\ \boldsymbol{\omega}\cdot\mathbf{n}_z = (\nabla\times\mathbf{u})\cdot\mathbf{n}_z \\ \dfrac{\partial\boldsymbol{\omega}}{\partial t}\cdot\mathbf{n}_z = \left[\nabla\times\mathbf{S} + \dfrac{1}{Re_\tau}\nabla^2\boldsymbol{\omega}\right]\cdot\mathbf{n}_z \\ \dfrac{\partial\left(\nabla^2\mathbf{u}\right)}{\partial t}\cdot\mathbf{n}_z = \left[\nabla^2\mathbf{S} - \nabla(\nabla\cdot\mathbf{S}) + \dfrac{1}{Re_\tau}\nabla^4\mathbf{u}\right]\cdot\mathbf{n}_z \\ \dfrac{\partial\phi}{\partial t} = S_\phi - \dfrac{s}{Pe}\nabla^2\phi - \dfrac{Ch^2}{Pe}\nabla^4\phi \end{cases} \tag{1.36}$$

Once the velocity field is obtained, the fluctuating pressure $p'$ can also be obtained by solving the Poisson equation resulting from applying the divergence operator, $\nabla\cdot$ on the original Navier-Stokes equations, Eq. 1.29. Thanks to the divergence free velocity fields the viscous term and the temporal term on the right hand side of Eq. 1.29 cancel and the following Poisson equation is obtained:

$$\nabla^2 p' = \nabla\cdot\mathbf{S} \tag{1.37}$$

### 1.4.1 Temporal discretization

An IMplicit EXplicit (IMEX) time integration scheme is employed in order to advance the solution in time. In particular, the nonlinear terms of the momentum equations and of the Cahn-Hilliard equation are integrated with an explicit Euler scheme during the first integration step and with a two-step Adam-Bashforth scheme during all subsequent steps. The linear terms of the momentum equations are integrated using an implicit Crank-Nicolson scheme. The linear terms of the Cahn-Hilliard equation are integrated with an implicit Euler scheme, which has a better performance at damping unphysical high frequency oscillations that arise due to the steep gradients associated with the phase-field [62, 44]. According to the above, the time-discretized equations at the generic step $n$ (current step) can be written as:

$$
\begin{cases}
\nabla \cdot \mathbf{u}^{n+1} = 0 \\
\boldsymbol{\omega}^{n+1} \cdot \mathbf{n}_z = (\nabla \times \mathbf{u}^{n+1}) \cdot \mathbf{n}_z \\
\dfrac{\boldsymbol{\omega}^{n+1} - \boldsymbol{\omega}^{n}}{\Delta t} \cdot \mathbf{n}_z = \left( \dfrac{3\nabla \times \mathbf{S}^{n} - \nabla \times \mathbf{S}^{n-1}}{2} + \dfrac{1}{Re_\tau} \dfrac{\nabla^2 \boldsymbol{\omega}^{n+1} + \nabla^2 \boldsymbol{\omega}^{n}}{2} \right) \cdot \mathbf{n}_z \\
\dfrac{\nabla^2 \mathbf{u}^{n+1} - \nabla^2 \mathbf{u}^{n}}{\Delta t} \cdot \mathbf{n}_z = \left[ \dfrac{3\left[\nabla^2 \mathbf{S}^{n} - \nabla(\nabla \cdot \mathbf{S}^{n})\right] - \left[\nabla^2 \mathbf{S}^{n-1} - \nabla(\nabla \cdot \mathbf{S}^{n-1})\right]}{2} \right. \\
\qquad \left. + \dfrac{1}{Re_\tau} \dfrac{\nabla^4 \mathbf{u}^{n+1} + \nabla^4 \mathbf{u}^{n}}{2} \right] \cdot \mathbf{n}_z \\
\dfrac{\phi^{n+1} - \phi^{n}}{\Delta t} = \dfrac{3S_\phi^{n} - S_\phi^{n-1}}{2} + \dfrac{s}{Pe} \nabla^2 \phi^{n+1} - \dfrac{Ch^2}{Pe} \nabla^4 \phi^{n+1}
\end{cases}
\tag{1.38}
$$

### 1.4.2 Spatial discretization

The numerical technique that is applied to approximate derivatives in space relies on a spectral spatial discretization using Fourier transforms along the two homogeneous directions of the channel, $x$ and $y$ and Chebyshev polynomials along the wall-normal direction, $z$ [63]. The products between variables in the nonlinear convective terms are obtained via multiplication in the physical space and are then transformed to the spectral space so to avoid time-consuming computation of convolution products. A uniform grid spacing is used in the two homogeneous directions, while Chebyshev-Gauss-Lobatto collocation points are used in the wall-normal direction, leading to a finer grid spacing near the two channel walls at $z = \pm 1$ and coarser grid near the channel centreline. The collocation points are defined as:

$$
\begin{aligned}
x_i &= (i-1)\,\frac{L_x}{N_x - 1}, \qquad i = 1, \ldots, N_x \\
y_j &= (j-1)\,\frac{L_y}{N_y - 1}, \qquad j = 1, \ldots, N_y \\
z_k &= cos\left(\frac{k-1}{N_z - 1}\pi\right), \qquad j = 1, \ldots, N_z
\end{aligned}
\tag{1.39}
$$

with the number of grid points in each direction being: $N_x$ (x - direction), $N_y$ (y - direction) and $N_z$ (z - direction). An example of a Chebyshev-Gauss-Lobatto grid points array, assuming a number of $N_z = 45$ points along the wall-normal direction, $z$ is shown in Fig. 1.4. The non-equidistant Chebyshev-Gauss-Lobatto points (shown in red) along the wall-normal direction are the projections of equispaced points around the unit circle (shown in black).
The generic signal, $f(x, y, z, t)$ is approximated in modal space as a truncated series of Fourier wavenumbers and Chebyshev polynomials.

$$
f(x,y,z,t) = \sum_{i=0}^{\frac{N_x}{2}} \sum_{j=-\frac{N_y}{2}+1}^{\frac{N_y}{2}} \sum_{k=0}^{N_z-1} \hat{f}(k_{x,i}, k_{y,j}, k, t) T_k(z) e^{\iota(k_{x,i}x + k_{y,j}y)}
\tag{1.40}
$$

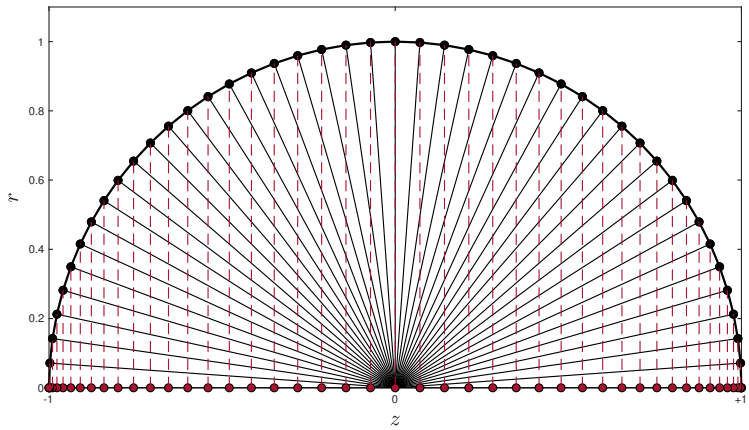


FIGURE 1.4 – Graphical representation of the Chebyshev-Gauss-Lobatto quadrature. The $N_z = 45$ red points correspond to the grid points along the wall-normal direction of the channel between the top wall at $z = +1$ and the bottom wall at $z = -1$.

where $\iota^2 = -1$, is the imaginary unit. The wavenumbers $k_{x,i}$, $k_{y,j}$ are defined as:

$$k_{x,i} = \frac{2\pi(i-1)}{L_x}, \qquad i = 1, ..., N_x/2 + 1 \tag{1.41}$$

$$k_{y,j} = \begin{cases} \dfrac{2\pi(j-1)}{L_y}, & j = 1, \ldots, \frac{N_y}{2} + 1 \\ -\dfrac{2\pi(N_y - j + 1)}{L_y}, & j = \frac{N_y}{2} + 2, \ldots, N_y \end{cases} \tag{1.42}$$

The Fourier amplitudes, $\hat{f}$ are independent of the space coordinates, $x$ and $y$ and thus the derivatives of the signal, $f$ along the two homogeneous directions are computed as:

$$\frac{\partial f(x,y,z,t)}{\partial x} = \sum_{i=0}^{\frac{N_x}{2}} \sum_{j=-\frac{N_y}{2}+1}^{\frac{N_y}{2}} \sum_{k=0}^{N_z-1} \iota k_{x,i} \hat{f}(k_{x,i}, k_{y,j}, k, t) T_k(z) e^{\iota(k_{x,i}x + k_{y,j}y)} \tag{1.43}$$

$$\frac{\partial f(x,y,z,t)}{\partial y} = \sum_{i=0}^{\frac{N_x}{2}} \sum_{j=-\frac{N_y}{2}+1}^{\frac{N_y}{2}} \sum_{k=0}^{N_z-1} \iota k_{y,j} \hat{f}(k_{x,i}, k_{y,j}, k, t) T_k(z) e^{\iota(k_{x,i}x + k_{y,j}y)} \tag{1.44}$$

The derivatives of the truncated Fourier series are computed analytically without introducing an additional error. This is one of the main advantages of spectral methods that leads to high accuracy [63]. Thanks to the orthogonality of Fourier modes the solutions for the modes along the $x$ and $y$ directions are decoupled. In this way,

$(N_x/2+1) \times N_y$ independent subproblems along the wall-normal direction, $z$, for each wavenumber pair, $k_{x,i}, k_{y,j}$ are obtained. The transformed signal $\hat{f}(k_{x,i}, k_{y,j}, z, t)$ notation can then change so to represent the Chebyshev series expansion at a generic wavenumber couple as:

$$\hat{f} = \hat{f}_{i,j} = \sum_{k=0}^{N_z-1} \hat{f}(k_{x,i}, k_{y,j}, k, t) T_k(z) e^{\iota(k_{x,i}x + k_{y,j}y)} \tag{1.45}$$

The discretized system of equations becomes:

$$\begin{cases} \iota k_{x,i}\hat{u}^{n+1} + \iota k_{y,j}\hat{v}^{n+1} + \dfrac{\partial \hat{w}^{n+1}}{\partial z} = 0 \\ \hat{\omega}_z^{n+1} = \iota k_{x,i}\hat{v}^{n+1} - \iota k_{y,j}\hat{u}^{n+1} \\ \dfrac{1}{\Delta t}\left(\dfrac{\partial^2 \hat{w}^{n+1}}{\partial z^2} - k_{i,j}^2 \hat{w}^{n+1} - \dfrac{\partial^2 \hat{w}^{n}}{\partial z^2} + k_{i,j}^2 \hat{w}^{n}\right) = \\ \qquad = \dfrac{3}{2}\left(-k_{i,j}^2 \hat{S_z}^{n} - \iota k_{x,i}\dfrac{\partial \hat{S_x}^{n}}{\partial z} - \iota k_{y,j}\dfrac{\partial \hat{S_y}^{n}}{\partial z}\right) - \\ \qquad - \dfrac{1}{2}\left(-k_{i,j}^2 \hat{S_z}^{n-1} - \iota k_{x,i}\dfrac{\partial \hat{S_x}^{n-1}}{\partial z} - \iota k_{y,j}\dfrac{\partial \hat{S_y}^{n-1}}{\partial z}\right) + \\ \qquad + \dfrac{1}{2Re_\tau}\left(k_{i,j}^4 \hat{w}^{n+1} + \dfrac{\partial^4 \hat{w}^{n+1}}{\partial z^4} - 2k_{i,j}^2 \dfrac{\partial^2 \hat{w}^{n+1}}{\partial z^2}\right) + \\ \qquad + \dfrac{1}{2Re_\tau}\left(k_{i,j}^4 \hat{w}^{n} + \dfrac{\partial^4 \hat{w}^{n}}{\partial z^4} - 2k_{i,j}^2 \dfrac{\partial^2 \hat{w}^{n}}{\partial z^2}\right) \\ \dfrac{\hat{\omega}_z^{n+1} - \hat{\omega}_z^{n}}{\Delta t} = \dfrac{3}{2}\left(\iota k_{x,i}\hat{S_y}^{n} - \iota k_{y,j}\hat{S_x}^{n}\right) - \dfrac{1}{2}\left(\iota k_{x,i}\hat{S_y}^{n-1} - \iota k_{y,j}\hat{S_x}^{n-1}\right) + \\ \qquad + \dfrac{1}{2Re_\tau}\left(\dfrac{\partial^2 \hat{\omega}_z^{n+1}}{\partial z^2} - k_{i,j}^2 \hat{\omega}_z^{n+1} + \dfrac{\partial^2 \hat{\omega}_z^{n}}{\partial z^2} - k_{i,j}^2 \hat{\omega}_z^{n}\right) \\ \dfrac{\hat{\phi}^{n+1} - \hat{\phi}^{n}}{\Delta t} = \dfrac{3\hat{S_\phi}^{n} - \hat{S_\phi}^{n-1}}{2} + \dfrac{s}{Pe}\left(\dfrac{\partial^2 \hat{\phi}^{n+1}}{\partial z^2} - k_{i,j}^2 \hat{\phi}^{n+1}\right) - \\ \qquad - \dfrac{Ch^2}{Pe}\left(k_{i,j}^4 \hat{\phi}^{n+1} + \dfrac{\partial^4 \hat{\phi}^{n+1}}{\partial z^4} - 2k_{i,j}^2 \dfrac{\partial^2 \hat{\phi}^{n+1}}{\partial z^2}\right) \end{cases} \tag{1.46}$$

with the coefficient $k_{i,j}^2$ being the sum of the squares of the two wavenumbers, $k_{i,j}^2 = k_{x,i}^2 + k_{y,j}^2$.

Next, all the terms from the current, $n$ and the previous, $n-1$, time step are collected in a historic term.

$$\begin{cases} H_i^n = \Delta t \left[ \dfrac{3\hat{S}_i^n - \hat{S}_i{}^{n-1}}{2} + \dfrac{1}{2Re_\tau} \dfrac{\partial^2 \hat{u}_i{}^n}{\partial z^2} + \left( \dfrac{1}{\Delta t} - \dfrac{k_{i,j}^2}{2Re_\tau} \right) \hat{u}_i{}^n \right], \quad i = x, y, z \\ H^n = \dfrac{\partial}{\partial z} \left( \iota k_{x,i} H_x{}^n + \iota k_{y,j} H_y{}^n \right) + k_{i,j}^2 H_z{}^n \\ H_\phi{}^n = \dfrac{\Delta t}{2} \left( 3\hat{S}_\phi{}^n - \hat{S}_\phi{}^{n-1} \right) + \hat{\phi}^n \end{cases} \tag{1.47}$$

After splitting knowns from unknowns the final system of equations becomes:

$$\begin{cases} \iota k_{x,i} \hat{u}^{n+1} + \iota k_{y,j} \hat{v}^{n+1} + \dfrac{\partial \hat{w}^{n+1}}{\partial z} = 0 \\ \hat{\omega}_z^{n+1} = \iota k_{x,i} \hat{v}^{n+1} - \iota k_{y,j} \hat{u}^{n+1} \\ \left( \dfrac{\partial^2}{\partial z^2} - \beta^2 \right) \left( \dfrac{\partial^2}{\partial z^2} - k_{i,j}{}^2 \right) \hat{w}^{n+1} = \dfrac{H^n}{\gamma} \\ \left( \dfrac{\partial^2}{\partial z^2} - \beta^2 \right) \hat{\omega}_z^{n+1} = -\dfrac{\iota k_{x,i} H_y^n - \iota k_{y,j} H_x^n}{\gamma} \\ \left( \dfrac{\partial^2}{\partial z^2} - \beta_\phi^2 \right) \left( \dfrac{\partial^2}{\partial z^2} - \beta_\phi^2 \right) \hat{\phi}^{n+1} = \dfrac{H_\phi^n}{\gamma_\phi} \end{cases} \tag{1.48}$$

where the parameters $\gamma$, $\beta$ and $\gamma_\phi$, $\beta_\phi$ are defined as:

$$\gamma = \frac{\Delta t}{2Re_\tau}, \qquad \beta^2 = \frac{1 + \gamma k_{i,j}^2}{\gamma} \tag{1.49}$$

$$\gamma_\phi = \frac{Ch^2 \Delta t}{Pe}, \qquad \beta_\phi^2 = \frac{s}{2Ch^2} + k_{i,j}^2 \tag{1.50}$$

Chebyshev polynomials (and their derivatives) are defined recursively as:

$$T_n(z) = 2zT_{n-1}(z) - T_{n-2}(z) \tag{1.51}$$

This property together with the orthogonality of the Chebyshev modes is exploited by the Chebyshev-Tau method [59], that is used to solve the $(N_x/2+1) \times N_y$ independent uni-dimensional problems along the wall-normal direction. The derivatives along the z-direction are approximated based on the amplitudes of neighbouring Chebyshev modes, which results in a tridiagonal system that is solved via Gauss elimination. Finally, due to the pseudo-spectral character of the method, with products taken in the physical space and then transformed to spectral space, the introduction of de-aliasing procedures is required, in order to guarantee the accurate reconstruction of the signals from the spectral to the physical space. For this purpose, the "2/3 rule" [201] is applied, according to which the Fourrier and the Chebyshev space bandwidths are reduced by setting one third of the highest wavenumber modes or polynomials to zero.

### 1.4.3 Boundary conditions

The adoption of the Fourier discretization along the two homogeneous directions, $x$ and $y$ implies that periodic boundary conditions are necessarily applied across these two directions. In the close channel configuration the two walls at $z = \pm 1$ act as the two solid boundaries, where no-slip and no-flux boundary conditions are applied to the flow field.

$$\begin{cases} \mathbf{u}(x, y, z = \pm 1) = [u_w, v_w, 0] \\ \left.\dfrac{\partial w}{\partial z}\right|_{z=\pm 1} = 0 \\ \omega_z(x, y, z = \pm 1) = 0 \end{cases} \tag{1.52}$$

where $u_w$, $v_w$ is the streamwise and the spanwise velocity of the wall, respectively. The phase-field transport equation is fourth-order and therefore requires an additional boundary condition to the no-flux condition for the phase-field, which guarantees that no advection of the phase-field can take place across the two walls. This additional condition is a no-flux condition imposed on the chemical potential and ensures that no diffusion of the phase-field can occur across the boundaries.

$$\begin{cases} \left.\dfrac{\partial \phi}{\partial z}\right|_{z=\pm 1} = 0 \\ \left.\dfrac{\partial^3 \phi}{\partial z^3}\right|_{z=\pm 1} = 0 \end{cases} \tag{1.53}$$

## 1.5 Multiple resolution strategy

The key issue in the study of turbulent multiphase flows is the wide range of spatial and temporal scales involved in the problem: from flow phenomena that occur at scales ranging from the integral scale of the problem down to the Kolmogorov scale, to interfacial phenomena that occur on a much wider range of scales, from the scale of a wave or a drop down to the molecular scale of the interface. Typically, the scale separation between flow and interfacial scales is about eight to nine orders of magnitude, a situation which renders accurate simulations – taking into account all flow and interfacial scales – extremely challenging to perform [64, 65, 31]. In addition, the numerical description of an ever-moving and deforming interface requires numerical methods able to capture its deformation and topological changes. When employing interface capturing methods such as the PFM, it is desirable to solve the colour/marker function variable on a grid that is refined as much as possible. In this way, short waves, small drops or ligaments can be accurately captured and topological changes better described [66, 67, 31]. Clearly, there is a limit to the grid resolution one can reasonably afford, even using cutting-edge HPC resources.
The challenge associated with the resolution of all the involved scales and the limitation on the grid resolution one can reasonably afford has driven researchers towards the development of different strategies. Two possible approaches can be envisioned to

increase the efficiency of the computational techniques so as to improve the description of multiphase flows: adaptive mesh refinements (AMR) or multiple resolution approaches. Using AMR schemes [68, 69], the computational grid is locally refined near the interface, where most of the marker function gradients are located and a coarser grid resolution (thus reducing the computational cost) can be adopted farther from the interface. This strategy has been applied to the most popular interface capturing methods (using quadtree-, octree-based algorithms): Volume of Fluid [70, 71, 72, 73], Level Set [74, 75, 76, 77, 78, 79, 80], Lattice-Boltzmann [81, 82] and Phase-Field Method [83, 84]. Differently, using multi-resolution strategies, the flow field is resolved on a base grid, fine enough to capture the smallest flow scale (i.e., order of the Kolmogorov length-scale), while the marker function is solved on a more refined grid so that smaller interfacial features can be described [85, 49, 86, 87]. Each of these techniques has its own advantages and disadvantages. On one hand, while in principle AMR schemes provide the most cost-effective strategy (as the grid is only refined at the interface location), it is not straightforward to balance the load among the different parallel tasks (the parallelization strategy used here is discussed in Sec. 1.6.1), since the load depends on the interface location and thus it is difficult to obtain good scalability when a large number of tasks is used. In addition, AMR schemes, are mainly suited for local methods (e.g., finite-difference, finite-volume schemes, finite-element or Lattice-Boltzmann methods) and less applicable to global methods, like spectral methods [88]. On the other hand, multiple resolution approaches are less effective in reducing the computational cost, but are also less affected by scalability issues (as the computational load per parallel process does not vary over time) and can be applied to different numerical methods [85, 49, 86, 87]. These differences are also reflected in the ease of implementation of these two techniques. Generally speaking, AMR is of more difficult implementation, and external libraries [89, 79] are often used, while the multiple resolution approach can be implemented in an easier manner, as the solution schemes do not require extensive modifications.

In this section, a multiple resolution strategy for the DNS-PFM technique of multiphase turbulence, described in the previous sections, is presented. As the solution of the Navier-Stokes equations in refined grids is extremely time- and memory-demanding, two different computational grids (dual-grid approach) are used: a base grid for the flow field, which must be fine enough to solve for the flow field down to the Kolmogorov scale and a refined grid for the phase-field variable. This allows for the accurate description of the flow field and at the same time for an improvement of the description of the small interfacial features (waves, drops, ligaments). The base reference grid (labelled BG) with $N_x \times N_y \times N_z$ grid points is used to describe the flow-field and has to be fine enough to resolve the smallest flow scale (order of the Kolmogorov scale), while the finer grid (labelled FG) with $M_x N_x \times M_y N_y \times M_z N_z$ grid points (with $M_i$ positive integer representing the refinement factor along the $i$-direction) is used for the phase-field variable. To time advance the solution, a time-marching algorithm is employed and at each time step, the following steps are executed:

i) The velocity field, $\mathbf{u}^n$, is initialised on the base grid (BG); the phase-field, $\phi^n$, is initialised on the fine grid (FG); variables are transformed in the spectral space, $\hat{\mathbf{u}}^n$ and $\hat{\phi}^n$.

ii) The surface tension term, which depends on the phase-field variable, is computed on the fine grid (FG) and then spectrally interpolated onto the base grid (BG).

iii) The non-linear viscous and inertial terms, which also can depend on the phase-field, are computed on the fine grid (FG) and then spectrally interpolated onto the base grid (BG).

iv) Navier-Stokes equations are solved on the base grid (BG) to obtain the new velocity-field, $\hat{\mathbf{u}}^{n+1}$.

v) The new velocity-field, $\hat{\mathbf{u}}^{n+1}$, is spectrally projected onto the fine grid (FG).

vi) Finally, the Cahn-Hilliard equation is solved on the fine grid (FG) to obtain the new value of the phase-field, $\hat{\phi}^{n+1}$.

A flow-chart showing the different steps required to advance the solution in time is shown in Fig. 1.5. The validation of the dual-grid approach is presented in Sec. 1.7.2.

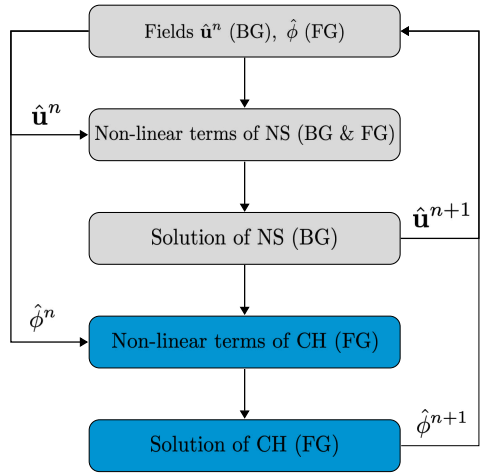


FIGURE 1.5 – Flow chart of the steps required to time advance the solution from the current time step, $n$, to the next time step, $n+1$, using the dual-grid approach.

## 1.6 Code implementation

The numerical algorithm presented in Sec. 1.4 for the solution of the equations presented in Sec. 1.3 has been implemented as an in-house code written in Fortran-2003 [34, 35, 31].

### 1.6.1 Parallelization strategy

The code is parallelised using the Message Passing Interface (MPI) paradigm. Within this framework a single process is assigned to each core, which has its own memory that

is not directly accessible by other cores. Therefore, the interchange of data between the different processes (or tasks) is based on communication through message passing known as MPI communication. MPI offers great scalability potential, since communication can take place across cores belonging to different nodes of a supercomputing cluster. This is in contrast to shared memory parallelization models, such as the Open Multi-Processing (OpenMP) model, which is based on a shared memory protocol and therefore allows for a parallelization between cores that share the local memory of a single node. The solution algorithm is executed simultaneously by a number of MPI tasks (or ranks). The workload is divided between different tasks following a partition of the three-dimensional computational domain across two dimensions. In particular, each rank initially holds a fraction of the total grid points along the $y$ and $z$ directions and all the grid points along the $x$ direction. However, the spectral method that is used to resolve the equations implies that Fourier and Chebyshev transforms need to be performed in order to transform the variables from the physical to the spectral space and back. These transforms are global, which means that each rank needs to have available in its memory every grid point across the direction along which the transform is performed. This practically means that the domain partition model has to be reoriented several times during each computational step in order for all the necessary transforms to be performed with success. The latter can be achieved through MPI communication between the ranks. A schematic representation of the steps required to compute a three-dimensional transform is shown in Fig. 1.6.

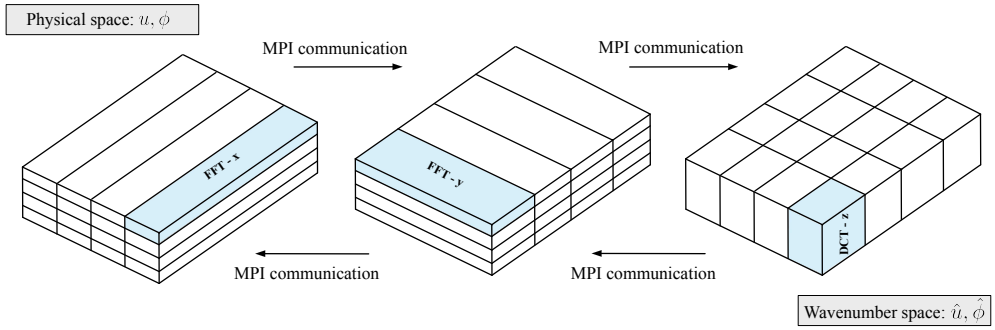


FIGURE 1.6 – From the right, the unknowns are in the physical space, $u, \phi$, the FFT along the $x$ direction is computed first. Then, through MPI communications, the domain partition is reoriented and the FFT along the $y$ direction is performed. Last, the partition is again reoriented and the Chebyshev transform along the $z$ direction is computed. After these steps, the unknowns are now in the wavenumber (or spectral) space, $\hat{u}, \hat{\phi}$. The inverse transform can be computed following the same steps but in the opposite direction.

The performance of the code was measured using the HPC compute node LUMI-C (FI) . This machine is equipped with two AMD EPYC 7763 CPUs with 64 cores each running at 2.45 $GHz$ for a total of 128 cores per node. In particular, strong scaling tests - overall computational time to complete a single time-step as function of number of processing elements - were performed for two different grid sizes: $N_x \times N_z \times N_y = 1024 \times 513 \times 256$ and $N_x \times N_z \times N_y = 2048 \times 513 \times 1024$. The results are demonstrated in Fig. 1.7. The speed-up or increase in performance with respect to the reference

case of the minimum number of cores used (16 cores), is reported in the y-axis, while the different number of cores used is reported in the x-axis. Ideally the speed-up should grow linearly with the number of cores used, which practically means that the computation time should be halved each time the total number of cores is doubled. The ideal curve is reported with a dashed black line. For both problem sizes the speed-up follows well the ideal curve suggesting a good scaling behaviour. The drop in performance observed when a higher number of cores is used can be associated to the increase in the number of MPI communications between ranks, since in this case the total number of ranks increases, while at the same time the number of computations performed by each rank is reduced. Based on the scaling test results, a maximum number of $128 \times 64$ ranks (8192 cores) has been selected for the purposes of the simulations performed in this work, considered to be a good compromise between computation time and performance. Indicatively, for the $1024 \times 513 \times 256$ problem size, this results in a simulation time per time step that is of the order of 100 $ms$.

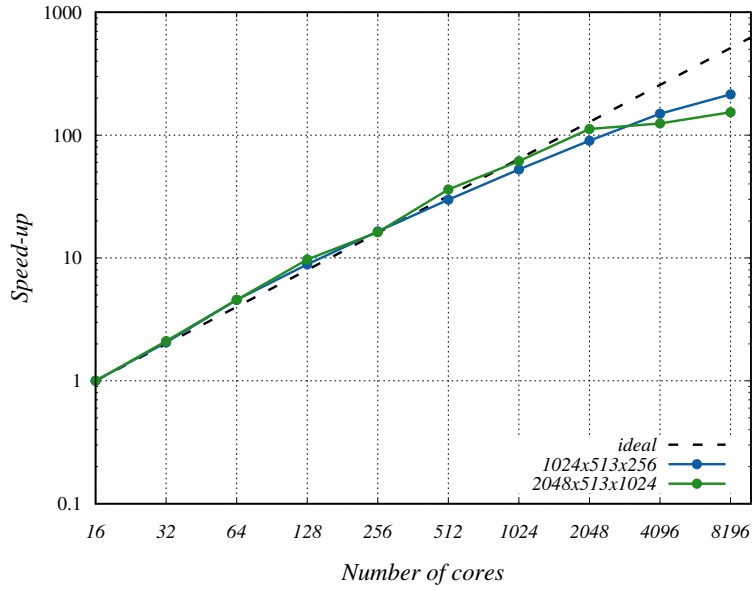


FIGURE 1.7 – Strong scaling tests for different grid sizes performed on LUMI-C (FI) HPC compute node. Grid $1024 \times 513 \times 256$ is shown with a blue line and $2048 \times 513 \times 1024$ with a green line. The black dashed line shows the ideal linear scaling.

### 1.6.2 Space-time resolved interface statistics

The simulation output is obtained by solving the Navier-Stokes equations and the Cahn-Hilliard equation. In particular, at each time-step the three components of the velocity field, $u, v, w$ and the phase-field variable, $\phi$ are computed. In terms of computer memory, each of the four fields is represented by one double precision numeric value or 8 Bytes of memory for every grid point. Therefore, for the typical grid size that is used in this work i.e. $N_x = 1024$, $N_y = 256$ and $N_z = 513$ grid points across

the $x$, $y$ and $z$ directions, respectively, a total memory of approximately 1 GByte for each field or 4 GByte for all of the four fields for every time step is required. Storing this amount of information can quickly become problematic in terms of hard disk memory occupancy. Fortunately, obtaining averaged statistics of the turbulent flow field requires only a limited number of fields saved over a large enough time window to guarantee the lack of any residual historic effects between consecutive fields. This is due to the triple-averaging of the hydrodynamic fields in both $x$ and $y$ directions and in time, which gives a quick convergence of the statistics using only a small number of time frames. In contrast, obtaining time-resolved interface statistics, which is one of the main objectives of this work, requires a much more frequent storage of the phase-field variable, which contains information on the topology of the two fluids inside the domain and therefore also on the interface position. However, not all the values of the phase-field on every grid point are required in order to reconstruct the interface shape. The interface is identified as the $\phi = 0$ iso-contour and therefore solely the extraction of this iso-contour suffices. The extraction of the interface, as well as the values of the velocity interpolated on the interface, can take place during the simulation run-time. Two techiques have been developed to serve this particular purpose and are presented below.

**Two-dimensional interface extraction - waves**

The first technique to extract the interface signal is specifically tailored for the case of a continuous interface separating two fluid layers. The interface in this case can deform, but the deformation is characterized by the presence of non-breaking waves with relatively low amplitudes. The idea is that the interface signal remains single-valued i.e. can be described by a single variable, the so called wave elevation, $\eta(x, y, t)$ during the whole simulation time. The wave elevation is defined as the vertical distance of the interface from the mean interface level. Therefore, at each time instant, for each pair of horizontal coordinates, $x(i)$ and $y(j)$ a wave elevation $\eta(i, j)$ can be determined. In this scenario, determining the interface position via the extraction of the $\phi = 0$ iso-contour is rather straight-forward. In particular, at each horizontal position $x(i), y(j)$ a uni-dimensional scan of the domain along the wall-normal coordinate, $z(k)$ is performed for every $k$ so to find the position where $\phi(i, k, j) = 0$. Since the phase-field takes the values $\phi = \pm 1$ in the bulk of the two phases and transitions between these two values smoothly at the transition layer, the location at which $\phi(i, k, j) = 0$ coincides with the first change in sign of the product $\phi(i, k, j) * \phi(i, k+1, j)$. In the case of single-valued interface deformation a single such transition must take places at each $x(i), y(j)$ position. The wave elevation, $\eta(i, j)$ is then identified as the $z(k)$ value at which this transition occurs. Note that since each rank contains in physical space only a part of the phase-field values along the $y$ and $z$ directions and all the values across the $x$ direction, additional MPI communication is required in order to communicate the boundary values of $\phi$ between neighbouring ranks and make possible the computation of the product $\phi(i, k, j) * \phi(i, k+1, j)$ at all $k$ positions. This step implies an additional overhead in terms of computation time, due to the MPI communications among the different ranks. However, the total overhead is small (of the order of 1% of the overall computation), and only for those steps for which the algorithm is executed, which typically corresponds to a few hundred steps. At the same time, the memory requirement of

this run-time extraction of the interface signal is dramatically reduced compared to the alternative of storing the phase-field at such a high saving frequency. Indeed, instead of saving the entire $\phi$ field with $N_x \times N_y \times N_z = 1024 \times 513 \times 256 = 134,479,872$ values, which amounts to $1GByte$ of memory, at each saving step, only the iso-countour, $\phi = 0$ with $N_x \times N_y = \times 1024 \times 256 = 262,144$ values, which amounts to $2MByte$ of memory, is saved. Finally, the three components of the velocity field $u, v, w$ can also be interpolated at the interface position providing additional information on the instantaneous interface velocity. This scanning algorithm has been implemented and integrated to the main code framework as an individual subroutine. The algorithm has been used to obtain the time resolution necessary to compute the frequency and frequency-wavenumber spectra of capillary waves presented in Chap. 2 and 3 and the animations of wave motion included in the supplementary material of Giamagas et al. [90].

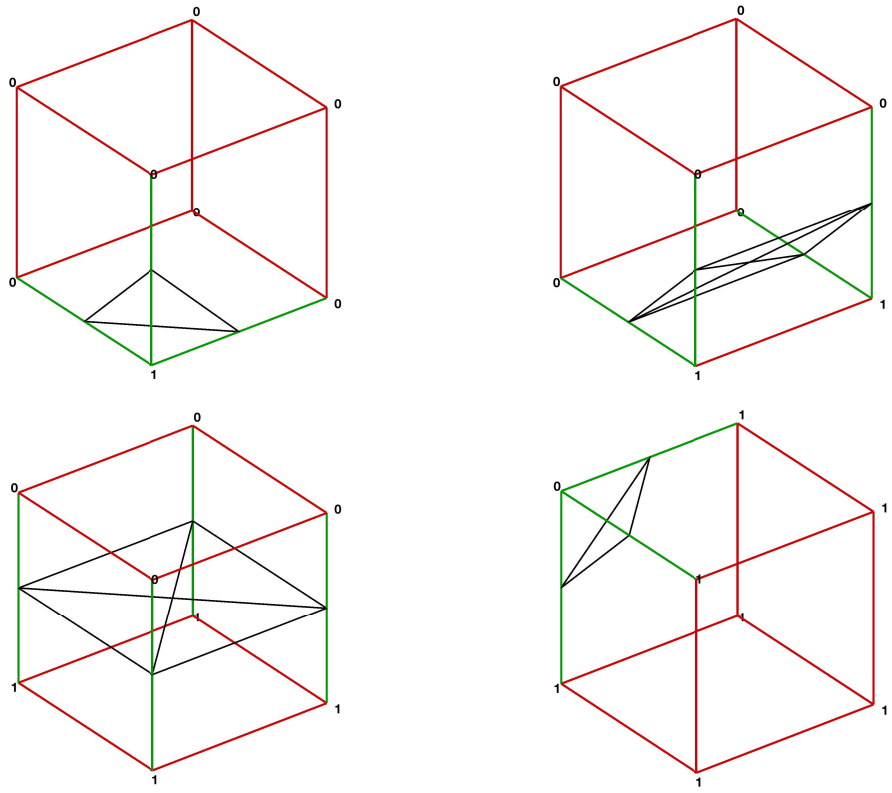

FIGURE 1.8 – Different polygon configurations emerging in the marching cubes algorithm triangulation step. The bit values 0 and 1 can be seen on the vertices of the cube. The polygon edges, shown in black, connect the midpoints of edges with different digits at their vertices. The connected edges are coloured in green contrary to the unconnected edges, which are coloured in red.

**Three-dimensional interface extraction - drops**

The second technique is more general and deals with the extraction of an arbitrary three-dimensional interface topology (breaking waves, droplets, ligaments, etc). In this scenario, the extraction of the so-contour, $\phi = 0$ cannot be based on a uni-dimensional scan of the domain, since the number of transitions from one phase to the other along any of the three dimensions can be larger than one and thus a more sophisticated technique needs to be employed. For this purpose, a marching cubes algorithm [92] has been implemented and integrated to the main code framework as an individual subroutine. The marching cubes is an algorithm for the three-dimensional reconstruction of an iso-contour given the values of a scalar field (in this case the phase-field, $\phi$) on a rectilinear grid. The discretized scalar field is scanned considering eight neighbouring points at each time, which form the vertices of a cuboid. In particular, a bit (1 or 0) is assigned to each of the eight vertices of the cuboid. The value of each bit is decided by comparing the scalar values of $\phi$ at the vertices of the cuboid to the iso-value, $\phi = 0$. If $\phi > 0$ then the bit is set to one, else it is set to zero. This results in a total of $2^8 = 256$ possible cuboid combinations (or indexes), each with a unique set of bit values at its vertices. Each index also corresponds to a unique polygon configuration that can connects the edges of the cuboid so to represent the $\phi = 0$ iso-countour. Only the edges with different bits (zero and one) at their vertices are connected, while those with the same bits (0 and 0 or 1 and 1) are not. The position of the vertices of the polygons is determined by means of linear interpolation between the values of $\phi$ at the vertices of the cuboid on each connected edge. An example of different polygon configurations for different indexes, where the midpoints of the connected edges have been considered as the polygon vertices for the shake of simplification, is shown in Fig. 1.8. In this case too, the three components of the velocity field u,v,w can be interpolated on the connected edges intersection points providing additional information on the instantaneous velocity of the interface. Moreover, the normal vectors to the interface, $\vec{n} = \frac{\nabla\phi}{|\nabla\phi|}$ are computed by means of interpolating the gradient of $\phi$ on every connected point. Finally, the total surface area of the interface is also approximated by the sum of all the polygon areas. In this case too, the total overhead due to the MPI communication associated with the exchange of vertex bit values between ranks with shared cuboids, is of the order of 1% of the overall computation and only for these steps for which the algorithm is applied, typically every few hundred steps. The memory requirement is once again reduced dramatically and time-resolved interface data can be stored easily. Despite the fact that a larger number of values compared to the previous ($N_x \times N_y$) case represent the iso-contour depending on the flow topology, the order of magnitude of the memory requirement is still only a few $MByte$. The time evolution of the interfacial area and the animations of the thin layer breakup in turbulence presented by Schenk et al. [93] have been obtained using this technique.

## 1.7 Validation

The code is validated using two different benchmark configurations. The basic Navier-Stokes and Cahn-Hillard equation solver has been validated using the test case of a

simple two-layer pressure-driven laminar channel flow configuration. The multiple resolution strategy has been validated using the benchmark case of a single droplet subjected in a shear laminar flow. Finally, the Navier-Stokes solver alone i.e. without the solution of the Cahn-Hillard equation, has also been validated using a shear-driven single-phase turbulent flow as a test case and is reported in Appendix A.

### 1.7.1 Two-layer laminar channel flow

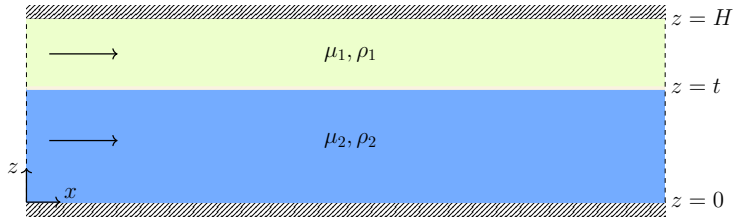


FIGURE 1.9 – Two fluid layers flowing in parallel in a rectangular channel driven by the action of a mean pressure gradient. The arrows indicate the flow direction.

The flow of two fluid layers of different thermophysical properties (fluid 1: $\mu_1, \rho_1$ and fluid 2: $\mu_2, \rho_2$) in a rectangular channel (see Fig. 1.9), driven by a constant pressure gradient, at low Reynolds number, can be described analytically [94]. The general unsteady momentum balance equations considering the whole fluid volume writes:

$$\rho(\frac{\partial u_i}{\partial t} + u_j \frac{\partial u_i}{\partial x_j}) = -\frac{\partial P}{\partial x_i} + \mu \frac{\partial^2 u_i}{\partial x_j^2} \tag{1.54}$$

from where, after expressing the balance for each individual fluid layer at steady state, we obtain:

$$\mu_1 \frac{\partial^2 u_1}{\partial z^2} = \frac{\Delta P}{\Delta x} \tag{1.55}$$

$$\mu_2 \frac{\partial^2 u_2}{\partial z^2} = \frac{\Delta P}{\Delta x} \tag{1.56}$$

for the flow of fluid $1 : \mu_1, \rho_1$ and the flow of fluid $2 : \mu_2, \rho_2$, respectively

The boundary conditions applied are no-slip at the two solid walls of the channel, located at $z = 0$ and $z = H$, and continuity of the velocity and the shear stress at the interface between the two fluid layers, located at $z = t$. These conditions are expressed as follows:

$$u_1(H) = 0, \;\; u_2(0) = 0, \;\; u_1(t) = u_2(t), \;\; \mu_1 \frac{\partial u_1}{\partial z}(t) = \mu_2 \frac{\partial u_2}{\partial z}(t) \tag{1.57}$$

Integrating the two equations, Eq. 1.55, 1.56 and applying the boundary conditions, Eq. 1.57, we obtain the solution for the velocity profile at each layer:

$$u_1(z) = \frac{H^2}{2\mu_1}\left(-\frac{\Delta P}{\Delta x}\right)\left[-\left(\frac{z}{H}\right)^2 + 1 + \left(\frac{z}{H} - 1\right)\frac{1 - k^2\left(1 - \mu_r\right)}{1 - k\left(1 - \mu_r\right)}\right] \tag{1.58}$$

$$u_2(z) = \frac{H^2}{2\mu_2}\left(-\frac{\Delta P}{\Delta x}\right)\left[-\left(\frac{z}{H}\right)^2 + \frac{z}{H}\frac{1 - k^2\left(1 - \mu_r\right)}{1 - k\left(1 - \mu_r\right)}\right] \tag{1.59}$$

where $k = t/H$ is the non-dimensional thickness of the bottom layer, $\mu_r = \mu_1/\mu_2$ is the ratio between the dynamic viscosities of the two fluids. Note that the solution depends only on the dynamic viscosities of the fluids and not on the fluid density at a given constant pressure gradient.
Taking as reference the properties of fluid 2: $\mu_2$, $\rho_2$ and considering the half channel height, $h$ as characteristic length scale and the friction velocity, $u_\tau$ of the single phase Poiseuille flow of fluid 2 as characteristic velocity scale, while also assuming that $k = 0.5$, we can non-dimensionalize the previous equations as follows:

$$u_1\left(z\right) = -\frac{Re_\tau}{2\mu_r}z^2 + \frac{Re_\tau}{2\mu_r}\frac{3 + \mu_r}{1 + \mu_r}z + \frac{2Re_\tau}{\mu_r} - \frac{Re_\tau}{\mu_r}\frac{3 + \mu_r}{1 + \mu_r} \tag{1.60}$$

$$u_2\left(z\right) = -\frac{Re_\tau}{2}z^2 + \frac{Re_\tau}{2}\frac{3 + \mu_r}{1 + \mu_r}z \tag{1.61}$$

where $Re_\tau = \rho_2 u_\tau h/\mu_2$ is the Reynolds number, expressing the ratio between inertial and viscous forces.
A more representative velocity scale for each layer can also be determined by considering the two-phase instead of the single-phase problem. In this case, the stress at the two walls and on the interface can be calculated as:

$$\tau_{w,1} = \frac{\Delta P}{\Delta x}H\left[1 - \frac{1}{2}\frac{1 - k^2\left(1 - \mu_r\right)}{1 - k\left(1 - \mu_r\right)}\right] \tag{1.62}$$

$$\tau_{w,2} = \frac{\Delta P}{\Delta x}\frac{H}{2}\frac{1 - k^2\left(1 - \mu_r\right)}{1 - k\left(1 - \mu_r\right)} \tag{1.63}$$

$$\tau_{int,1} = -\tau_{int,2} = \frac{\Delta P}{\Delta x}H\left[k - \frac{1}{2}\frac{1 - k^2\left(1 - \mu_r\right)}{1 - k\left(1 - \mu_r\right)}\right] \tag{1.64}$$

The friction velocities at the two walls of the two-phase flow can then be expressed in the form of corrections to the friction velocity of the single-phase flow, due to the wall shear stress and the density mismatch [95, 4].

$$u_{\tau,1} = u_\tau\sqrt{\frac{2\rho_r|\tau_{w,1}|}{|\tau_{w,1}| + |\tau_{w,2}|}} \tag{1.65}$$

$$u_{\tau,2} = u_\tau\sqrt{\frac{2|\tau_{w,2}|}{|\tau_{w,1}| + |\tau_{w,2}|}} \tag{1.66}$$

at the top wall and at the bottom wall, respectively, with $\rho_r = \rho_1/\rho_2$ being the ratio between the fluid densities.

In a similar way, a semi-local Reynolds number in each of the two fluid layers can be defined and expressed as a correction of the Reynolds number for the single-phase flow as:

$$Re_{\tau,1} = \frac{\sqrt{\rho_r} Re_\tau}{\mu_r} \sqrt{2 - \frac{1 - k^2 (1 - \mu_r)}{1 - k (1 - \mu_r)}} \tag{1.67}$$

$$Re_{\tau,2} = Re_\tau \sqrt{\frac{1 - k^2 (1 - \mu_r)}{1 - k (1 - \mu_r)}} \tag{1.68}$$

Finally, note that while the above estimations of the shear-stresses for the two-phase flow are exact, they are only valid within the assumption of a laminar flow regime. The more general case of a turbulent flow regime is much more complex with momentum transfer in directions perpendicular to the direction of the mean pressure gradient and deformation of the interface. In such scenario, the stresses at the wall and at the interface and therefore also the semi-local Reynolds numbers can only be numerically approximated.

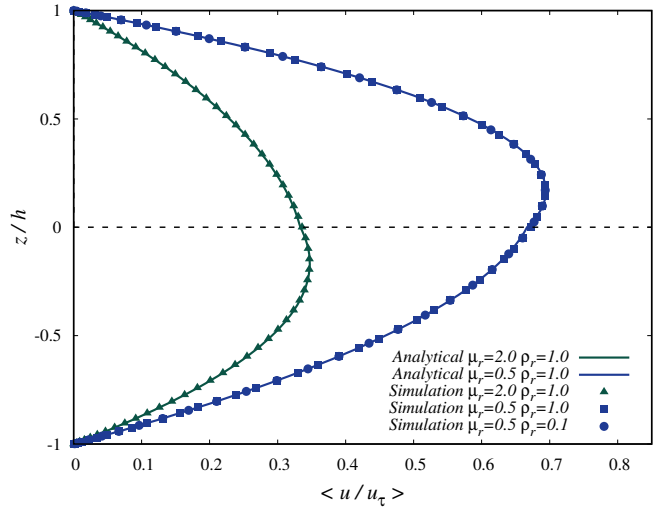


FIGURE 1.10 – Comparison between analytically calculated and numerically computed mean velocity profiles of a two-layer Poiseuille flow for two different values of the viscosity ratio, $\mu_r = 2.0$ and $\mu_r = 0.5$, and two different values of the density ratio, $\rho_r = 1.0$ and $\rho_r = 0.1$.

The code has been validated against the analytical solution by performing simulations of the two-layer Poiseuille flow at $Re_\tau = 1$, $k = 0.5$ and for two different viscosity ratios, $\mu_r = 0.5$ and $\mu_r = 2.0$. The results are shown in Fig. 1.10. An excellent agreement is observed between the numerical and analytical results for both cases of the viscosity ratio. In particular, the percentage error in the numerically computed versus the analytically calculated flow rate is below 1% for both of the simulated cases. In order to further demonstrate the independency of the solution from the density ratio, an additional simulation has been performed considering two fluids with different

densities. Indeed, the velocity profiles are identical for the same set of parameters, but for two different values of the density ratio, $\rho_r = 1.0$ and $\rho_r = 0.1$.

### 1.7.2 Drop deformation in laminar shear flow

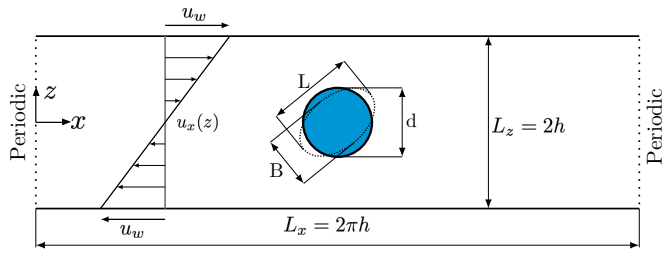


FIGURE 1.11 – Sketch of the deformation of a drop in a shear flow. A circular drop of diameter $d = 0.8h$ is initially located at the centre of the channel (blue circle). The domain is two-dimensional with dimensions $L_x \times L_z = 2\pi h \times 2h$. Periodicity is applied along $x$, and the two walls move in opposite directions with constant velocity $u_x = u_w = \pm 1$. The imposed shear deforms the drop into an ellipsoid (a qualitative representation of its final shape is given by the dotted line). Drop deformation is evaluated computing the deformation parameter $D = (L - B)/(L + B)$, being $L$ and $B$ the major and minor axes of the ellipsoid, respectively.

The multi-resolution strategy proposed in Sec. 1.5 is benchmarked for the case of a single drop immersed in a laminar shear flow, as sketched in Fig. 1.11. A circular drop of diameter $d = 0.8h$ is placed at the centre of a plane channel, in which the top and bottom walls move at constant velocity, $u_w$, but in opposite directions. The simulations performed consider a two-dimensional domain.
The initial condition for the flow field is a linear velocity profile for the streamwise velocity, $u_x$, along the wall-normal direction, $z$, while the wall-normal velocity is set to zero. The phase-field, $\phi$, is initialized so that the drop is located at the centre of the channel. The computational domain has dimensions $L_x \times L_z = 2\pi h \times 2h$ along the $x$- and $z$-directions, respectively. The Reynolds number – evaluated for this benchmark using the wall velocity – is kept constant among all simulations, $Re_w = 0.1$. The value of the Cahn number, $Ch = 0.02$, is set so to have a minimum of 3 grid points across the transition layer between the phases [96]. Accordingly, the Peclet number is set to $Pe = 1/Ch = 50$. An overview of the simulation parameters is given in Tab. 1.1.
Given the low value of the Reynolds number, the flow remains laminar and the velocity profile is linear. The resulting shape of the drop is determined by the competition between viscous forces – which try to deform the drop – and surface tension forces – which try to restore the original, circular shape (being the droplet two-dimensional). The relative importance of viscous and surface tension forces (and thus drop deformation) is controlled by the Capillary number.

$$Ca = \frac{We}{Re_w}\frac{d}{2h} \tag{1.69}$$

In this benchmark, to compare the results with previous literature studies [97, 98, 99], the Capillary number is defined based on the drop radius, hence the scaling factor $d/2h$

| Code | Refinement factor, $M_i$ | Grid NS | Grid CH | $Ch$ | $Pe$ |
|---|---|---|---|---|---|
| $G1$ | 1x1 | 512x513 | 512x513 | 0.02 | 50 |
| $G2$ | 2x2 | 256x257 | 512x513 | 0.02 | 50 |
| $G4$ | 4x4 | 128x129 | 512x513 | 0.02 | 50 |

TABLE 1.1 – Summary of the simulation parameters for the benchmark of the drop deformation in a two-dimensional shear flow. Three different simulations are run, by keeping the resolution of the Cahn-Hilliard equation constant ($N_x \times N_z = 512 \times 513$ grid points, Grid CH), and reducing the resolution of the Navier-Stokes equation (Grid NS). The refinement factors, $M_i$, are also reported. Simulations are labelled based on the employed refinement factor: $G1$ indicates a refinement factor of 1 (i.e., same grid); $G2$ indicates a refinement factor of 2 between the NS grid and the CH grid; $G4$ indicates a refinement factor of 4.

is introduced. Note that the Weber number, $We$ expressing the ratio between inertial and surface tension forces also appears in the above relation. Numerical simulations are run considering two different values of the viscosity ratio, $\mu_r = 0.1$ and $\mu_r = 1.0$, and three different values of the Capillary number: $Ca = 0.062$, $Ca = 0.125$ and $Ca = 0.1875$. The drop and the carrier fluid have the same density ($\rho_r = 1$). Each combination of Capillary number and viscosity ratio is analysed for different values of the refinement factor (and thus different grid resolutions).
Indicating with $L$ and $B$ the major and minor axes of the drop (see the sketch in Fig. 1.11), the deformation parameter, $D$, can be computed as follows:

$$D = \frac{L - B}{L + B} \tag{1.70}$$

An analytical solution for the behaviour of $D$ as a function of $Ca$ was obtained by Taylor [97, 98] for an unbounded flow, and later extended by Shapira & Haber [99] to account for lateral confinement effects.

$$D = \frac{16 + 19\eta_r}{16 + 16\eta_r} Ca \left[ 1 + C_{SH} \frac{3.5}{2} \left( \frac{d}{4h} \right)^3 \right] \tag{1.71}$$

where $C_{SH} = 5.6996$ is a numerical coefficient [99]. This equation is proven to be accurate also for two-dimensional and three-dimensional drops at small $Ca$, i.e., in the limit of small deformations [100, 101, 102].
The behaviour of the deformation parameter $D$ as a function of the Capillary number, $Ca$, is shown in Fig. 1.12. Panel a refers to the cases with drop-to-fluid viscosity ratio $\mu_r = 0.1$, while panel b refers to the cases with drop-to-fluid viscosity ratio $\mu_r = 1$. For all considered cases, we find a good agreement between the numerical simulations (symbols, each referring to a specific grid resolution for $\phi$), and the analytical solution, with minor differences for the viscosity ratio $\mu_r = 0.1$ (discrepancy between theoretical and numerical results below 10%). In addition, we observe almost no difference between the results obtained by the grid $G1$ (same grid for NS and CH), grid $G2$ (grid for CH two times finer than grid for NS), and grid $G4$ (grid for CH four times finer than grid for NS). This shows the consistency of the proposed implementation and suggests that, when the flow field is resolved on a fine enough grid, the dual-grid approach gives a final result that is identical to the result that could be obtained by a simulation performed on the fine grid for both velocity and phase-field.

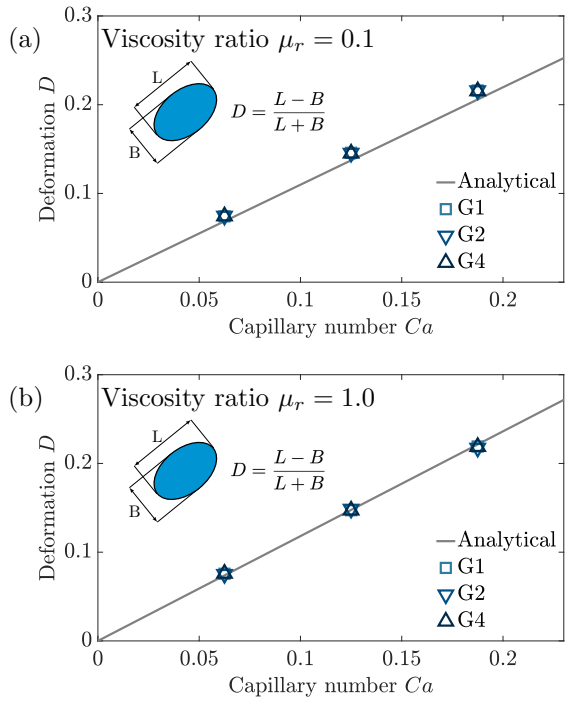


FIGURE 1.12 – Behaviour of the deformation parameter $D$ (see sketch) as a function of the Capillary number, $Ca$, for a drop in a two-dimensional shear flow: comparison between the numerical results (symbols) and analytical predictions (continuous black lines). Two different viscosity ratios are considered: $\mu_r = 0.1$ (panel a) and $\mu_r = 1.0$ (panel b). The different symbols refer to the different refinement factors employed: light blue squares (case $G1$), blue down-facing triangles (case $G2$), upward-facing dark blue triangles (case $G4$).

It is therefore important now to evaluate the computational efficiency of the proposed technique. To characterize the computational efficiency of the proposed approach we measure the wall-clock time required for a single time step and the memory usage using different refinement factors $M_i$. Results are shown in Fig. 1.13. The results reported are associated to the same case run ($Ca = 0.062$) and are normalized using simulation G1 as a reference, where the grid for both the Navier-Stokes and the Cahn-Hilliard equations is the finest and thus the computational cost is the highest. The same HPC-cluster and set-up were used, and the simulations were performed using the same number of MPI tasks (64). Considering the results reported, we can see that employing the dual-grid approach, it is possible to save up to 27% in wall-clock time and memory usage for a refinement factor equal to 2 (i.e. CH is solved on a grid that is two times finer than that used for NS, case $G2$), and up to 38% in time and memory for a refinement factor of 4 (i.e. CH is solved on a grid that is four times finer than the one used for NS, case $G4$), compared to the case in which the finest grid is used for both CH and NS (case $G1$). Clearly, the efficiency should further increase in three-dimensional scenarios, which have greater requirements in terms of computational time and memory, making this strategy very appealing for simulations

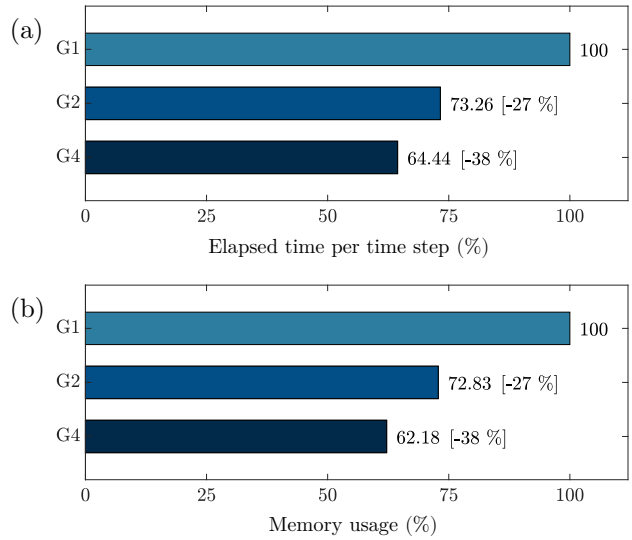


FIGURE 1.13 – Computational efficiency of the dual-grid approach: elapsed time (wall-clock) for a time step (panel a) and memory usage (panel b). Results are normalized using case $G1$ as reference, where the finest grid is used for all equations. Light blue bars refer to case $G1$ (same grid), blue bars to case $G2$ (refinement factor equal to 2) and dark blue bars to case $G4$ (refinement factor equal to 4).

of complex three-dimensional flows.

# 2

# Capillary waves in two-layer oil-water channel flow

**Reproduced in part from:**
G. Giamagas, F. Zonta, A. Roccon & A. Soldati, (2023) *Propagation of capillary waves in two-layer oil-water turbulent flow*, Journal of Fluid Mechanics, 960, A5.

The flow of two immiscible fluids is often encountered in the petroleum industry, where crude oil and water – upon extraction from wells – are transported over very long distances and finally separated in designated process plants. When oil and water flow together inside horizontal pipelines and channels, different flow regimes are possible. At low flow rates, the flow is stratified and the oil-water interface is smooth. At moderate flow rates, the flow can still remain stratified, but the oil-water interface is characterized by the presence of waves, which are initially long compared to the pipe diameter/channel height, and become shorter as the flow rate is increased. At even higher flow rates, waves might break and generate a dispersed flow in which water drops form inside the oil layer and/or oil drops form inside the water layer [5, 6]. Because of the inherent modelling complexity of the flow, literature in the field of oil-water transportation inside pipes and channels is almost entirely based on experimental investigations – focused mainly on the evaluation of flow regimes/global flow properties, like pressure drop and flow rate [8] – and on single point measurements of the interface deformation [14], but also on analytical investigations of flow stability [103, 104].

More detailed experimental observations, aiming at characterizing the flow structure and the interface deformation, have become possible in the last years, thanks to the development of laser based diagnostic techniques like Planar Laser-Induced Fluorescence (PLIF) and Particle Image/Tracking Velocimetry (PIV/PTV). In particular, PLIF provides information on the scalar distribution of the two phases in the plane of the laser light, while PIV/PTV can provide the corresponding instantaneous velocity distribution. These techniques are generally applied to cases in which the two fluids have the same refractive index, RI [105, 106], in order to minimize the optical distortion at the liquid-liquid interface. Similar techniques have also been applied to gas-liquid systems, including horizontal stratified air-water flow in pipes [107, 108, 109], and

even gas-liquid annular flow [110]. Very recently, a new simultaneous two-line (two-colour) technique, combining PLIF and PIV/PTV for non RI-matched fluids, has been developed [111, 112], and is expected to contribute further to the research in the field. Given the difficulties in obtaining accurate experimental results of interfacial flows, time and space-resolved numerical simulations – although complex and computationally expensive to perform – are a valuable tool to provide insightful measurements of the entire flow field and to offer a corresponding precise characterization of the liquid-liquid interface deformation. Compared to the case of gas-liquid flows, in which the number of accurate simulations is rapidly increasing [113], the case of liquid-liquid flows has gathered relatively less interest, which is however currently rising thanks to the renewed interest in the water-lubricated oil pipelines [114, 115]. Previous works [30, 4, 116] have employed pseudo-spectral Direct Numerical Simulation (DNS) of turbulence, coupled with a Phase-Field Method (PFM) to study the dynamics of immiscible, stratified liquid-liquid flow inside plane channels. However, a detailed space-time characterization of the liquid-liquid interface in such a configuration is not yet available. This is exactly the subject of the present chapter. We consider two immiscible fluid layers that move, under the action of an imposed mean pressure gradient, inside a plane channel. The two fluid layers have same thickness and same density. Two sets of parametric studies are performed, the first varying the viscosity of one fluid with respect to the other and the second varying the surface tension between the fluids. We combine pseudo-spectral DNS of turbulence with PFM to track the dynamics of the liquid/ liquid interface. Upon application of space and time-resolved flow measurements, we are able to compute the spectral properties of the liquid-liquid interface and discuss them in the context of the Wave Turbulence Theory (WTT) [117, 118, 119, 120].

It is important to note that the waves that form in a stratified oil-water system are extremely interesting also from a fundamental viewpoint: due to the similar density of the two fluids, the influence of gravity is ruled-out and the entire evolution of the interfacial waves is dominated by surface tension. This represents a convenient numerical setup, which gives us the possibility to challenge current understanding of capillary waves propagation [121, 122]. Obtaining similar results with larger density difference fluids would otherwise require complex experimental measurements to be performed in microgravity conditions [123].

## 2.1 Viscosity effects

The effects of the variation of the viscosity ratio between the two fluid layers on both the flow and the interface dynamics are examined here.

### 2.1.1 Simulation setup

We consider two immiscible fluid layers flowing inside a rectangular channel under the effect of a constant mean pressure gradient. The channel has dimensions $L_x = 8\pi h$, $L_y = 2\pi h$ and $L_z = 2h$, along the streamwise ($x$), spanwise ($y$) and wall-normal ($z$) directions, respectively. The two layers have the same thickness – so that the initially undeformed interface is located at a distance $h$ both from the top and from

the bottom wall – and same density, $\rho_1 = \rho_2 = \rho$, but different viscosity, $\mu_1 \neq \mu_2$ (and hence different kinematic viscosity, $\nu_1 \neq \nu_2$). The interface between the two fluids has a constant and uniform surface tension, $\sigma$. A sketch of the domain geometry, along with an instantaneous visualization of the interface topology is provided in Fig. 2.1. Two different cases characterized by the same value of the reference shear Reynolds number, $Re_\tau = 300$, and Weber number, $We = 1.0$ are considered. The viscosity ratio between the two fluids is $\mu_r = 1.00$ for the first case, and $\mu_r = 0.25$ for the second case. The values of the physical parameters are chosen to mimic a situation in which a light industrial oil (Exxon Mobil Solvesso 200 ND) with $\rho = 980\ \ kg/m^3$, $\mu_2 = 3.85 \times 10^{-3}\ \ Pa\ \ s$ and $\sigma = 0.044\ \ N/m$ flows together with water inside a channel of height $2h = 6 \times 10^{-2}\ \ m$, at a reference shear velocity of $u_\tau = 3.8 \times 10^{-2}\ \ ms^{-1}$. Note that the reduction of the viscosity in the upper layer leads to a corresponding increase of the local Reynolds number, which can be estimated as $Re_{\tau,1} \approx Re_\tau/\mu_r$. As a consequence, the number of grid points $N_x \times N_y \times N_z$ must increase for decreasing $\mu_r$, in order to maintain a suitable resolution. To ensure a correct representation of the interface dynamics, all simulations are run for $Ch = 0.02$ and $Pe = 3/Ch = 150$ [43]. For both simulations, the initial condition is taken from a preliminary simulation of a single-phase flow at $Re_\tau = 300$, on top of which we properly define the initial distribution of the phase-field, $\phi$ so that the liquid-liquid interface is at the beginning flat and located at the channel centre. The main simulation parameters are summarized in Tab. 2.1.

| Simulation | $Re_\tau$ | $We$ | $N_x$ | $N_z$ | $N_y$ | $L_x$ | $L_y$ | $L_z$ |
|---|---|---|---|---|---|---|---|---|
| $\mu_r = 1.00$ | 300 | 1.0 | 1024 | 513 | 256 | $8\pi h$ | $2\pi h$ | $2h$ |
| $\mu_r = 0.25$ | 300 | 1.0 | 2048 | 513 | 1024 | $8\pi h$ | $2\pi h$ | $2h$ |

TABLE 2.1 – Overview of the main simulation parameters at variable viscosity ratio.

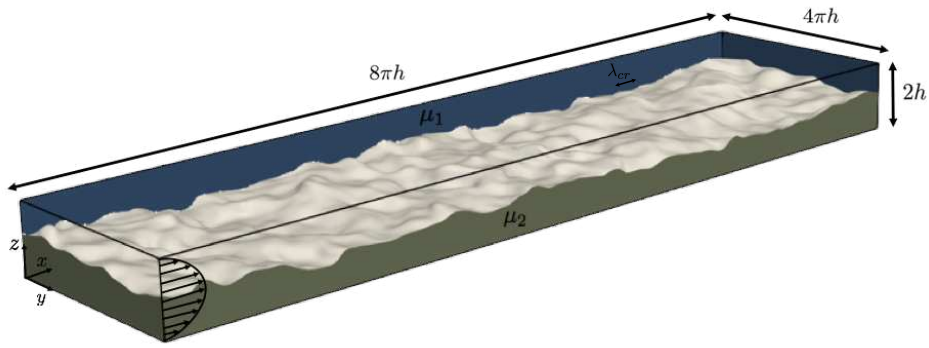


FIGURE 2.1 – Sketch of the computational domain. Two immiscible fluid layers, with viscosity $\mu_1$ (upper layer) and $\mu_2$ (lower layer) flow inside a plane channel under the action of an imposed pressure gradient. The instantaneous liquid-liquid interface deformation is shown in white.

### 2.1.2 Statistics of the turbulent flow field

We first look at the flow statistics for the different cases considered in this work. In Fig. 2.2a, we show the mean streamwise velocity, $\langle u(z)/u_\tau \rangle$, as a function of the wall-normal coordinate. Results for the two-layers configuration at different viscosity ratio ($\mu_r = 1.00$ and $\mu_r = 0.25$) are shown together with the reference single-phase (SP) case. When the two layers have the same viscosity ($\mu_r = 1.00$), the mean velocity profile is only slightly modified by the presence of the liquid-liquid interface. However, when the upper layer has a lower viscosity ($\mu_r = 0.25$) the mean streamwise velocity is consistently increased, and its shape much more modified. This reflects into an overall flow rate increase of about 11% (see Tab. 2.2), which can be traced back to a corresponding drag reduction (since our simulations are all run at the same pressure gradient). Note that the location at which the streamwise velocity has a maximum (represented by the dashed horizontal lines in Fig. 2.2a) is changed. In particular, for $\mu_r = 0.25$, the maximum is shifted upwards with respect to the channel centre, and indicates the tendency for the streamwise velocity profile to be skewed when the two layers have different viscosity. This is also highlighted in the corresponding profiles of the mean strain rate, $\langle du/dz \rangle$, shown in Fig. 2.2b. In particular, in the inset of Fig. 2.2b one can observe that the location of the zero crossing of the mean strain rate is shifted upwards for the case $\mu_r = 0.25$, while it occurs at the centreline for the other two cases. Notice that this asymmetry for the case $\mu_r = 0.25$ leads to a purely positive value of the mean strain rate close to the average interface position, $z = 0$. The probability density function of the instantaneous strain rate, $du/dz$, computed at the instantaneous interface position and normalized by its root mean square value, $\langle (du/dz)^2 \rangle^{1/2}$, for each case, is shown in Fig. 2.3. In both cases, the probability density functions are fitted very well by the Gaussian distribution, however with a different mean value, namely $\alpha = 0$ for the case $\mu_r = 1.00$ and $\alpha = 0.4$ for the case $\mu_r = 0.25$.

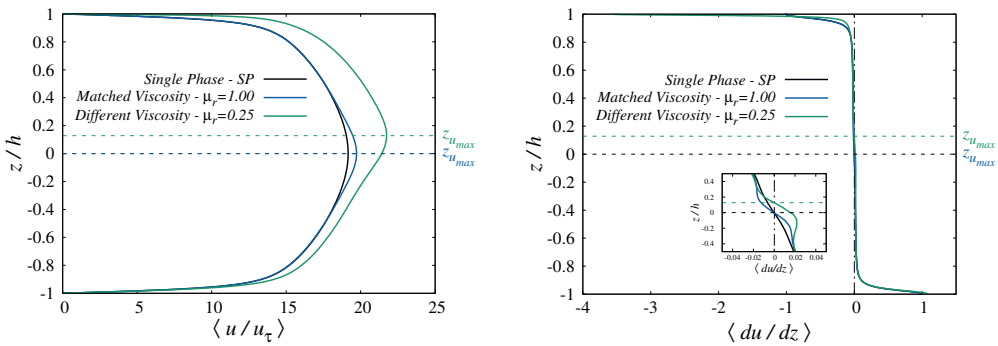


FIGURE 2.2 – Left: Mean streamwise velocity profiles, $\langle u(z)/u_\tau \rangle$, as a function of the wall-normal distance $z/h$, for the three different cases: $\mu_r = 1.00$ (blue line), $\mu_r = 0.25$ (green line), single-phase flow (SP, black line). Also shown (horizontal dashed lines, $z_{u_{max}}$) is the location at which the mean streamwise velocity profiles have a maximum. Right: Mean strain rate profiles, $\langle du/dz \rangle$, as a function of the wall-normal distance $z/h$, for the three different cases. The inset shows a close-up view of the mean strain rate profile in the region $-0.5 < z/h < 0.5$.

Considering the key role of the layer viscosity on the overall flow field, it is also interesting to show the behaviour of the mean streamwise velocity profiles in wall

| Simulation | $Q_1/Q_{SP}$ | $Q_2/Q_{SP}$ | $Q_t/Q_{SP}$ | $\Delta Q\%$ |
|---|---|---|---|---|
| Single-phase | - | - | 1.0000 | - |
| $\mu_r = 1.00$ | 0.5035 | 0.5034 | 1.0069 | 0.69 |
| $\mu_r = 0.25$ | 0.5807 | 0.5316 | 1.1123 | 11.23 |

TABLE 2.2 – Mean flow rates for the different simulations. $Q_1$, $Q_2$ and $Q_t$ correspond to the mean flow rates of the upper layer (oil), the lower layer (water) and the total mean flow rate over the whole channel height respectively, while $Q_{SP}$ is the mean flow rate of the reference single-phase flow. The quantity $\Delta Q\%$ stands for the percent increase in mean flow rate between the multiphase and the single-phase flow simulations.

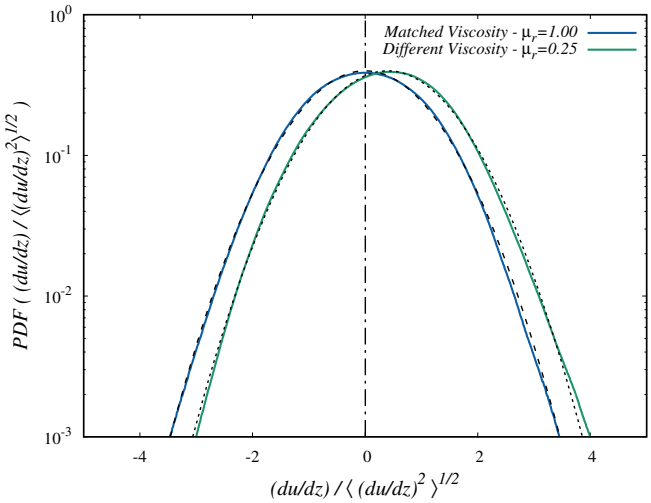


FIGURE 2.3 – Probability density function of the normalized strain rate $du/dz/\langle(du/dz)^2\rangle^{1/2}$ for cases $\mu_r = 1.00$ (blue line) and $\mu_r = 0.25$ (green line). The Gaussian distributions with mean values $\alpha = 0$ , $\alpha = 0.4$ and unit standard deviation are shown with a dashed and a dotted black line respectively.

units. This can be done via a semi-local scaling [95, 4, 116], which makes use of the local value of the friction velocity:

$$u_{\tau,loc} = u_\tau \sqrt{\frac{2|\tau_{w,1}|}{|\tau_{w,1}|+|\tau_{w,2}|}} \tag{2.1}$$

to rescale the different profiles, as shown in Fig. 2.4. Note that $\tau_{w,1}$ and $\tau_{w,2}$ are the values of the shear stress at the two walls. The wall normal coordinate in wall units reads as $z^+ = z(u_{\tau,loc}/\nu)$. Panel a refers to the lower layer while panel b refers to the upper layer. The classical law of the wall, $u^+ = z^+$ and $u^+ = (1/k)\log(z^+) + 5$, with $k = 0.41$ the von Kármán constant, is also shown by a dashed line for comparison purposes. At the lower layer (Fig. 2.4*a*), all the velocity profiles follow the classical law of the wall. This indicates that the presence of the interface induces only negligible effects on the near-wall turbulence cycle. A similar situation is also observed at the

upper layer (Fig. 2.4*b*), with all numerical results following fairly well – when rescaled in local wall units – the law of the wall. Naturally, for $\mu_r = 0.25$, the outer layer is extended compared to $\mu_r = 1.00$. The influence of the viscosity ratio on the near-

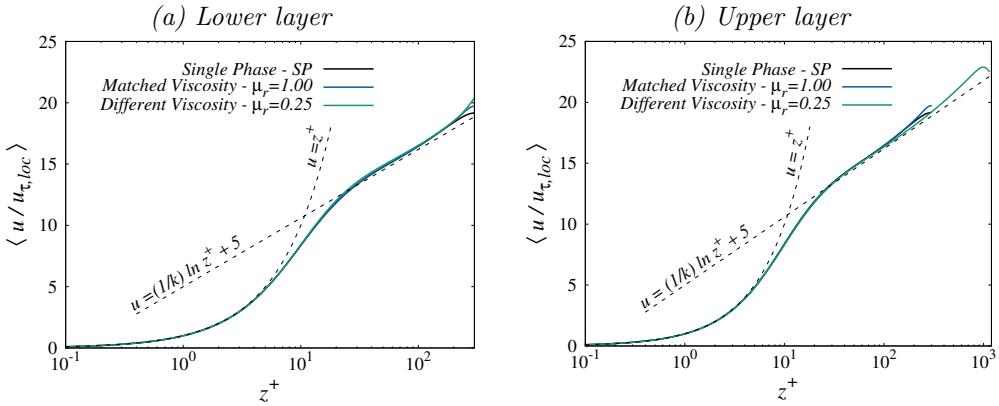


FIGURE 2.4 – Mean streamwise velocity profiles at the lower layer (panel a) and at the upper layer (panel b) rescaled in wall units using the local friction velocity at the corresponding wall. Also shown (dashed line) is the classical law of the wall: $u^+ = z+$ and $u^+ = (1/k)\log(z^+) + 5$ (where $k = 0.41$ is the von Kármán constant).

wall turbulence structure becomes rather apparent by looking at the fluctuations of the streamwise velocity, $u'$, on $x - y$ planes located near the top and bottom walls. Results are presented in Fig. 2.5. In particular, panel a refers to a distance of $z^+ = 30$ from the bottom wall, while panel b refers to a distance of $z^+ = 30$ from the top wall. We notice the presence of regions with higher (dark green) and lower (light green) than mean streamwise velocity, called high- and low-speed streaks, respectively. It is apparent that, as viscosity is decreased, turbulence structures become finer and their distribution more complex.

### 2.1.3 Forcing of the liquid-liquid interface by turbulence

The liquid-liquid interface is naturally forced by turbulence over a broad range of scales, from the larger ones, whose size is of order of the channel height, down to the smaller dissipative scales. An example of the spatial distribution of the wall-normal velocity $w$ on two x-y parallel planes for the case $\mu_r = 0.25$ is shown in Fig. 2.6. The two planes are located at $z/h = -0.3$ (below the minimum wave trough, panel a), and at $z/h = 0.3$ (above the maximum wave crest, panel b), so that statistics represent the turbulence activity around the interface. Regions of positive and negative velocity fluctuations, of different size and shape, populate the region near the interface. As expected, the size of the structures in the upper layer, where viscosity is lower, is smaller. A quantitative measure of such spatial distribution can be obtained by looking at the power spectra of the vertical velocity fluctuations at the two parallel planes. This is shown in Fig. 2.7. Panel a refers to the plane below the waves, while panel b refers to the plane above the waves. Also shown in this figure (grey area) is the

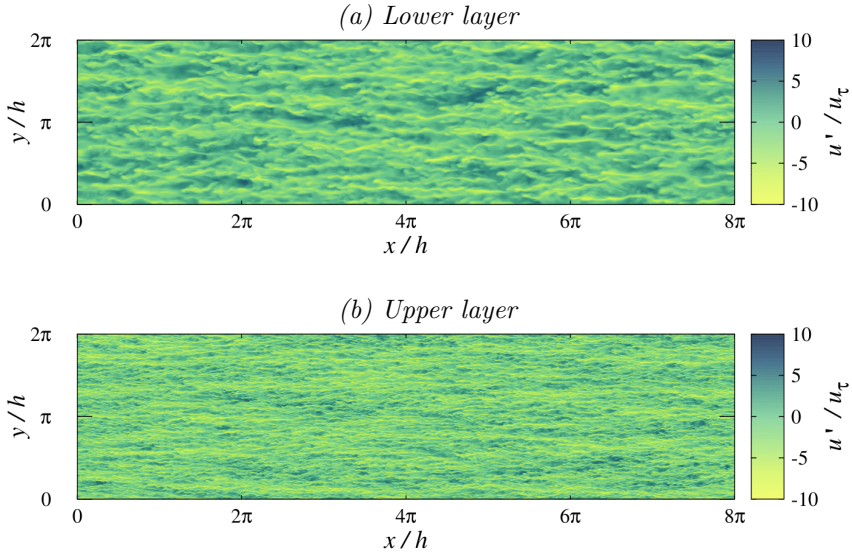


FIGURE 2.5 – Contour-maps of streamwise velocity fluctuations, $u'$, on wall–parallel $x-y$ planes located at $z^+ = 30$ from the walls, for the case $\mu_r = 0.25$. Panel (a): $x-y$ plane near the bottom wall. Panel (b): $x-y$ plane near the top wall.

forcing range of scales, going from largest, energy-injection scales – indicated as $k^+_{LS}$ and corresponding to channel height $2h$ – downwards. We observe that, below the interface (panel a), the forcing applied by turbulence does not change with $\mu_r$, and is consistent with literature results [124]. Above the interface, turbulence forcing at large scales (around $k^+_{LS}$) does not change significantly as well, even when we decrease $\mu_r$. What changes is the forcing at small scales.

The dynamics of the interface separating the two fluid layers depends on the competition between two opposite effects: the destabilizing effect of shear and turbulence, and the stabilizing effect of surface tension (we recall that gravity does not play a role here because the two fluid layers have the same density). A simplified picture of the generation of a capillary wave through the competition of inertial (turbulent) and capillary (surface tension) forces at the interface is sketched in Fig. 2.8. Initially, a vertical velocity fluctuation denoted as $w$, encounters the undeformed interface. A pressure, $p'$ proportional to $\rho w^2$ is exerted on the interface, due to inertia. Once the interface deforms a capillary stress acting normal to the interface and being proportional to the local curvature, $\kappa$ and to the magnitude of surface tension, $\sigma$ resists the further deformation, thus stabillizing the wave profile. At this stage waves begin to propagate in order for the interface to restore equilibrium by recovering its original undisturbed position. The influence of turbulence forcing on the wave dynamics will be discussed in more detail in Sec. 2.1.5 and Sec. 2.1.6.

Finally, it is interesting to point out that the wave growth in the oil-water turbulent flow examined here shares some similarities with the wave growth at the surface of the ocean by a turbulent wind. Indeed, in both cases the wave growth is initially triggered by the forcing of the turbulent fluctuations of the pressure fields above the water

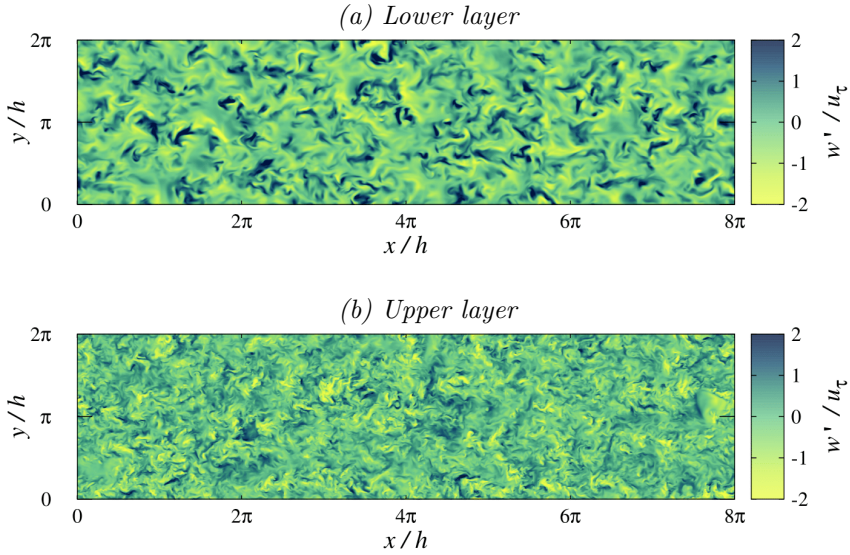


FIGURE 2.6 – Contour-maps of wall-normal velocity fluctuations, $w$, on wall–parallel $x-y$ planes located near the interface, for the case $\mu_r = 0.25$. Panel (a): $x-y$ plane below the interface, in the lower layer, at $z/h = -0.3$. Panel (b): $x-y$ plane above the interface, in the upper layer, at $z/h = 0.3$.

surface [133]. Later on, when the first low amplitude waves have been developed, the wave shape influences the air stream and the wave growth is further promoted by the instability mechanism induced by the coupling between the wave profile and the mean air flow above [134], as well as by sheltering effects due to the pressure mismatch between the windward and leeward wave side [135]. Nevertheless, there are also some notable differences between the wave growth in the Poiseuille oil-water flow and the wind-driven wave generation at the ocean surface. First, in the wind-driven water waves there is a density mismatch between the two fluids, which gives rise to the presence of a restoring gravity force as well as of an asymmetric forcing. In the Poiseuille oil-water flow, the gravity force is zero, and the interface is forced on both sides in a nearly symmetric manner - with only a small asymmetry induced by the mismatch in viscosity in the case $\mu_r = 0.25$. In addition, in the Poiseuille oil-water flow the interface is advected at the maximum mean velocity observed at the channel centre, and the shear stress is minimum at that location, which is another important difference when compared to the turbulent boundary layer developed at the air side during wind-driven wave generation. The lack of a velocity difference across the interface excludes one of the main mechanisms with which waves are generated in two-phase mixing layers according to the Kelvin-Helmholtz instability [136]. In general, the problem of wave growth is a fundamental problem, which is relevant in a number of different fields (from environmental and geophysical sciences, to chemical and industrial ones) and has been studied theoretically, experimentally and numerically in a number of different conditions. The latest advances in numerical methods and computer power allows for fully-resolved two-phase simulations, which can provide detailed databases

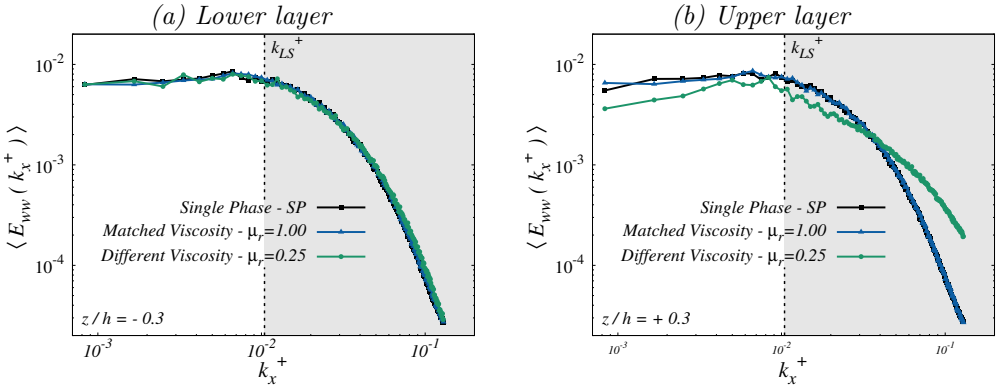


FIGURE 2.7 – Streamwise wavenumber spectrum of the vertical velocity fluctuations, $E_{ww}$, averaged in time, computed on wall-parallel planes $x-y$ below the interface (at $z/h=-0.3$, panel a) and above the interface (at $z/h=0.3$, panel b). Results for $\mu_r=1.00$ and $\mu_r=0.25$ are shown together with the results obtained for the reference single-phase flow.

and tackle all the underlying complexity of these flows. Indeed, recently performed numerical simulations of water wave growth [25, 28, 29] have provided valuable insight on the mechanisms that drive the wave growth at its different stages. The wave growth under different conditions in terms of forcing mechanisms and different fluid properties such as viscosity and density ratio still requires further investigations. As more simulation and experimental data become available, it would be interesting in the future to compare the wave-turbulence coupling under all these various conditions.

### 2.1.4 Characterization of the wave field

The outcome of the competition between inertial and capillary forces determines the behaviour of the interface evolution, which is ultimately characterized by the propagation of waves with different amplitudes and wavelengths. This is well represented by the instantaneous interface shape shown in Fig. 2.1. We measure the root mean square of the interface elevation, $\sigma_\eta = \overline{\eta^2(x,y,t)}^{1/2}$, and the typical wave steepness, $\sigma_s = \left\langle \sqrt{1/S \int_S ||\nabla\eta||^2(x,y,t)dxdy} \right\rangle$, where $\eta$ is the amplitude of the interface elevation and $S$ is the surface area of the interface. Overbars indicate averaging in space along the two homogeneous directions $x$ and $y$, while angular brackets indicate average in time. After a transient in which waves grow starting from the initial flat interface, $\sigma_\eta$ and $\sigma_s$ reach the statistically-steady value reported in Tab. 2.3. Also listed in the same table is the value of the non-dimensional depth parameter $d=k_p h$, where $k_p$ corresponds to the wavenumber of the most energetic wave (discussed below). Reportedly, the wave propagation can be considered a linear process if $\sigma_s \ll 1$ [125]. Since this condition is not met in the present case, nonlinear effects can be significant. In addition, the influence of the fluid layer depth is negligible when $d \gg 1$ (deep water approximation). Even in this case, since the condition is not fulfilled, we cannot a-priori exclude some influence of the top and bottom wall on the dynamics of interfacial waves. From the results summarized in Tab. 2.3, we notice that the

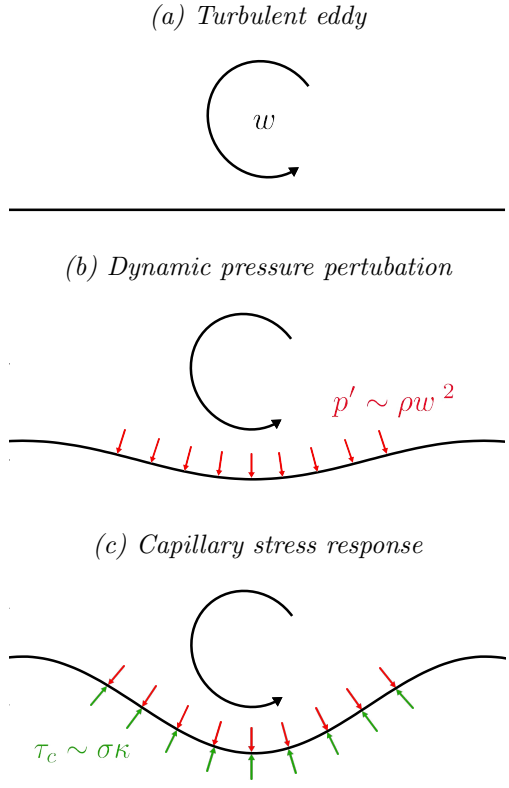


FIGURE 2.8 – Wave generation by turbulence. Panel (a) : a turbulent eddy encounters the undeformed interface at $t = 0$. Panel (b): the interface deforms as a result of the dynamic pressure, $p'$, which is proportional to the square of the vertical velocity, $w$. Panel (c): capillary stress, $\tau_c$ proportional to the the local curvature of the interface, $\kappa$, resists the deformation.

reduction of $\mu_r$ (i.e. reduction of the viscosity of the upper layer) has a significant effect on the interface elevation ($\sigma_\eta$ reduces by $\approx 15\%$), but only a small effect on the wave steepness ($\sigma_s$ reduces by $\approx 5\%$). This reduction in wave height for the case $\mu_r = 0.25$ is presumably due to the increased strain rate exerted on the interface in that case, as it was shown in section Sec. 2.1.2.

### 2.1.5 Frequency spectra

To characteride the propagation of waves at the liquid-liquid interface, we look at the frequency power spectrum of wave elevation, $\overline{\langle S_\eta(f)\rangle}$. Spectra are averaged in space, over all points of the interface, and in time, over $N_s = 14$ independent realizations sampled by the same probe. Results are shown in Fig. 2.9 for both $\mu_r = 1.00$ and $\mu_r = 0.25$. The frequency axis is normalized by the frequency $f_p$ at which the peak of the spectra is observed ($f_p$ does not change by changing $\mu_r$). The lower boundary in the frequency range reported in the plot corresponds to the inverse of the channel crossing time, $t_c = L_x/\overline{u}_c$, where $\overline{u}_c$ is the mean streamwise velocity

| Simulation | $\sigma_\eta/h$ | $\sigma_s$ | $d$ | $\overline{u_c}/u_\tau$ |
|---|---|---|---|---|
| $\mu_r = 1.00$ | 0.136 | 0.374 | 0.5 | 19.0 |
| $\mu_r = 0.25$ | 0.116 | 0.350 | 0.5 | 21.0 |

TABLE 2.3 – Overview of the wave field characteristics for the variable viscosity ratio simulations. The first column shows the two simulations performed at different viscosity ratios, $\mu_r = 1.00$ and $\mu_r = 0.25$. The second column shows the statistically-steady value of the root mean square of the interface elevation, $\sigma_\eta$, while the third shows the typical wave steepness, $\sigma_s$. The fourth column shows the depth parameter, $d$ and the fifth the mean velocity at the channel centre, $\overline{u_c}$.

at the channel centre (i.e., the velocity at which the interface is advected by the bulk fluid motion) for the case $\mu_r = 1.00$. Note that $\overline{u}_c$ (whose value is reported in Tab. 2.3) is slightly higher for $\mu_r = 0.25$, due to the viscosity reduction in the upper layer. The upper boundary in the frequency range reported in the plot is the frequency at which the interface elevation signal is sampled. Also shown in Fig. 2.9 are the theoretical predictions (solid and dashed lines) obtained in the context of the Wave Turbulence Theory (WTT). In particular, assuming weak nonlinearities and negligible dissipation, WTT predicts – for pure capillary waves – a steady state regime in which energy is transferred from the injection scale down to the dissipation scale [118, 126]. Far from the injection and the dissipation scales, an inertial regime with scaling $S_\eta(f) \sim f^{-17/6}$ (dashed line) is predicted. This scaling has been previously observed in experiments performed using a mechanical wave maker – characterized by a narrow-band low-frequency forcing, and by a large scale separation between the low-frequency forcing and the high frequency dissipation region [10] –, but also in numerical simulations under similar conditions [24]. Note that, for two immiscible fluids of same density, WTT predicts in the inertial regime the scaling $S_\eta(f) \sim f^{-8/3}$, and not $S_\eta(f) \sim f^{-17/6}$, as a result of four-wave interactions instead of three-wave interactions [11]. In our simulations, a wide inertial regime with scaling $S_\eta(f) \sim f^{-8/3}$, is not clearly observed, for different reasons. First, as mentioned above, the influence of nonlinearities and dissipation cannot be excluded a-priori. But also, and perhaps of greater importance, in our system we do not have a clear scale separation between the scale of energy injection (forcing) and the scale of energy dissipation. Energy is injected at the interface by turbulent fluctuations over a broad range of scales, from the larger ones – which scale with the channel height –, down to the smallest ones, which include also the smallest scales at which energy is dissipated. At low frequencies (in the region $f/f_p < 7$), and before the frequencies of energy injection, the spectrum is compatible with the scaling $S_\eta(f) \sim f^{-1}$, which is expected in case of energy equipartition among large scales [127, 128], and corresponds to a vanishing average energy flux through scales. An experimental confirmation of this scaling has been obtained only recently, via measurements in the absence of gravity [123]. Therefore, the present numerical configuration seems to offer a convenient setting for the assessment of important theoretical predictions.

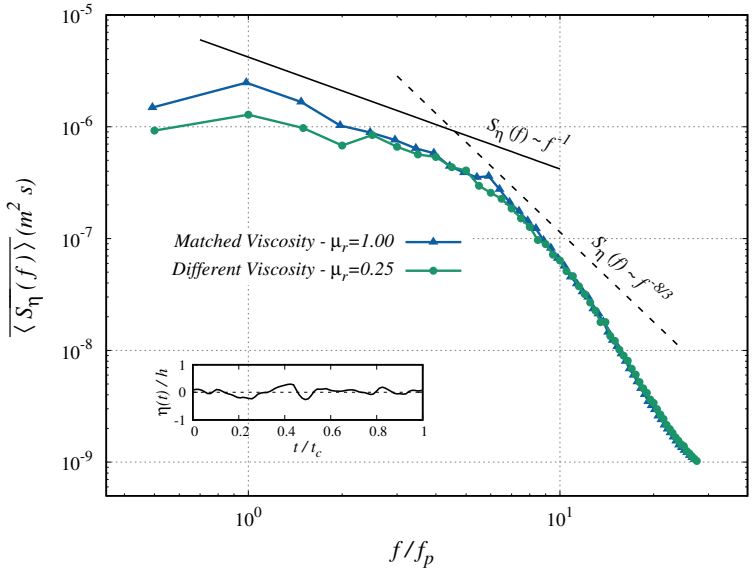


FIGURE 2.9 – Frequency power spectrum of wave elevation, $\overline{\langle S_\eta(f)\rangle}$, averaged in space and time (over 14 independent realizations sampled by the same probe). Results are shown for $\mu_r = 1.00$ (blue triangles) and $\mu_r = 0.25$ (green bullets). The theoretical scalings proposed in literature for the inertial range, $f^{-8/3}$ (dashed line), and for the low frequency, large-scale, range, $f^{-1}$ (solid line), are also shown for comparison. The behaviour of the interface deformation in time, recorded at a given location in space, is shown in the inset.

### 2.1.6 Wavenumber spectra

Wavenumber power spectra of wave elevation computed along the streamwise direction, and averaged in space (only along the spanwise direction, $y$) and in time, $\overline{\langle S_\eta(k_x)\rangle}$, are shown in Fig. 2.10. As done for the frequency spectrum, we normalize the wavenumber axis by the wavenumber $k_p$ at which the peak of the spectra is observed ($k_p = 4\pi/L_x$ for both values of $\mu_r$). In Fig. 2.10, the wavenumber axis ranges between a lower boundary, which corresponds to the entire domain length, and an upper boundary $k_N/k_p$ (highlighted by a vertical dotted line), which corresponds to the shortest wavelength that can be captured. From geometrical considerations, and recalling that the extension of the transition layer between the two phases is $4Ch$, this wavelength is $\lambda_N = 8Ch$ (corresponding to a completely bent interface), hence giving a wavenumber $k_N = \pi/(4Ch)$. Theoretical predictions, mostly derived in the context of WTT (solid, dashed and dashed-dotted lines) are also shown in Fig. 2.10. For the reasons already presented above (see the discussion about the frequency spectra), even in this case we do not observe a wide inertial range with scaling $S_\eta(k) \sim k^{-4}$, as predicted by WTT. We recall here that, as already mentioned, capillary wave turbulence between two immiscible fluids of same density is the result of four-waves – and not three-waves – interactions, therefore leading to $S_\eta(k) \sim k^{-4}$ instead of $S_\eta(k) \sim k^{-15/4}$. In addition, at high wavenumbers, we observe a steeper slope, which follows the scaling $k^{-6}$, as indicated by the dot-dashed line in Fig. 2.10. A similar scaling was reported in

previous experimental observations of wave dynamics at the free surface of a turbulent open channel flow [129]. This sharp decay of the wavenumber spectrum was ascribed by the authors to the non-negligible effects of wave nonlinearities and dissipation that – even though neglected by the theory – can play a role in the propagation of small scale waves in many cases of practical interest. The observed behaviour can be physically explained by looking at the dynamics of wave generation by turbulence. We recall that the dynamics of waves is driven by the balance between destabilizing and stabilizing forces. Waves are generated and sustained by vertical velocity fluctuations $w'$ [25, 27], while they are stabilized by surface tension. At the channel centre, the energy of velocity fluctuations is distributed among eddies of different sizes, from the largest ones, with size of the order of the channel height, to the smallest ones, with size of the order of the small dissipative scales. The larger eddies are also the most

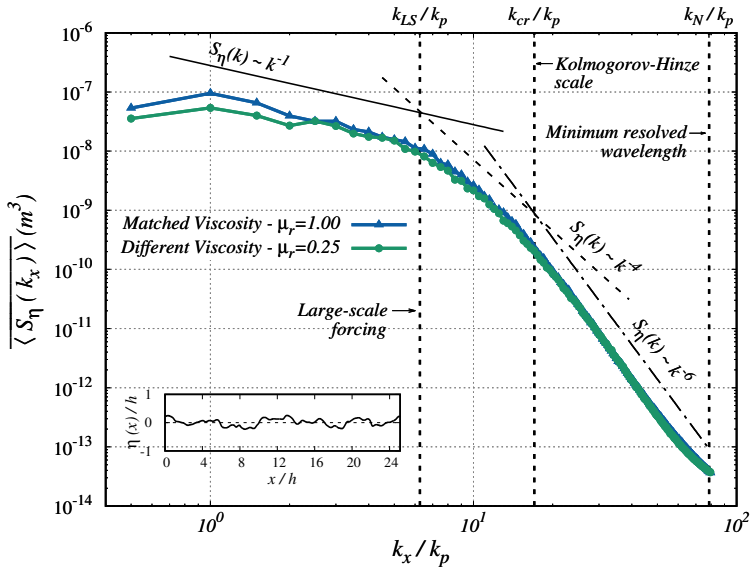


FIGURE 2.10 – Streamwise wavenumber power spectra of wave elevation, $\overline{\langle S_\eta(k_x)\rangle}$, averaged in space (over the spanwise direction) and in time. Results are shown for $\mu_r = 1.00$ (blue triangles) and $\mu_r = 0.25$ (green bullets). Theoretical scalings proposed in literature for the inertial range, $k^{-4}$, for the low-wavenumber, large-scale range, $k^{-1}$, and for the high-wavenumber regime, $k^{-6}$ are also shown for comparison. The three vertical dotted lines correspond to the large scales forcing , $k_{LS}$, to the critical wavenumber, $k_{cr}$, at which surface tension and inertial forces are balanced, and to the numerical cut-off, $k_N$, which identifies the highest wavenumber that can be captured. The behaviour of the instantaneous interface deformation along the streamwise direction, monitored at a given spanwise position, is shown in the inset.

energetic ones, and thus induce, upon impact on the interface, the larger deformation. On the other hand, surface tension forces act to restore the interface back to its equilibrium position and, being proportional to the curvature of the interface, are stronger for shorter waves. Therefore, assuming that the generation of a wave with wavelength $\lambda$ is triggered by a turbulent eddy of equal size, a critical Weber number exists, $We_{cr} = \rho\overline{w'}^2\lambda_{cr}/\sigma$, at which surface tension and inertial forces are balanced. The critical wavelength, $\lambda_{cr}$, marks the threshold between longer waves that can grow

in amplitude due to the strong inertial forces, and shorter waves that do not grow because of the overwhelming effect of the restoring surface tension forces and of the increasing role of dissipation at large wavenumbers [14, 130, 24, 120]. This consideration is similar to the one postulated by [131] and recalled by [132] to estimate the maximum size of a drop/bubble that will not break in a given turbulent flow, i.e. $D_{cr} = 0.725\,(\rho/\sigma)^{-3/5}\,|\epsilon_c|^{-2/5}$, with $\epsilon_c$ the turbulent kinetic energy dissipation. Using this semi-empirical prediction, and applying it to the present case in which the characteristic size is the wavelength and not the drop diameter, we obtain the following estimate for the dimensionless critical wavelength:

$$\lambda_{cr} = 0.725 We^{-3/5} Re_\tau^{-2/5} |\epsilon_c|^{-2/5} \tag{2.2}$$

where the value of $\epsilon_c$, which is evaluated at the channel center, is extracted from literature data at the reference Reynolds number [124]. The critical wavenumber, $k_{cr} = 2\pi/\lambda_{cr}$ is indicated in Fig. 2.10 by a vertical dotted line. Assuming $\overline{w'}^2 \simeq u_\tau^2$, the critical wavelength (sketched in Fig. 2.1) corresponds to $We_{cr} \simeq 0.71$. According to equation Eq. 2.2, the local increase of the Reynolds number in the upper layer for $\mu_r = 0.25$ would lead to a slightly different critical wavelength. This difference is however negligible, since the critical wavelength is evaluated based on the balance between inertia and surface tension, therefore implying that a change in $We$ is much more effective than a change in $Re_\tau$. Note indeed that the influence of $Re_\tau$ on $\lambda_{cr}$ is not only explicit, via the term $Re_\tau^{-2/5}$, but also implicit, via $\epsilon_c$. Since $\epsilon_c$ decreases for increasing $Re_\tau$, the two terms – $Re_\tau^{-2/5}$ and $|\epsilon_c|^{-2/5}$ – balance each other. The estimated critical wavelength lies between the characteristic large scale and the dissipation scale. Indeed, the tendency to depart from the theoretical prediction, $k^{-4}$, and to follow the scaling $k^{-6}$, starts around $k_{cr}$. Further investigations at different values of the flow parameters would be required to fully confirm present predictions. We finally observe that at low wavenumbers, and consistently with what was observed for the frequency spectra, the numerical results show also a nice agreement with the prediction $S_\eta(k) \sim k^{-1}$ [128]. To the best of our knowledge, the coexistence of these two different scalings – one for the small scales and one for the large scales – and the characterization of the transition region from one scaling to the other, was never reported before in a single experiment/simulation.

### 2.1.7 Frequency-wavenumber spectra

Combining the temporal and the spatial analysis of the wave field discussed above, we can obtain the frequency-wavenumber spectra, $S_\eta\,(f, k_x)$, shown in Fig. 3.11, a quantity that allows us to characterize the wave propagation process (dispersion relation of waves). According to the classical wave theory [137], capillary wave propagation occurs at velocities that do depend on the wavelength of each individual wave and on the magnitude of surface tension. In addition, the liquid-liquid interface in our experiments is also advected by the mean bulk velocity at the centre of the channel and therefore the wave frequencies are doppler shifted. To isolate the wave velocity, a shift $\eta'(x,t) = \eta(x + dx_{shift}, t)$ is applied to the interface signal in the physical space, where $dx_{shift} = \overline{u}_c/df_{samp}$ and $df_{samp}$ is the frequency at which the interface elevation is sampled. By removing the doppler shift, the interface motion is characterized

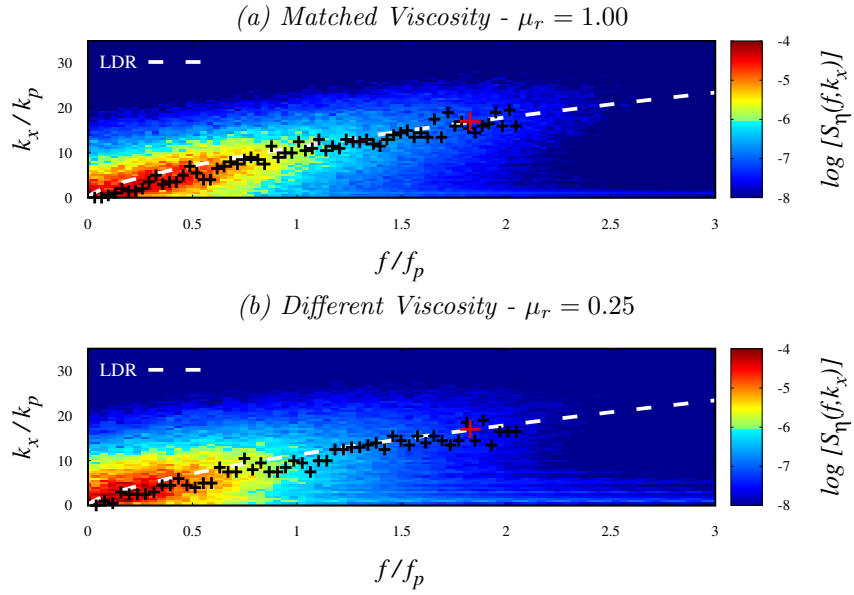


FIGURE 2.11 – Frequency-wavenumber spectra of wave elevation, $S_\eta\,(f, k_x)$, for $\mu_r = 1.00$ (panel a) and for $\mu_r = 0.25$ (panel b). Dashed white line in both panels corresponds to the linear dispersion relation (LDR) for capillary waves given by equation Eq. 2.4. The black crosses correspond to the maxima of the numerical results, while the red cross indicates the critical scale, $(f_{cr}, k_{cr})$, beyond which surface tension dominates over inertia.

only by the wave velocities, $c(k) = \omega(k)/k$, where $\omega = 2\pi f$ is the angular frequency. The theoretical dispersion relation for pure capillary waves in a finite-depth domain, including also the nonlinear correction [138], yields:

$$\omega^2\,(k) = \frac{\sigma}{\rho_1 + \rho_2} k^3 \left[1 + \left(\frac{ak}{4}\right)^2\right]^{-1/4} \tanh(kh), \tag{2.3}$$

in which $\sigma_\eta$ can be used instead of the wave amplitude $a$ [12]. In the present case, finite-depth and nonlinear corrections are found to play a minor role, and the linear counterpart of the dispersion relation [137] is proven accurate.

$$\omega^2\,(k) = \frac{\sigma}{\rho_1 + \rho_2} k^3 \tag{2.4}$$

This is shown in Fig. 3.11, where the theoretical prediction given by equation Eq. 2.4 is plotted by a dashed line, and compared to the numerical results (contour-maps). Local maxima of the numerical results are rendered by black crosses. Present findings indicate that, regardless of the value of $\mu_r$, spectral energy is focused around the theoretical prediction, equation Eq. 2.4. In addition, the critical scale (red cross) is localized near the point where the spectral energy starts decreasing sharply, in agreement with the previous observations that the energy of waves drops significantly at wavenumbers larger than the critical one, $k_{cr}$.

### 2.1.8 Isotropy of the wave field

We here examine the isotropy of the wave based on the behaviour of the time-averaged two dimensional wavenumber spectra, $\langle S_\eta(k_x, k_y)\rangle$, shown in Fig. 2.12. In this picture, the $x$ axis represents the normalized wavenumbers in the streamwise direction, $k_x/k_p$, while the $y$ axis represents the normalized wavenumbers in the spanwise direction, $k_y/k_p$. The two dimensional spectra show that, for both $\mu_r = 1.00$ and $\mu_r = 0.25$, wave energy is concentrated in a circular-like region of radius $k = \sqrt{(k_x/k_p)^2 + (k_y/k_p)^2} < 20$, only slightly elongated along the $k_x$ axis. This indeed indicates that wave propagation does not have a clear preferential direction.

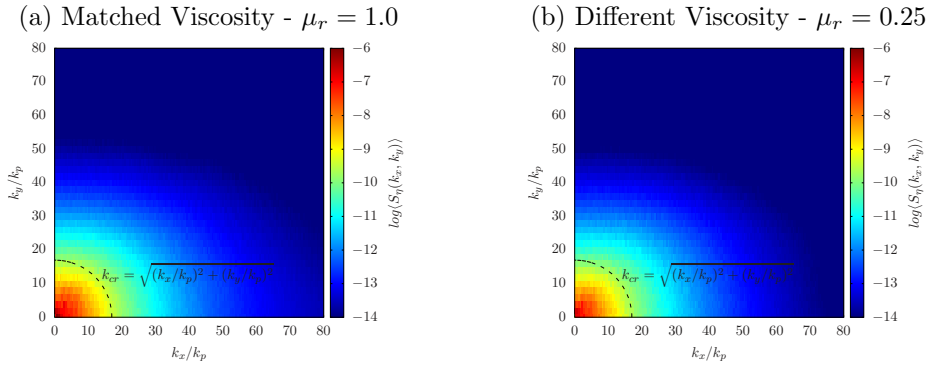


FIGURE 2.12 – Two dimensional wavenumber spectra of wave elevation, $\langle S_\eta(k_x, k_y)\rangle$, averaged in time, for $\mu_r = 1.00$ (panel a) and $\mu_r = 0.25$ (panel b). The black dashed line refers to circles of radius equal to the Hinze-Kolmogorov critical length scale, $k_{cr}$.

A discussion on the effects of the domain size, together with a discussion on the effects of shrinkage and coarsening of the phase-field, for the simulations performed in this work is included in Appendix B.

### 2.1.9 Time scales of the wave motion

In this section, we describe and quantify the time scales of wave motions, namely the time scale of linear wave oscillations, $\tau_l = 1/\omega$; the time scale of the nonlinear interactions among waves, $\tau_{nl}$; and the dissipative time scale of waves, $\tau_{diss} = \left[k^2(\nu_1 + \nu_2)\right]^{-1}$ [139]. Note that, beside being useful to characterize and parameterize the wave field, this analysis serves also the purpose to establish the possibility of applying the WTT – which is based on the assumption of the time scale separation, $\tau_l \ll \tau_{nl} \ll \tau_{diss}$ – to the present case. To estimate the nonlinear time scale, we follow the approach suggested in previous literature studies ([137, 140, 141, 24]), and based on the evaluation of the broadening of the frequency-wavenumber spectrum (Fig. 3.11) around the linear dispersion relation: $\tau_{nl} = 1/\Delta\omega(k^*)$, with $\Delta\omega(k^*)$ the spectrum width at the given wavenumber $k^*$. In particular, $\Delta\omega(k^*)$ is obtained based on the root mean square value of a Gaussian fit used to approximate the behaviour of $S_\eta(f, k^*)$ [24]. Repeating this calculation for all $k$, we obtain $\tau_{nl}(k)$. The behaviour of the different time scales is shown in Fig. 2.13. The assumption $\tau_l \ll \tau_{nl}$, between the linear (blue

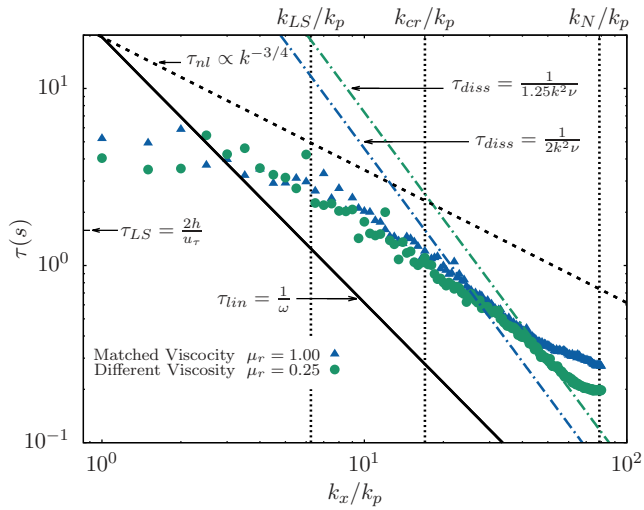


FIGURE 2.13 – Behaviour of the different time scales for waves motion as a function of the wavenumber. The nonlinear interaction timescale, $\tau_{nl}$, obtained from current simulations is shown by the symbols (triangles for $\mu_r = 1.00$ and circles for $\mu_r = 0.25$). The solid black line refers to the linear propagation time, $\tau_l$, while the dot-dashed lines refer to the dissipation time, $\tau_{diss}$ (evaluated as $\tau_{diss} = [k^2(\nu_1 + \nu_2)]^{-1}$, and particularized here for the two cases with $\mu_r = 1.00$ and $\mu_r = 0.25$). The theoretical prediction for the nonlinear interaction timescale, $\tau_{nl} \sim k^{-3/4}$, is shown by the black dashed line. The time scale corresponding to large-scale forcing, $\tau_{LS} = 2h/u_\tau$, is also indicated on the y-axis of the figure. The vertical dotted lines, from left to right, indicate the wavenumber associated with i) the large scale forcing, $k_{LS}$, ii) the critical Kolmogorov-Hinze scale, $k_{cr}$, and iii) the numerical cut-off, $k_N$.

solid line) and the nonlinear (circle symbols) time scales, is valid for moderate values of k. The two time scales are of the same order of magnitude only for large scale motions ($k/k_p < 3$). In the inertial range, $\tau_{nl}$ follows the scaling $\tau_{nl} \sim k^{-3/4}$ (dashed line), as predicted by WTT for capillary waves. Regarding the dissipative time scale (dot-dashed lines), we observe that it is in general larger than $\tau_{nl}$, but it becomes comparable around $k/k_p > 20$ (i.e. about the Hinze-Kolmogorov scale). This is a further indication that in the present case the theoretical power law scaling predicted by WTT cannot be observed over a broad range of wavenumbers.

### 2.1.10 Energetics of turbulence

In this section, the mean and turbulent kinetic energy budgets in the two-layer oil-water flow configuration are analysed. The so-called energy-box analysis [142, 143] is applied to obtain a decomposition of the different energy contributions in each of the two fluid layers. This technique, which was originally developed for the study of the global energy balance in a single-phase turbulent flow, is based on the space- and time- averaging of the energy budget terms over the entire computational domain. Consequently, the analysis does not account for energy fluxes through deformable interfaces between different fluids and thus it is not a-priori suited for the description of multiphase flow systems. However, in the case of multiphase flow systems, an extension of the original approach that is able to account for the energy budget of

each individual fluid phase through phase-averaging can be applied [66, 144]. Within this approach interfacial energy fluxes can also be accounted for. This approach has also been adopted by Roccon et al. [116] for the study of the energy balance in a lubricated two-layer channel flow configuration. The same approach will be used here, since it provides a simple and meaningful visual characterization of the energy fluxes in the fluid system.

**Energy budget for single-phase flow**

The first step towards the computation of the energy-box is to compute the energy budget of the flow. For this purpose, it is necessary to first perform a standard Reynolds decomposition of the flow field [145]. For a genericl field, $f(x,y,z,t)$, the Reynolds decomposition is expressed, as follows:

$$f(x,y,z,t) = \langle f(z,t)\rangle + f'(x,y,z,t) \tag{2.5}$$

Angular brackets, $\langle\cdot\rangle$, indicate averaging in space, across the two homogeneous directions of the channel, $x$ and $y$. $\langle f(z,t)\rangle$ is the mean and $f'(x,y,z,t)$ is the fluctuating part of the field $f(x,y,z,t)$. Note that time- and space-averaging of the hydrodynamic fields, is possible thanks to the ergodic theorem, according to which, under conditions of homogeneity and/or stationarity, probability averages can be replaced by time and/or space averages [146]. In this way, a mean (MKE) and a turbulent kinetic energy (TKE) contribution to the total kinetic energy are defined, as follows:

$$\text{MKE} = \frac{1}{2}\langle u_i\rangle\langle u_i\rangle \tag{2.6}$$

$$\text{TKE} = \frac{1}{2}u_i'u_i' \tag{2.7}$$

with repeated indices implying summations over the three directions $i=1$ $(x)$, $i=2$ $(y)$ and $i=3$ $(z)$. A transport equation for the MKE can be obtained via multiplying the Navier-Stokes equations by the mean velocity field and averaging in space and in time [147].

$$\begin{aligned}\frac{\mathrm{D[MKE]}}{\mathrm{Dt}} = &\underbrace{-[\langle u_i\rangle\langle\frac{\partial p}{\partial x}\rangle]}_{\Pi_m} + \underbrace{\left[\langle u_i'u_j'\rangle\frac{\partial\langle u_i\rangle}{\partial x_j}\right]}_{P_k} - \underbrace{\left[\frac{\partial(\langle u_i'u_j'\rangle\langle u_i\rangle)}{\partial x_j}\right]}_{T_m} \\ &+ \underbrace{\left[\frac{1}{2Re_\tau}\frac{\partial^2\langle u_i\rangle^2}{\partial x_j^2}\right]}_{D_m} \underbrace{-\left[\frac{1}{Re_\tau}\frac{\partial\langle u_i\rangle}{\partial x_j}\frac{\partial\langle u_i\rangle}{\partial x_j}\right]}_{\epsilon_m}\end{aligned} \tag{2.8}$$

Each term in the above equation accounts for a different contribution to the energy balance and can act either as a source, a sink or an internal transport term. The internal transport terms have no net contribution to the MKE budget and act purely as energy redistribution terms. In particular, the left hand side represents the material rate of change of MKE, which is equal to zero when the flow is at steady state.

The only source term in the equation is $\Pi_m$, which represents the power injected in the system via the mean pressure gradient. The sink terms include $P_k$ and $\epsilon_m$, which represent the production of TKE (at the expense of MKE) and the viscous dissipation by the mean flow, respectively. The other two terms, namely $T_m$ and $D_m$ are redistribution terms, which represent the work done by the Reynolds stresses, $\langle u_i' u_j' \rangle$ and the viscous diffusion of MKE, respectively. The transport equation for the TKE can be obtained via multiplying the Navier-Stokes equations by the fluctuating velocity field and averaging in space and time, as follows:

$$\begin{aligned} \frac{\mathrm{D[TKE]}}{\mathrm{Dt}} = & \underbrace{-\left[\frac{\partial \langle p' u_i' \rangle}{\partial x_i}\right]}_{\Pi_k} \underbrace{-\left[\langle u_i' u_j' \rangle \frac{\partial \langle u_i \rangle}{\partial x_j}\right]}_{P_k} \underbrace{-\left[\frac{1}{2}\frac{\partial \langle u_i' u_i' u_j' \rangle}{\partial x_j}\right]}_{T_k} \\ & \underbrace{+\left[\frac{1}{2Re_\tau}\frac{\partial^2 \langle u_i' u_i' \rangle}{\partial x_j^2}\right]}_{D_k} \underbrace{-\left[\frac{1}{Re_\tau}\frac{\partial u_i'}{\partial x_j}\frac{\partial u_i'}{\partial x_j}\right]}_{\epsilon_k} \end{aligned} \tag{2.9}$$

Similarly, the left hand side represents the material rate of change of TKE, which at steady state is zero. The only source term in the equation is $P_k$, which is the TKE production term and is the same as the one in the MKE balance, only here it acts as a source rather than a sink term. The only sink term is $\epsilon_k$, which represents the turbulent viscous dissipation. All the rest of the terms, namely $\Pi_k$, $T_k$ and $D_k$ are redistribution terms, which represent pressure diffusion, turbulent diffusion and viscous diffusion, respectively.

Thanks to the averaging across the $x$ and $y$ directions and in time, the dependence of each term in Eq. 2.8 and 2.9 is a function of only the channel wall-normal direction, $z$. Therefore, integrating each equation over the $z$ direction we obtain the following integral balance equations:

$$\overline{P_k} + \overline{\Pi_m} + \overline{\epsilon_m} = 0 \tag{2.10}$$

$$-\overline{P_k} + \overline{\epsilon_k} = 0 \tag{2.11}$$

Note that only the source and sink terms "survive" the integration, since the net contribution of every redistribution term, over the whole domain, is zero. Adding equations Eq. 2.10 and 2.11 by parts, we obtain the overall balance for the total kinetic energy, which states that the entire power injected into the system via the work of the pressure forces is ultimately dissipated by viscosity.

$$\overline{\Pi_m} + \overline{\epsilon_m} + \overline{\epsilon_k} = 0 \tag{2.12}$$

### Extension for two-phase flow

The same mathematical procedure to obtain transport equations for the MKE and TKE can be formally applied in the case of a multiphase flow. In this case, analogous energy balance equations are obtained, as follows:

$$\frac{\mathrm{D[MKE]}}{\mathrm{Dt}} = P_k + \Pi_m - T_m + D_m + \epsilon_m + \psi_m \tag{2.13}$$

$$\frac{\mathrm{D[TKE]}}{\mathrm{Dt}} = -P_k + \Pi_k + T_k + D_k + \epsilon_k + \psi_k \tag{2.14}$$

Notice that the presence of an interface inside the flow, results in the appearance of two additional terms, $\psi_m$ and $\psi_k$. The first of the two terms, $\psi_m$ represents the work of the surface tension forces on the mean flow, while the second, $\psi_k$ the work exchanged between the interface and the fluctuating velocity field via the surface tension forces [148]. These terms originate from the product between the surface tension force term in the Navier-Stokes equations and the mean and fluctuating velocity fields, respectively.

$$\psi_m = \langle u_i \rangle \frac{3Ch}{\sqrt{8}We} \frac{\partial \langle \tau_{ij}^c \rangle}{\partial x_j} \tag{2.15}$$

$$\psi_k = u_i' \frac{3Ch}{\sqrt{8}We} \frac{\partial {\tau_{ij}^c}'}{\partial x_j} \tag{2.16}$$

Integrating along the wall-normal direction, $z$, integral balance equations are obtained as for the single-phase case.

$$\overline{P_k} + \overline{\Pi_m} + \overline{\epsilon_m} + \overline{\psi_m} = 0 \tag{2.17}$$

$$-\overline{P_k} + \overline{\epsilon_k} + \overline{\psi_k} = 0 \tag{2.18}$$

In statistical steady state conditions, the average value of the interface area remains constant, which means that the total work done by surface tension forces is zero [149].

$$\overline{\psi_m} + \overline{\psi_k} = 0 \tag{2.19}$$

Therefore, the resulting balance for the total kinetic energy is the same as the one for the single-phase flow.

$$\overline{\Pi_m} + \overline{\epsilon_m} + \overline{\epsilon_k} = 0 \tag{2.20}$$

### Phase-averaged energy-box for tow-phase flow

The above procedure for obtaining balances for the two-phase flow may be mathematically correct, but, unlike in the single-phase flow scenario, it lacks a rigorous physical meaning in the multiphase flow setting. The reason is that the space-averaging procedure does not account for the presence of the interface and therefore no distinction is drawn between the energy contributions from each individual fluid phase. This is

indeed problematic and can even lead to erroneous results, in particular when the two fluids have different thermophysical properties such as viscosity and density. The best alternative to this approach is to take into account the multiphase nature of the system via a phase discrimination procedure [66, 144]. This so-called phase-averaging technique is presented in this section.
In order to derive the phase-averaged energy balance equations, the phase-field variable, $\phi$ is used to define a local concentration, $c_l$ for each liquid.

$$c_1 = \frac{1+\phi}{2}, \qquad c_2 = \frac{1-\phi}{2} \tag{2.21}$$

where, in accordance with the notation used so far, the subscript $l = 1$ is used to identify the water phase and the subscript $l = 2$ the oil phase. Multiplying the MKE and TKE balances, Eq. 2.13 and 2.14 by the two local concentrations and averaging along the $x$, $y$ directions and in time we obtain energy balance equations for each individual fluid layer.

$$\frac{\mathrm{D}[\mathrm{MKE}]_l}{\mathrm{Dt}} = P_{k,l} + \Pi_{m,l} - T_{m,l} + D_{m,l} + \epsilon_{m,l} + \psi_{m,l} \tag{2.22}$$

$$\frac{\mathrm{D}[\mathrm{TKE}]_l}{\mathrm{Dt}} = -P_{k,l} + \Pi_{k,l} + T_{k,l} + D_{k,l} + \epsilon_{k,l} + \psi_{k,l} \tag{2.23}$$

where the index $l$ is used to denote phase-averaged quantities obtained via taking the product of instantaneous quantities with the local concentration, $c_l$ and averaging in space. The physical meaning of each term remains the same as in the single-phase flow scenario, but each contribution now refers to a specific fluid layer. This means that upon integrating along the $z$ direction, the integral balance equations for each layer must also contain the contributions of the turbulent and viscous redistribution terms, $T$ and $D$, since these contributions are now only evaluated in a portion of the domain.

$$\overline{P_{k,l}} + \overline{\Pi_{m,l}} + \overline{T_{m,l}} + \overline{D_{m,l}} + \overline{\epsilon_{m,l}} + \overline{\psi_{m,l}} = 0 \tag{2.24}$$

$$-\overline{P_{k,l}} + \overline{\Pi_{k,l}} + \overline{T_{k,l}} + \overline{D_{k,l}} + \overline{\epsilon_{k,l}} + \overline{\psi_{k,l}} = 0 \tag{2.25}$$

Summing the respective balances, the redistribution terms cancel out and we obtain the global MKE/TKE integral energy balances for the two-fluid system.

$$\underbrace{\overline{P_{k,1}} + \overline{P_{k,2}}}_{\overline{P_k}} + \underbrace{\overline{\Pi_{m,1}} + \overline{\Pi_{m,2}}}_{\overline{\Pi_m}} + \underbrace{\overline{\epsilon_{m,1}} + \overline{\epsilon_{m,2}}}_{\overline{\epsilon_m}} + \underbrace{\overline{\psi_{m,1}} + \overline{\psi_{m,2}}}_{\overline{\psi_m}} = 0 \tag{2.26}$$

$$\underbrace{-\overline{P_{k,1}} - \overline{P_{k,2}}}_{\overline{-P_k}} + \underbrace{\overline{\epsilon_{k,1}} + \overline{\epsilon_{k,2}}}_{\overline{\epsilon_k}} + \underbrace{\overline{\psi_{k,1}} + \overline{\psi_{k,2}}}_{\overline{\psi_k}} = 0 \tag{2.27}$$

from where it becomes clear that adding the two last equations by parts again results to the total energy balance given by Eq. 2.20.

**Energy-box analysis of oil-water flow**

In Fig. 2.14 the energy-box representation of the phase-averaged energy contributions in the two fluid phases for both MKE and TKE is presented. The results correspond to averages obtained with the flow fields at steady state. Fig. 2.14a corresponds to the matched viscosity case, $\mu_r = 1.00$ and Fig. 2.14b to the unmatched viscosity case, $\mu_r = 0.25$. The dashed box on the left represents the MKE, while the one on the right the TKE contributions. Within each dashed box there is a box for each of the two layers, water at the top and oil at the bottom. Arrows indicate the various energy exchanges between the two layers. Green arrows represent the injected power, due to the action of the mean pressure gradient. Red arrows represent the energy dissipation by the mean and the fluctuating flow. The ciel arrows represent the TKE production. The dark blue vertical arrows represent the energy redistribution between the two layers. The redistribution terms of MKE are viscous diffusion and turbulent diffusion and have been collected to a single term, $\overline{F_{m,l}}$, for each phase. The redistribution terms of TKE are viscous diffusion, turbulent diffusion and pressure diffusion and have been collected in the term, $\overline{F_{k,l}}$, for each phase. Finally, the additional dashed box in the middle represents the energy of the interface. The orange arrows represent the energy flux from the mean flow field to the fluctuating flow field via the interface. All contributions are normalized based on the value of the injected power, $\overline{\Pi_m}$, in such a way so that $\overline{\Pi_m} = 100\%$.

In the matched viscosity case, the energy is distributed equally among the two layers, while the mean work done by the redistribution terms is equal to zero. Indeed, this is expected since the two fluid have the same thermophysical properties and occupy domains with the same volume, while the capillary waves at the interface are symmetric around the mean interface level. The interfacial term is a very small amount of the total energy injected into the system, $\overline{\psi_m} = 1.38\%$ and acts as a redistribution term extracting energy from the mean flow and transferring it to the fluctuating flow [116]. The total energy balance expressed by Eq. 2.20 is respected within an error of the order of 1%. In the unmatched viscosity case, more of the injected energy flows to the top layer than to the bottom layer. This is due to the significantly higher mean velocity in the less viscous fluid as shown in Fig. 2.2a. The TKE production is also higher in the top than it is in the bottom layer. Moreover, the energy dissipated by the mean flow is higher in the bottom than in the top layer, while the opposite holds for the energy dissipated by turbulence. Indeed, the high viscosity in the bottom layer leads to higher energy losses, while thanks to the increase in turbulence activity the low viscosity layer loses more energy by the fluctuating flow field. The energy redistribution terms are responsible for small energy fluxes between the layers, while their net contribution is very close to zero. Finally, the interfacial term, $\overline{\psi_m} = 1.63\%$ is of similar magnitude as in the matched viscosity case.

### 2.1.11 Energetics of waves

In this section, we examine the energy content of the capillary wave field at the interface between the two layers. In particular, we look at the potential and kinetic energy of

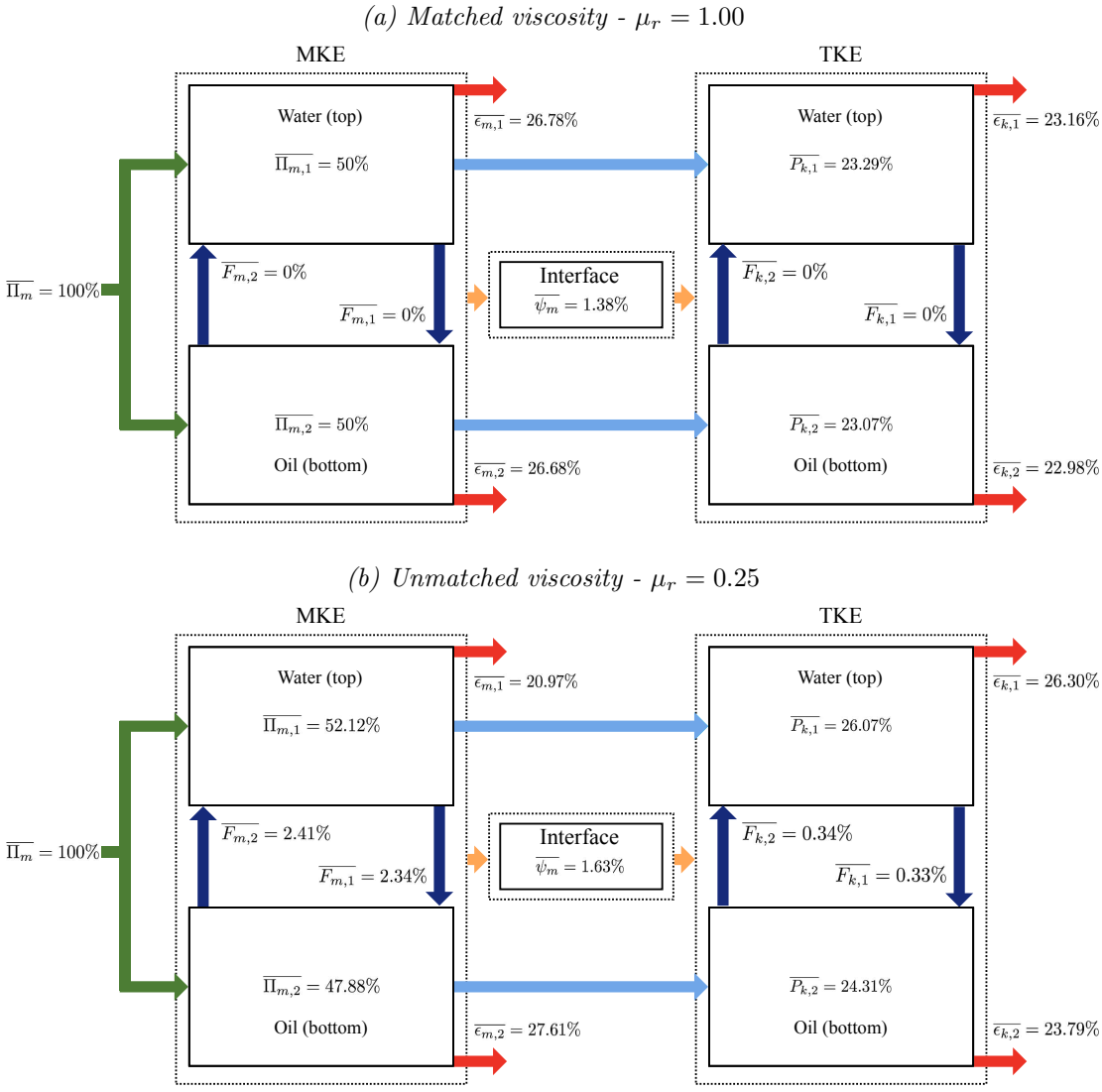


FIGURE 2.14 – Phase-averaged energy-box for the matched viscosity case, $\mu_r = 1.00$ (a) and the unmatched viscosity case, $\mu_r = 0.25$ (b). The two dashed boxes contain the power contributions to the MKE (left) and the TKE (right). Within each dashed box a rectangle represents each of the two fluid layers, top layer (water) and bottom layer (oil). All contributions are expressed as a percentage of the total power input, $\overline{\Pi_m}$, entering the system and here represented by green arrows. The mean and fluctuating viscous dissipation, $\overline{\epsilon_m}$ and $\overline{\epsilon_k}$, respectively, are represented by red arrows. The TKE production terms, $\overline{P_k}$, are represented by ciel arrows. Finally, the interfacial contribution, $\overline{\psi_m}$, is represented by orange arrows. The dark blue arrows linking the two layers represent the energy fluxes between the two layers, due to viscous, $\overline{D_m}$,$\overline{D_k}$, turbulent $\overline{T_m}$,$\overline{T_k}$ and pressure, $\overline{\Pi_k}$, diffusion, gathered in a single net redistribution term, $\overline{F_m}$,$\overline{F_k}$.

the capillary waves. We then look at a way of obtaining the total energy, by means of associating the total energy of the wave field to the power spectra of wave elevation via the energy spectrum. For a known theoretically predicted dissipation rate at different wave scales we can then estimate the dissipated power spectra and deduce the total dissipated power by the wave field via an integration over all wave scales. Finally, a method for obtaining the mean energy flux across wave scales based on the balance of wave energy expressed in the wavenumber space is proposed.

### Power spectra of wave elevation

Before proceeding to the analysis of the wave energy, it is here considered useful to include the definition of the power spectrum of wave elevation, $S_\eta$. The power spectrum of wave elevation (also called averaged periodogram in oceanographic contexts [151]) is computed either in space or in time from the DFT (Discrete Fourier Transform) of the discretized wave elevation signal, $\eta(x,t)$, assuming a number of $N$ discrete points, as follows:

$$S_\eta^n = \frac{1}{N^2}[|\eta_n^c|^2 + |\eta_{N-n}^c|^2] \ , \quad n = 1, 2, ..., N/2 - 1 \tag{2.28}$$

$$S_\eta^0 = \frac{1}{N^2}|\eta_0^c|^2 \tag{2.29}$$

$$S_\eta^{N/2} = \frac{1}{N^2}|\eta_{N/2}^c|^2 \tag{2.30}$$

where $|\eta_n^c|$ is the modulus of the DFT amplitudes. The sum of all the components of the spectrum is equal to the variance of the wave elevation signal.

$$\sum_{n=0}^{N/2} S_\eta^n = \frac{1}{N}\sum_{j=0}^{N-1} |\eta_j|^2 \tag{2.31}$$

The range (bandwidth) of the spectrum in terms of wave frequencies (or wavenumbers) is limited by the Nyquist sampling theorem [152], which determines the maximum frequency (or wavenumber) to half the sampling frequency, $f_{max} = \frac{1}{2dt}$ ($k_{max} = \frac{\pi}{dx}$) and the overall length of the signal, $T$ ($L_x$), which determines the lowest frequency, $f_{min} = \frac{1}{T}$ ($k_{min} = \frac{2\pi}{L_x}$).

$$\frac{1}{T} < f < \frac{1}{2dt} \quad \text{or} \quad \frac{2\pi}{L_x} < k < \frac{\pi}{dx} \tag{2.32}$$

### Capillary wave energy and wave energy spectrum

In the following, the wave energy is defined and related to the power spectra of wave elevation. The potential wave energy per unit surface area, $V$ for capillary waves between two fluids with densities, $\rho_1$ and $\rho_2$ [137], is given by:

$$V = \frac{1}{4}\sigma k^2 \eta^2 \tag{2.33}$$

while the kinetic wave energy per unit surface area, $T$ for capillary waves is given by:

$$T = \frac{1}{4}\left(\rho_1 + \rho_2\right) k^{-1} \dot{\eta}^2 \tag{2.34}$$

According to the linear wave theory [153], the speed of the wave oscillation, $\dot{\eta}$ is related to the angular wave frequency, $\omega$ via the formula, $\dot{\eta} = \omega\eta$. Substituting from the linear dispersion relation, Eq. 2.4, an equality is obtained between the two types of wave energy.

$$T = V = \frac{1}{4}\sigma k^2 \eta^2 \tag{2.35}$$

The total wave energy, $E$ is the sum of the potential and the kinetic wave energy. Therefore, the total wave energy per unit surface area and density for capillary waves is given by:

$$E = \frac{1}{2}\frac{\sigma}{\rho}k^2\eta^2 \tag{2.36}$$

where, in this case $\rho = \rho_1 = \rho_2$.

The wave energy spectrum, $E_k(k)$, can be associated to the power spectrum of wave elevation, $S_\eta(k)$ [150, 154], as follows:

$$E_k(k) = \frac{1}{2}\frac{\sigma}{\rho}k^2 S_\eta(k) \tag{2.37}$$

The total wave energy can then be obtained via the integration of the wave energy spectrum over the entire bandwidth of the wave signal:

$$E = \int_{k_{min}}^{k_{max}} E_k(k)dk = \int_{k_{min}}^{k_{max}} \frac{1}{2}\frac{\sigma}{\rho}k^2 S_\eta(k)dk \tag{2.38}$$

**Dissipation power spectrum**

Dissipation of wave energy can occur in several ways. The first way is through friction with a solid boundary. In our case, as discussed above, the waves are not influenced by the two walls at $z = \pm 1$ and their propagation is that of waves over infinite depth. Therefore, considering also that the domain is unbounded along the $x$ and $y$ directions, no dissipation of wave energy due to friction with solid boundaries occurs. The only other possible source of dissipation of wave energy is dissipation taking place at the surface. In this case, the classical wave theory [137] predicts a scaling of the dissipation rate with the wave scale.

$$\Gamma(k) = 2\nu k^2 \tag{2.39}$$

Note that this scaling applies only for the case of uncontaminated surface and is often in contrast to what is found in experiments, where the presence of surfactants leads to a surface that acts as an inextensible film with zero tangential velocity [155, 150]. The wave amplitude for linear waves then decays exponentially as:

$$\eta(t) = \eta_0 e^{-\Gamma t} \tag{2.40}$$

Eq. 2.39 shows that the dissipation rate is proportional to the square of the wavenumber, which indicates that shorter waves decay much faster than longer waves. The wave dissipation spectrum, $D_\eta(k)$ can then be defined as:

$$D_\eta(k) = E_k(k)\Gamma(k) \tag{2.41}$$

The dissipation spectra for the two cases of matched and unmatched viscosity are shown in Fig. 2.15. For both cases, the dissipated power density increases as the wavenumber increases in the low wavenumber range, plateaus in the intermediate wavenumber range and then drops in the high wavenumber range. Note that based on the above the scaling followed should be $D_\eta(k) \sim k^4 S_\eta(k)$. Indeed, Fig. 2.15 shows that the slopes $k^3$, $k^0$ and $k^{-2}$ are observed in the corresponding ranges of the $k^{-1}$, $k^{-4}$ and $k^{-6}$ of the wavenumber spectra.

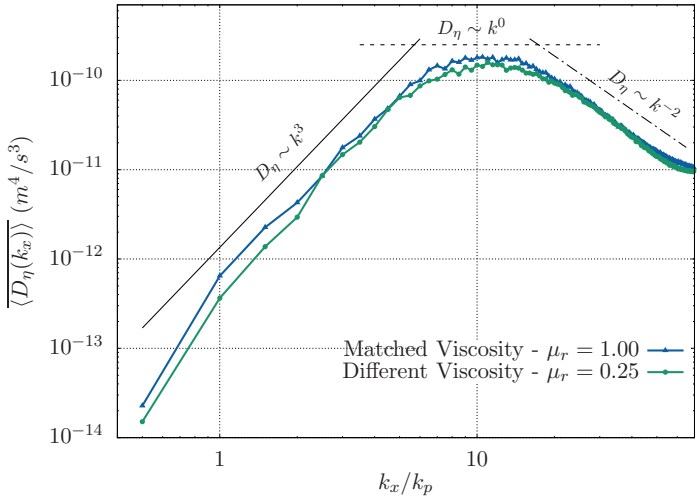


FIGURE 2.15 – Dissipation spectra, $\overline{\langle D_\eta\,(k_x)\rangle}$, averaged in space (over the spanwise direction) and in time. Results are shown for $\mu_r = 1.00$ (blue triangles) and $\mu_r = 0.25$ (green bullets).

The total power dissipated by the waves can also be estimated by integrating the dissipation spectra over the entire bandwidth:

$$D = \int_{k_{min}}^{k_{max}} D_\eta(k)dk = \int_{k_{min}}^{k_{max}} 2\nu k^2 E_k(k)dk \tag{2.42}$$

**Energy flux across wave scales**

Energy is injected into the waves due to forcing by the surrounding turbulent flow field. Therefore, a broad-band forcing due to fluctuations of the hydrodynamic field over multiple scales takes place. This is a scenario that is indeed much different to the one assumed by WTT, where dissipation and forcing scales are clearly separated and a constant energy flux occurs across the inertial range of the wave spectrum [117]. Similarly, in most experiments with capillary wave turbulence power is mechanically injected into the waves at a narrow-band frequency corresponding to the oscillation frequency of a wave maker [10, 12, 120]. It therefore becomes evident that since both

dissipation and forcing occur across multiple wave scales, the hypothesis of a constant energy flux across different scales is questionable, since energy can be injected or extracted from different parts of the wave spectrum in a non-uniform manner. The energy balance in the wavenumber space, can be expressed as:

$$\frac{\partial E_k}{\partial t} + \frac{\partial \epsilon(k)}{\partial k} = -D_\eta(k) + F_t(k) \tag{2.43}$$

where the additional term of the forcing power spectrum due to turbulence, $F_t(k)$ has been added to the right hand side of the original balance proposed by Nazarenko et al. [140]. The forcing term is associated to the energy provided to the waves by the turbulent flow field. The kinetic energy per unit volume and unit density of the vertical turbulent velocity fluctuations is given by:

$$E_t = \frac{1}{2}w^2 \tag{2.44}$$

Therefore, assuming that the energy provided to the waves is proportional to the available kinetic energy of the fluctuating flow field, the turbulent forcing power spectrum can be expressed as:

$$F_t(k) \sim \frac{1}{2}E_{ww}(k) \tag{2.45}$$

where $E_{ww}(k)$ is the power spectrum of the vertical velocity fluctuations in the vicinity of the interface.

Finally, since the time derivative of the energy spectrum at statistical steady state is equal to zero, the energy flux at a specific wavenumber $k^*$ can be obtained from the integration of the wave energy balance, as follows:

$$\epsilon(k^*) = \int_{k^*}^{k_{min}} \left[D_\eta(k) + F_t(k)\right] dk \tag{2.46}$$

## 2.2 Surface tension effects

So far, the effect of the viscosity on the turbulent flow and interface deformation properties has been examined. In particular, it was found that for moderate values of the viscosity ratio, $\mu_r \sim O(1)$ and for an interface that is equidistant from the two channel walls, the wave dynamics are not strongly affected by viscous effects. Overall, an unmatched viscosity between the two liquid layers leads to a reduction of the wave amplitude, presumably due to the development of strain at the interface, while wave spectra, both in time and in space, show that the wave interaction with the surrounding turbulent flow, as well as the wave-wave interaction at moderate and small wave scales are almost unaffected by the change of $\mu_r$. Indeed, it was observed that the wave dynamics at intermediate scales are mainly driven by the interaction between capillary and inertial forces. In particular, the balance between these forces at the critical length scale acts as a threshold between longer waves, which grow in amplitude and shorter ones that do not. In this part of the study, we aim at observing the effect of modifying this balance, by means of reducing surface tension through an increase of the Weber number.

### 2.2.1 Simulation setup

We focus on the effect of the Weber number. More specifically, we perform simulations at different Weber numbers, while keeping all other simulation parameters constant. In particular, two additional simulations have been performed at two Weber numbers that are higher compared to the reference one, $We = 1.0$, namely $We = 1.5$ and $We = 2.0$. The same reference Reynolds number $Re_\tau = 300$ and matched viscosity ratio $\mu_r = 1.00$ have been used for all simulations. The simulation parameters are summarized in Tab. 2.4. Note that $\Delta_x^+$, $\Delta_y^+$ and $\Delta_z^+$ are the streamwise, spanwise and wall-normal grid spacings respectively, expressed in wall units. The selected resolution is adequate for resolving the smallest turbulent flow scales and to guarantee an accurate depiction of the interfacial layer. Considering that the rest of the parameters are fixed for all simulations, the increase of the Weber number can be directly interpreted as a decrease of the surface tension between the liquids.

| Simulation | $Re_\tau$ | $\mu_r$ | $\Delta_x^+$ | $\Delta_y^+$ | $\Delta_z^+$ |
|---|---|---|---|---|---|
| $We = 1.0$ | 300 | 1.00 | 7.37 | 7.37 | 1.84 |
| $We = 1.5$ | 300 | 1.00 | 7.37 | 7.37 | 1.84 |
| $We = 2.0$ | 300 | 1.00 | 7.37 | 7.37 | 1.84 |

TABLE 2.4 – Overview of the main simulation parameters at variable Weber number.

### 2.2.2 Interface statistics

In the left column of Fig. 2.16 we can see snapshots of the instantaneous interface deformation over the $x-y$ plane, obtained at steady state, for the three different cases. It is clear that as the Weber number increases, the deformation is enhanced and is characterized by the presence of smaller scale structures. A quantitative description of this effect can be obtained by means of estimating the curvature of the wave field. The interface curvature is defined as $\kappa = \nabla \cdot \mathbf{n}$, where $\mathbf{n}$ is a vector normal to the interface. If the wave slope is small, $\nabla\eta << 1$ then the interface curvature can be approximated as $\kappa \approx \left(\frac{\partial^2\eta}{\partial x^2} + \frac{\partial^2\eta}{\partial y^2}\right)$. Maps of the absolute value of curvature, $|\kappa|$, corresponding to the elevation snapshots in the left column of Fig. 2.16 are shown in the right column of the same figure. Indeed, we observe that regions of high curvature become much more pronounced as the Weber number increases, indicating rapid changes in wave steepness.

The values of the root mean square of the interface elevation, $\sigma_\eta$ and the typical wave steepness, $\sigma_s$ for each case are summarized in Tab. 2.5. The percentage increase in $\sigma_\eta$ with respect to the $We = 1.0$ case is 8% and 15.4% for $We = 1.5$ and $We = 2.0$, respectively. The percentage increase in $\sigma_s$ with respect to the $We = 1.0$ case is 28.3% and 56.7%, respectively. This large increase in wave steepness and the relatively smaller increase in wave amplitude indicates that shorter waves grow in amplitude as the Weber number increases, which is also in agreement with the qualitative observation of the wave field reported in Fig. 2.16.

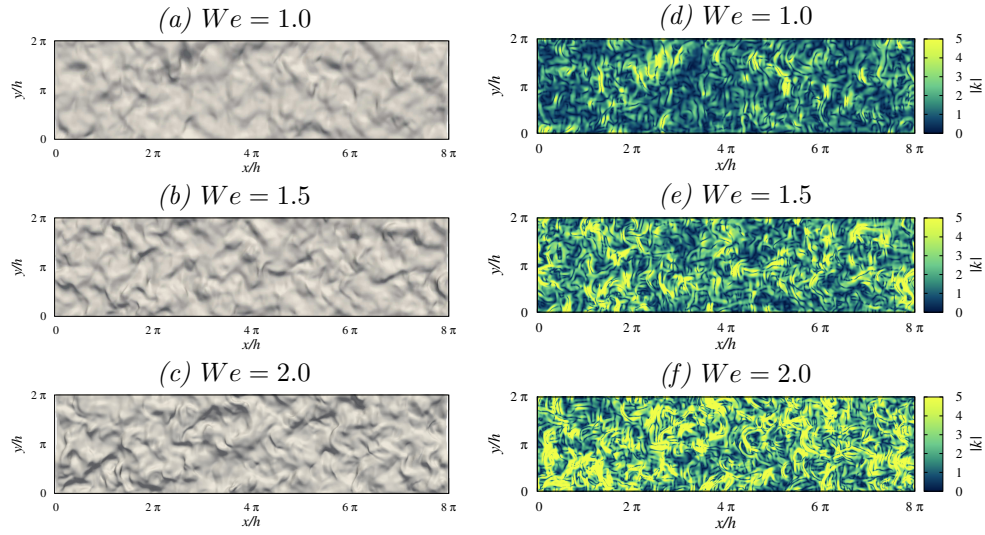


FIGURE 2.16 – Instantaneous interface elevation snapshots at $t^+ = 4000$ (left) and corresponding absolute curvature maps (right) for the three cases: We=1.0, We=1.5 and We=2.0.

| Simulation | $\sigma_\eta/h$ | $\sigma_s$ | $\frac{k_{cr}}{k_p}$ |
|---|---|---|---|
| $We = 1.0$ | 0.136 | 0.374 | 17.0 |
| $We = 1.5$ | 0.147 | 0.480 | 21.7 |
| $We = 2.0$ | 0.157 | 0.586 | 25.8 |

TABLE 2.5 – Overview of the wave field parameters for the variable Weber number simulations.

A uni-dimensional representation of the instantaneous interface elevation signals across the streamwise direction, $x$ at a fixed spanwise position, $y = L_y/2$, is shown in Fig. 2.17 (top left). In Fig. 2.17 (bottom left) the time evolution of the interface elevation at a fixed $x, y$ position is also shown. In both cases, we can observe a noticeable yet not too pronounced increase of the wave amplitude together with a significant increase of the wave slope, as the Weber increases. Finally, the probability density function of the interface elevation normalized by its standard deviation, $\sigma_\eta$, for all three cases is shown in Fig. 2.17 (right). The distribution is Gaussian in every case, indicating that the capillary waves are perfectly symmetric around the mean interface level, $z = 0$.
The critical wavelength, $\lambda_{cr}$ depends on the Weber number according to equation Eq. 2.2. Indeed, the critical wavelength should decrease as the Weber number increases, since surface tension forces become weaker compared to inertial forces, which retain their original magnitude. The values of the critical wavenumber, $k_{cr}$, for each case are summarized in Tab. 2.5. Wavenumber power spectra of wave elevation, $\overline{\langle S_\eta(k_x)\rangle}$, are shown Fig. 2.18 (left). The spectra seem to be unaffected at larger scales, beyond the turbulent forcing range, where the $k^{-1}$ scaling is always observed over the same range of wavenumbers. On the other hand, the spectra inside the turbulent forcing

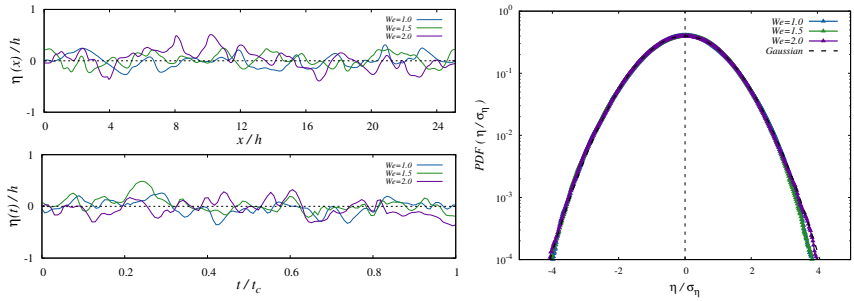


FIGURE 2.17 – Left (top): Interface elevation signal as a function of the streamwise direction, $x$ at a fixed instant in time. Left (bottom): Interface elevation signal as a function of time, $t$ at a fixed $x, y$ position in space. Right: Probability density function of the interface elevation normalized by the root mean square of the interface elevation for each case. The Gaussian distribution with zero mean and unit standard deviation is also shown with a black dashed line.

range vary with the increase of the Weber number. In order to better appreciate this change, the compensated power spectra $\overline{\langle k_x^4 S_\eta(k_x)\rangle}$ are also shown in Fig. 2.18 (right), where the $k^{-4}$ scaling appears as a horizontal line. Indeed, we observe that the horizontal range of the spectra is extended as the Weber number increases following the corresponding shift of the critical wavenumber to the right. This is in agreement with the observation that the transition of the spectral slope occurs at the threshold between longer waves that grow in amplitude, due to the predominance of inertial forces and shorter waves that do not grow in amplitude, due to the predominance of surface tension forces.

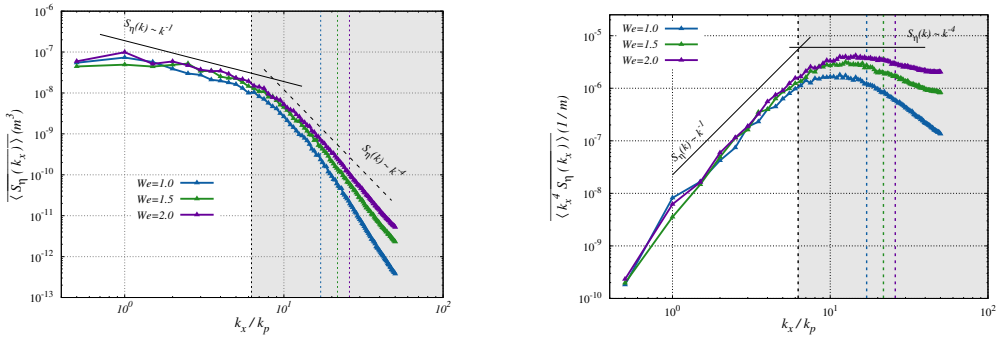


FIGURE 2.18 – Left: Streamwise wavenumber power spectra of wave elevation for the three cases. The coloured vertical dotted lines indicate the critical wavenumber, $k_{cr}$, for $We = 1.0$ (blue), $We = 1.5$ (green), $We = 2.0$ (purple). Right: the same spectra compensated by $k^4$.

Frequency-wavenumber spectra of wave elevation, $S_\eta(f, k_x)$, for the three cases are reported in Fig. 2.19. We observe that in every case the the maximum of the wave energy is localized around the LDR for capillary waves. However, the increase of the Weber number results in shorter, high-frequency waves becoming energetic.

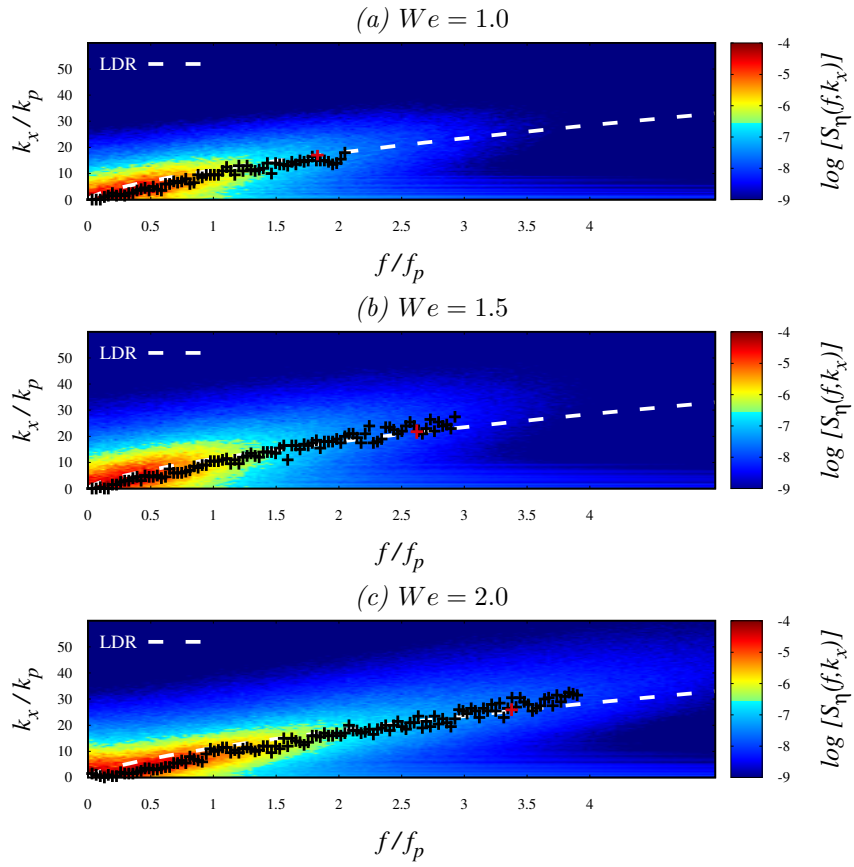


FIGURE 2.19 – Frequency-wavenumber spectra of wave elevation, $S_\eta(f, k_x)$, for the three cases. Dashed white line corresponds to the linear dispersion relation (LDR) for capillary waves. The black crosses correspond to the maxima of the numerical results, while the red crosses indicate the critical scale, $(f_{cr}, k_{cr})$, beyond which surface tension dominates over inertia.

## 2.3 Conclusions

We have reported computational results on the propagation of capillary waves travelling at the interface between two immiscible liquid layers that flow inside a plane channel. Simulations are based on a combined pseudo-spectral DNS-PFM method, which gives us the possibility to describe the action of surface tension forces, and therefore to track the dynamics of the two different liquid layers and of the separating interface. The two liquid layers are driven by an imposed mean pressure gradient and have the same thickness. Two parametric studies were performed, the first at a variable viscosity ratio between the two liquid layers, so to study the effects of viscosity and the second at a variable Weber number, so to study the effects of surface tension. The focus of this work was primarily on the full space and time-resolved spectrum of wave elevation and secondarily on the properties of the turbulent flow

field. The viscosity mismatch between the two liquids was found to have a small influence on the properties of the wave field for the examined range of viscosity ratio i.e. down to $\mu_r = 0.25$. Our results show that the frequency spectra exhibit only a short inertial regime characterized by the scaling $S_\eta(f) \sim f^{-8/3}$, as predicted by the Wave Turbulence Theory (WTT). The main reason for the short inertial regime is the adopted computational setup, which is characterized by realistic flow conditions that are different from the simplified assumptions set in the context of WTT (for example the absence of a clear scale separation between energy injection and dissipation, and the importance of wave nonlinearity, which is considered weak in the context of the theory). At lower frequencies, and confirming recent theoretical and experimental observations, we find a scaling $S_\eta(f) \sim f^{-1}$, compatible with the large-scale energy equipartition assumption. Even the streamwise wavenumber spectrum – for the same reasons already mentioned above – does exhibit only a short inertial regime with scaling $S_\eta(k) \sim k^{-4}$, as predicted by WTT. Interestingly, we find a much steeper scaling, $S_\eta(k) \sim k^{-6}$, at wavenumbers beyond a critical scale $k_{cr}$, which corresponds to the characteristic wave size at which surface tension and inertial forces balance. At low wavenumbers, the theoretical scaling $S_\eta(k) \sim k^{-1}$, consistent with the large-scale energy equipartition assumption, is recovered. Finally, joint frequency-wavenumber spectra have shown that the dispersion relation is in good agreement with the theoretical prediction, $\omega(k) \sim k^{3/2}$. The energy budget of the flow was also analysed based on the phase-averaged energy-box technique. The results showed that while the distribution of the mean and turbulent energies is symmetric in the matched viscosity case it becomes asymmetric in the unmatched viscosity case. In particular, the turbulent kinetic energy production increases in the top layer with the lowered viscosity and so does the energy dissipation by the fluctuating flow field. The opposite is true for the dissipation of energy by the mean field, which is higher at the bottom layer with the high viscosity compared to the top. In both cases, the energy flux towards the interface is small and amounts for approximately 2% of the energy injected into the system due to the mean pressure gradient. The energy injected from the flow field to the interface is passed to the waves. Capillary wave energy is of two types: potential and kinetic, the two being equal in the idealized linear wave case. The spectrum of the total wave energy can thus be estimated and associated to the power spectrum of wave elevation . The dissipation power spectra have also been computed, assuming the classical model for the wave amplitude dissipation rate. The results show a scaling according to $D_\eta(k) \sim k^4 S_\eta(k)$. Finally, a modified wave energy balance equation in the wavenumber space is proposed with the addition of an extra term to account for the presence of forcing across multiple wave scales. The forcing term is then associated to the turbulent spectra of the vertical velocity fluctuations near the interface mean position. In contrast to the viscosity, the change of surface tension via the modulation of the Weber number has a striking effect on the interface dynamics. The root mean square of the interface elevation, as well as the wave steepness and curvature, increase significantly with the increase of Weber number, which given that all the rest of the parameters of the problem remain fixed is equivalent to a decrease of surface tension. The Kolmogorov-Hinze scale, although not affected by the change of viscosity (Reynolds number), it is affected significantly with the change of Weber number, since it expresses the balance between surface tension and inertial forces. The increase of the

Weber number leads to a shift of the critical wavenumber, $k_{cr}$ towards smaller scales. The results suggest that the transition between a mild and a steep decrease of wave energy as the wavenumber increases takes place near the shifted critical wavenumber, $k_{cr}$ in each case.

# 3

# Channel flow of a thin laminar layer over a thick turbulent layer

**Reproduced in part from:**
Giamagas, G., Zonta, F., Roccon, A. & Soldati A. (2023) *Turbulence and Interface Waves in Stratified Oil–Water Channel Flow at Large Viscosity Ratio.* Flow Turbul. Combust.

Oil-water flows are observed in a number of energy applications and environmental phenomena, from the transport of oil and water over long distances in pipelines [156, 157, 158] to the prevention and mitigation of pollution in oil spill accidents [159, 160]. An important feature of oil-water flows is the small density difference between the two fluids. If, on one side, this density difference does not significantly alter the exchange of momentum and energy in oil-water interactions, on the other side, it promotes the occurrence of stratified configurations in which the oil – which is slightly lighter – flows on top of water. This aspect has a huge impact on the resulting flow and on its control and manipulation (to design efficient oil/water separators, or to devise strategies to mitigate pollution from oil-spill risks). Indeed, the presence of a thin layer of oil, characterized by a density similar to water, but by a much larger viscosity, can largely modify the pressure drop required to drive the flow inside pipelines in industrial applications [161], or can lead to strong modifications of the waves and turbulence dynamics at the water surface in environmental/marine applications [162, 5, 6, 163]. For all these reasons, the oil-water stratified flow has gathered the attention of many researchers. Several investigations have been performed employing different analytical, experimental, and numerical techniques [161, 24, 164, 115, 103, 165], as well as targeting different flow configurations, from pipe/channel flows to more environmental-oriented setups. Experimental techniques often represent an important tool to investigate the physics of turbulent flows, but also to validate analytical or simplified mathematical models. However, accurate experimental measurements, which usually rely on optical techniques, are difficult to realize in oil/water flows because of the fluid turbidity. It is therefore not surprising that, to obtain precise space- and time-resolved data on the entire flow field and also on the dynamics of the oil/water interface, direct numerical simulations are being used in this field more and more frequently in the last years [166, 27, 115, 90]. Also in this case, accurate and reliable numerical methodologies capable of describing the interface position and deformation in time are required

[167, 33, 31]. An additional difficulty arises when large oil-to-water viscosity ratios are considered, since the resulting flow structure might be characterized by laminar-turbulent patches and by a high degree of intermittency, depending on the local flow characteristics and on the interface-flow interactions.

In this chapter, we use Direct Numerical Simulation (DNS) of the Navier-Stokes equations coupled with a Phase-Field Method (PFM) to investigate the channel flow of a thin layer of oil flowing on top of a thick layer of water. In contrast with previous works [168, 30, 4, 116], where the focus was mainly on elucidating the Drag-Reduction (DR) mechanisms observed in lubricating channels (i.e. when a thin layer of small viscosity fluid is used to lubricate the flow of a large viscosity fluid), here we move to the opposite situation in which a thin layer of a much more viscous fluid (50 or 100 times more viscous) flows on top of a thick layer of water. This configuration aims at mimicking oil-water flows in pipelines, as well as free-surface flows in which a thin oil film, being very viscous, behaves as a boundary for the liquid flow beneath it. The main goal of this work is to characterize the flow field as well as the structure and properties of the capillary waves that are generated at the oil-water interface.

## 3.1 Simulation setup

The adopted setup consists of a flow configuration with two immiscible fluid layers driven by an imposed mean pressure gradient along the horizontal direction (see Fig. 3.1). Channel dimensions are $L_x \times L_y \times L_z = 4\pi h \times 2\pi h \times 2h$, with $h$ the half-channel height and $x$, $y$, $z$ the streamwise, spanwise and wall-normal directions, respectively. A thin oil layer, $0.15h$ thick, flows over a thick water layer, $1.85h$ thick. To mimic a realistic oil-water configuration, we consider that the two layers have the same density $\rho_o = \rho_w = \rho$, but different viscosity, $\mu_o$ and $\mu_w$. For the validity of the matched densities assumption we refer to the Appendix C. The deformable interface separating the two fluid layers is characterized by a constant and uniform value of the surface tension, $\sigma$.

We consider the benchmark case of a single-phase turbulent channel flow, and three different cases of oil-water two-phase flow, each characterized by a different value of the oil-to-water viscosity ratio $\mu_r = \mu_o/\mu_w$. In particular, we consider the following viscosity ratios: $\mu_r = 1$, $\mu_r = 50$ and $\mu_r = 100$. All simulations are run at the given reference value of the shear Reynolds number $Re_\tau = 300$ and Weber number $We = 0.5$. For all cases, the domain is discretized using $N_x \times N_y \times N_z = 512 \times 256 \times 513$ grid points. The Cahn number is set to $Ch = 0.02$, while the Péclet number is obtained according to the scaling $Pe = 3/Ch$ [58, 43]. An overview of the simulation parameters, together with the resulting grid spacing is reported in Tab. 3.1. The initial condition for all simulations is taken from a preliminary direct numerical simulation of a single-phase turbulent channel flow at $Re_\tau = 300$, complemented by a proper definition of the initial distribution of the order parameter $\phi$ so that the liquid-liquid interface is initially flat and located at distance $0.15h$ from the top wall.

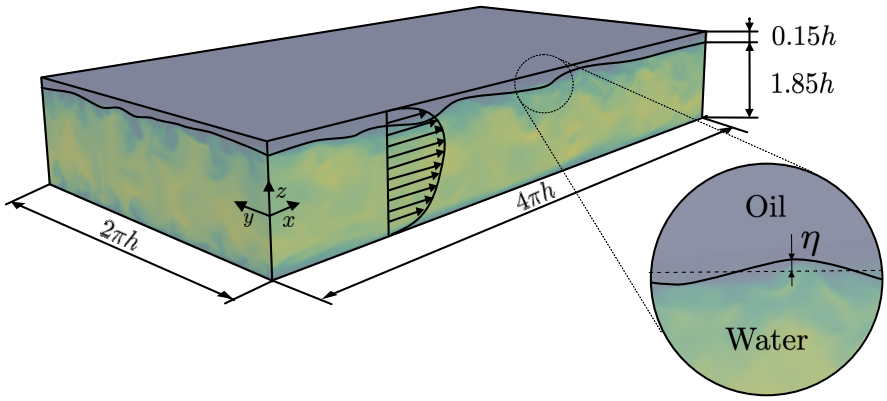


FIGURE 3.1 – Sketch of the computational domain employed for the simulations. The channel has dimensions $L_x \times L_y \times L_z = 4\pi h \times 2\pi h \times 2h$. The nominal thickness of the oil layer (located at the top) is $0.15h$ while the nominal thickness of the water layer (located at the bottom) is $1.85h$. The close-up view shows the definition of the interface elevation $\eta$, i.e. the vertical distance from the nominal position of the interface.

| Simulation | $Re_\tau$ | $\mu_r$ | $We$ | $N_x$ | $N_y$ | $N_z$ | $\Delta_x^+$ | $\Delta_y^+$ | $\Delta_z^+$ |
|---|---|---|---|---|---|---|---|---|---|
| SP | 300 | - | - | 512 | 256 | 513 | 7.37 | 7.37 | 1.84 |
| MP1 | 300 | 1 | 0.5 | 512 | 256 | 513 | 7.37 | 7.37 | 1.84 |
| MP2 | 300 | 50 | 0.5 | 512 | 256 | 513 | 7.37 | 7.37 | 1.84 |
| MP3 | 300 | 100 | 0.5 | 512 | 256 | 513 | 7.37 | 7.37 | 1.84 |

TABLE 3.1 – Overview of the main simulation parameters for the reference single-phase (SP) flow and for the oil-water flows characterized by different values of the viscosity ratio $\mu_r$. The resulting grid spacing in wall units is also reported.

## 3.2 Flow field characterization

In the following, we discuss the results obtained from the numerical simulations focusing on the flow field and investigating the turbulence behaviour from both a qualitative and quantitative viewpoint.

### 3.2.1 Qualitative description of the flow field

Fig. 3.2 shows the instantaneous distribution of turbulent kinetic energy, $TKE = \left(u'^2 + v'^2 + w'^2\right)/2$, on a $y-z$ plane located at $x = 0$, for the different cases considered in this study: single-phase (panel *a*), $\mu_r = 1$ (panel *b*), $\mu_r = 50$ (panel *c*) and $\mu_r = 100$ (panel *d*). The instantaneous position of the interface (identified as the iso-level $\phi = 0$) is also shown by a white line. We notice that – compared to the reference single-phase case – the presence of the interface, no matter the value of $\mu_r$, induces an asymmetry in the flow. In particular, by increasing $\mu_r$, turbulence is progressively damped inside the thin oil layer (located near the top wall). In addition, we note that by increasing

$\mu_r$ turbulence is damped also in the thick water layer, near the bottom wall. This behaviour can be explained by looking at the value of the local Reynolds number. At the bottom wall, considering that the friction velocity is $u_{\tau,bot} = \sqrt{\tau_{w,bot}/\rho}$, the semi-local Reynolds number becomes [95, 4]:

$$Re_{\tau,bot} = Re_\tau \sqrt{\frac{2 \mid \tau_{w,bot} \mid}{\mid \tau_{w,bot} \mid + \mid \tau_{w,top} \mid}}, \tag{3.1}$$

from which we obtain: $Re_{\tau,bot} = 364$ ($\mu_r = 1$), $Re_{\tau,bot} = 255$ ($\mu_r = 50$) and $Re_{\tau,bot} = 251$ ($\mu_r = 100$). As a consequence, turbulence becomes progressively attenuated near the bottom wall. It is also interesting to observe that the turbulent intensity just below the interface, in the water layer, is higher for $\mu_r = 50$ and $\mu_r = 100$ compared to the case with $\mu_r = 1$. This effect suggests that the interface behaves for the water layer similarly to a solid boundary, whereas it behaves like a compliant surface for $\mu_r = 1$.

### 3.2.2 Mean velocity profiles and flow rates

The change of the flow structure described above clearly results into a corresponding change of the mean velocity profiles. Fig. 3.3*a* shows the mean streamwise velocity profile, $\langle u \rangle$, as a function of the wall-normal coordinate, $z$, for all cases considered here. We observe that, compared to the single-phase case – for which the velocity profile is symmetric – the introduction of the thin oil layer breaks the symmetry of the velocity profile. While for $\mu_r = 1$ the velocity profile is skewed towards the upper part of the channel, for $\mu_r = 50$ and $\mu_r = 100$ it is skewed towards the bottom part. The main reason for this different behaviour is, as anticipated above, the different character of the liquid-liquid interface depending on the value of $\mu_r$: while for $\mu_r = 1$ the interface is compliant, and actively adapts to vertical momentum, for $\mu_r = 50$ and $\mu_r = 100$ the interface acts essentially as a wall, hence giving a velocity profile with a maximum located roughly halfway between the interface and the bottom wall (i.e. shifted towards the bottom wall compared to the channel centreline). Rescaling the velocity profile by the actual value of the friction velocity at the bottom wall, $u_{\tau,bot}$ (as done to compute the semi-local Reynolds number in equation 3.1), it is possible to evaluate the behaviour of the velocity field in wall units, and compare it with the law of the wall: $u = z^+$ and $u = (1/k)\log(z^+) + 5$ (where $k = 0.41$ is the von Kármán constant [169]). The single-phase turbulent flow (black) shows a good agreement with the law of the wall (represented by the dashed line). Even for the case $\mu_r = 1$ the results of the simulation follow fairly well the behaviour of the law of the wall. The situation is slightly different for $\mu_r = 50$ and $\mu_r = 100$, for which we notice a reduction of the flow velocity, in particular in the viscous sub-layer. This indicates that the introduction of the thin oil layer in the top part of the channel induces a general attenuation of turbulence, which reflects into a corresponding modulation of the turbulence regeneration cycle even at the bottom wall. The flow rate of the oil and the water layer, $Q_o$ and $Q_w$, as well as the total flow rate, $Q_t$, are shown – normalized by the single-phase flow rate, $Q_{SP}$ – in Tab. 3.2. As it can be observed, the introduction of a thin liquid layer with the same viscosity of the thick layer ($\mu_r = 1$) leads to a significant increase in the total flow rate, which amounts to about 27%

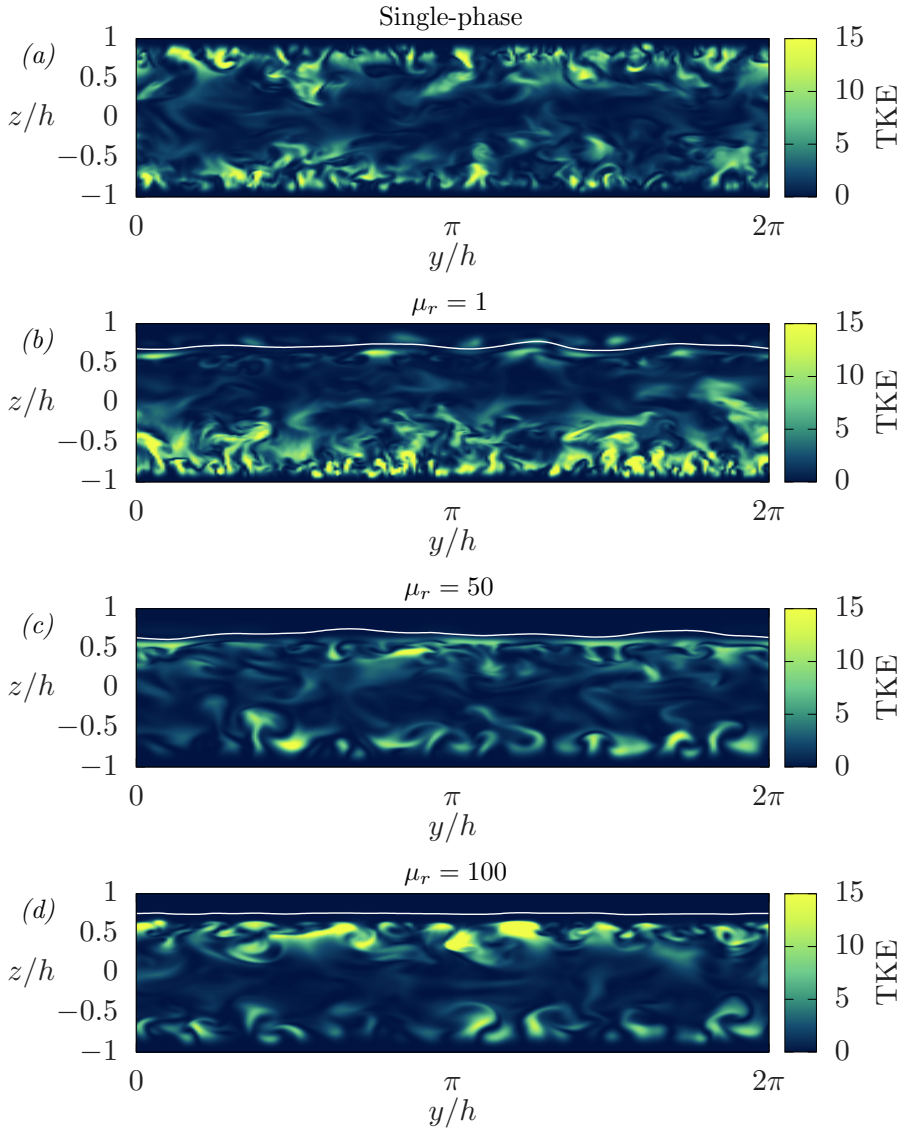


FIGURE 3.2 – Instantaneous distribution of turbulent kinetic energy, $TKE = \left(u'^2 + v'^2 + w'^2\right)/2$ on an $y - z$ plane located at $x = 0$ for the different cases considered in this study: single-phase (panel *a*), $\mu_r = 1$ (panel *b*), $\mu_r = 50$ (panel *c*), $\mu_r = 100$ (panel *d*).

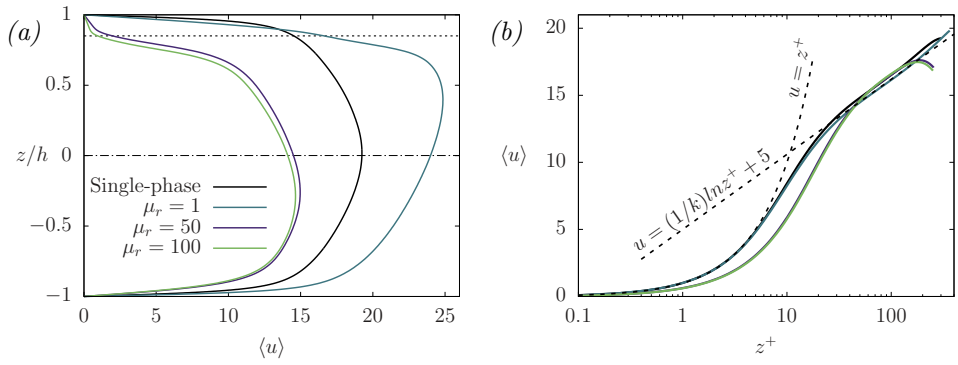


FIGURE 3.3 – Panel *a*: wall-normal behaviour of the mean streamwise velocity $\langle u \rangle$ as a function of $z/h$. The nominal interface position is shown with a dotted line, while the position of the channel centreline is shown with a dash-dotted line. Panel *b*: wall-normal behaviour of the mean streamwise velocity $\langle u \rangle$ in the water layer, rescaled based on the actual value of the friction velocity at the bottom wall, $u_{\tau,bot}$. Also shown in panel *b* is the law of the wall: $u^+ = z^+$ and $u^+ = (1/k)\log(z^+) + 5$ (where $k = 0.41$ is the von Kármán constant [169]). The different cases are reported with different colours: single-phase (black), $\mu_r = 1$ (blue), $\mu_r = 50$ (violet), $\mu_r = 100$ (green).

| Simulation | $\mu_r$ | $Q_o/Q_{SP}$ | $Q_w/Q_{SP}$ | $Q_t/Q_{SP}$ | $\Delta Q$ % |
|---|---|---|---|---|---|
| Single-phase | - | - | - | 1.0000 | - |
| M1 | 1 | 0.0436 | 1.2261 | 1.2698 | + 26.98 % |
| M2 | 50 | 0.0034 | 0.6872 | 0.6906 | - 30.94 % |
| M3 | 100 | 0.0016 | 0.6601 | 0.6617 | - 33.83 % |

TABLE 3.2 – Flow rate measurement for the different simulations: $Q_o$, $Q_w$ and $Q_t$ correspond to the flow rates of the thin layer (oil), of the thick layer (water), and of the entire flow oil-water flow, respectively, while $Q_{SP}$ is the flow rate of the reference single-phase case. The quantity $\Delta Q$ represents the increase (in percentage) of the total flow rate between the two-phase and the single-phase flow simulations.

compared to the single-phase case. In contrast, when the thin layer has a much larger viscosity than the thick layer, i.e. $\mu_r = 50$ and $\mu_r = 100$, the flow rate is reduced by about 30% and 34%, respectively. Given that the mean pressure gradient is constant for all simulations, the modification of the flow rate can be associated with a reduction of drag for the matched viscosity case [4] and an increase of drag for the other two cases with a more viscous fluid in the thin layer.

### 3.2.3 Stress budget

To analyse in more detail the modifications produced by the introduction of a thin viscous layer in the flow, we look at the stress behaviour as a function of the wall-

normal coordinate z. The mean stress can be expressed as

$$\tau_{tot} = \underbrace{\frac{\langle \mu(z) \rangle}{Re_\tau} \frac{\partial \langle u \rangle}{\partial z}}_{\tau_v} - \underbrace{\langle u'w' \rangle}_{\tau_t} + \underbrace{\frac{3}{\sqrt{8}} \frac{Ch}{We} \left\langle \frac{\partial \phi}{\partial x} \frac{\partial \phi}{\partial z} \right\rangle}_{\tau_c}, \tag{3.2}$$

indicating that the total stress $\tau_{tot}$ is the sum of three contributions: the viscous stress, $\tau_v$, the Reynolds or turbulent stress, $\tau_t$, and the capillary stress, $\tau_c$. The wall-normal behaviour of the stresses averaged along the two homogeneous directions $x$ and $y$ and in time is shown in Fig. 3.4. For all considered cases, the total stress – shown in Fig. 3.4*a* with a dashed line – is a linear function of $z$. The sum of the absolute values of the stress evaluated at the two walls is constant and equal to 2 for all cases, since the wall-shear stress balances the mean pressure gradient used to drive the flow, which is kept constant and equal to $\overline{\nabla p} = -1$. In Fig. 3.4*a*, we also show the wall-normal behaviour of the Reynolds stress, $\tau_t$, for all cases (continuous line). Compared to the single-phase case, for which $\tau_t$ is anti-symmetric about the channel centreline, the introduction of thin layer near the top wall induces remarkable changes. For $\mu_r = 1$, there is a significant reduction of $\tau_t$ around the liquid-liquid interface and in the thin layer, due to the blockage effect induced by the presence of the compliant liquid-liquid interface [4]. By contrast, in the bottom part of the channel, we observe an opposite behaviour, with $\tau_t$ much larger than the single-phase case, as a consequence of the increased turbulence activity. For $\mu_r = 50$ and $\mu_r = 100$, $\tau_t$ is almost vanishing inside the thin viscous layer, due to the large fluid viscosity, while it becomes larger below the liquid-liquid interface, which in this case is perceived as a solid boundary by the flow, hence actively contributing to the turbulence production (larger $\tau_t$). On the other hand, $\tau_t$ decreases near the bottom wall, because of the already observed turbulence reduction there.

Considering now the capillary stress, shown in the inset of Fig. 3.4*a*, we observe that is larger for $\mu_r = 1$, and smaller for $\mu_r = 50$ and $\mu_r = 100$. Given that the flow in the thin layer tends to be laminar, the liquid-liquid interface acts – via the capillary stress – as an active barrier against momentum transport between the thick and the thin layer.

The wall-normal behaviour of the viscous stress $\tau_v$ is shown in Fig. 3.4*b*. For $\mu_r = 1$, the viscous stress at the top wall is lower than the reference single-phase flow and is characterized by a non-monotonic transition across the interface, while it decrease towards zero below the interface, similarly to the single-phase case at the same distance from the wall. At the bottom wall, the viscous stress is $\sim 50\%$ higher, due to the increase of the mean velocity gradient in that region (see Fig. 3.3*a*). For $\mu_r = 50$ and $\mu_r = 100$, the viscous stress is significantly higher at the top wall, because of the high viscosity, and remains high over a much larger distance from the wall – down to $z/h \approx 0.5$. At the bottom wall the situation is reversed, and the viscous stress is smaller than the single-phase case. In summary, the presence of the thin layer leads to a sharp gradient in the mean velocity profile below the interface, which is associated with an increased shear stress between the two fluid layers. This is true in particular for $\mu_r = 50$ and $\mu_r = 100$, and is also the reason behind the increased production of turbulent kinetic energy in that region, where turbulence intensity can be even higher compared to the region near the bottom wall (see Fig. 3.2*d*). Therefore, when high

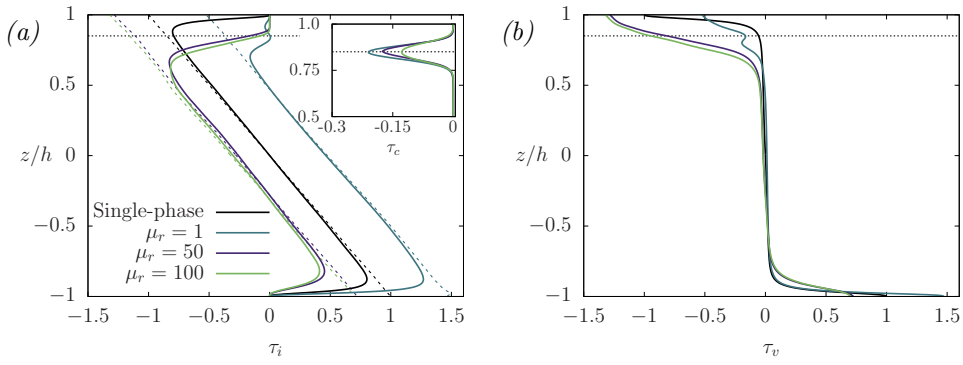


FIGURE 3.4 – Panel *a*: wall-normal behaviour of the Reynolds stress (solid lines), total stress (dashed lines) and capillary stress (inset) as a function of the wall-normal coordinate $z/h$. Panel *b*: wall-normal behaviour of the viscous stress as a function of the wall-normal coordinate $z/h$. The different cases are reported with different colours: single-phase (black), $\mu_r = 1$ (blue), $\mu_r = 50$ (violet), $\mu_r = 100$ (green). The dotted line marks the mean interface level.

viscosity ratios are considered, the thick layer perceives the liquid-liquid interface as an almost rigid boundary, which is a situation that is not observed for $\mu_r = 1$.

## 3.3 Interface statistics

In this section, we present a space-time characterization of the interface that separates the two liquid layers, for the different cases considered in this study.

### 3.3.1 Spatial characterization of the interface deformation

In Fig. 3.5 we show the instantaneous shape of the liquid-liquid interface for the three different two-phase flow cases considered here: Fig. 3.5a refers to $\mu_r = 1$, Fig. 3.5b refers to $\mu_r = 50$ and Fig. 3.5c refers to $\mu_r = 100$. Together with a three dimensional rendering of the liquid-liquid interface (left column), we also show – for each case – a close-up view of the interface elevation $\eta/h$ (as defined in Fig. 3.1) along the streamwise direction $x/h$, and measured at spanwise location $y = 0$. At a first glance, the interface shape, regardless of the value of $\mu_r$, seems characterized by the presence of waves. In our setting, in which the two fluid layers have the same density and the role of gravity is ruled out, these waves are pure capillary waves in which the restoring force is the surface tension. We notice also that the interface deformation shows remarkable differences for the high viscosity ratio cases, $\mu_r = 50$ and $\mu_r = 100$, compared to the matched viscosity case, $\mu_r = 1$. In particular, instead of multiple different wavelengths of moderate wave amplitudes observed for the matched viscosity case, the interface deformation for the two cases at large viscosity ratio is characterized by a regular wave pattern. This pattern is very pronounced at $\mu_r = 100$, and is characterized by a steep windward side (up to the crest), followed by a much less steep lee side (down to the trough). The values of the root mean square elevation for each case are: $\sqrt{\langle\eta^2\rangle} = 2.7 \times 10^{-2}$ ($\mu_r = 1$), $\sqrt{\langle\eta^2\rangle} = 3.6 \times 10^{-2}$ ($\mu_r = 50$), $\sqrt{\langle\eta^2\rangle} = 4.0 \times 10^{-2}$

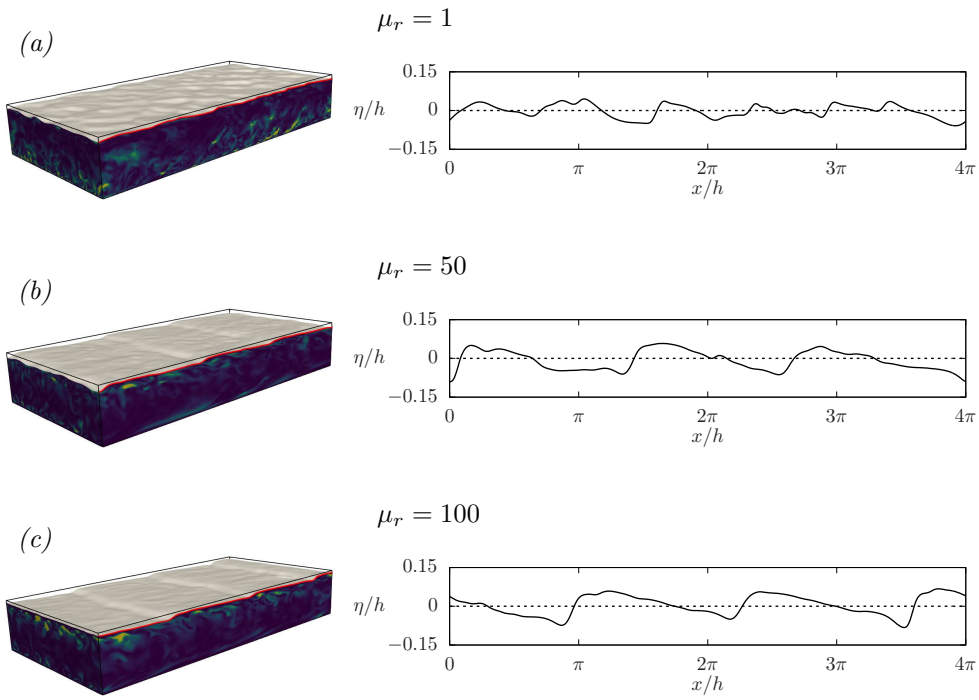


FIGURE 3.5 – Three-dimensional rendering of the instantaneous interface deformation (left), and corresponding profiles of the interface elevation $\eta$ (right), measured as a function of the streamwise direction $x$ at a given $y$ position. Each panel refers to a different case: $\mu_r = 1$ (panel $a$), $\mu_r = 50$ (panel $b$) and $\mu_r = 100$ (panel $c$).

($\mu_r = 100$), and indicates that waves grow in amplitude as the viscosity ratio increases. It is interesting to note that the shape of the interface elevation at large viscosity ratio looks similar to the so-called "bamboo wave" structure observed in oil-water core annular flows in pipes [170, 157].

To quantify the influence of the viscosity ratio on the deformation of the liquid-liquid interface, we look at the Probability Density Function (PDF) of the interface elevation normalized by its root mean square value, for each case. Results are shown in Fig. 3.6. We can observe that, for $\mu_r = 1$, the probability density is maximum near the mean interface location $\langle\eta\rangle = 0$, and it is negatively skewed due to the effect of wall confinement (waves are larger towards the centre of the channel than towards the wall). Note indeed that the wall is located at a distance of $0.15h$ from the nominal interface position, and therefore there is a vanishing probability of extreme events with positive interface elevations compared to extreme events with negative interface elevations. For the high viscosity ratio cases, the probability density function is bimodal, and the major mode is positive. This suggest a larger presence of wave crests than troughs. The bimodal distribution also indicates the persistence of wave crests and troughs with specific amplitudes, corresponding to the two modes of the distribution.

Naturally, the interface deformation is two-dimensional, and waves propagate at the interface along $x$ and $y$. This is visualised in Fig. 3.7 for the three different cases: Fig.

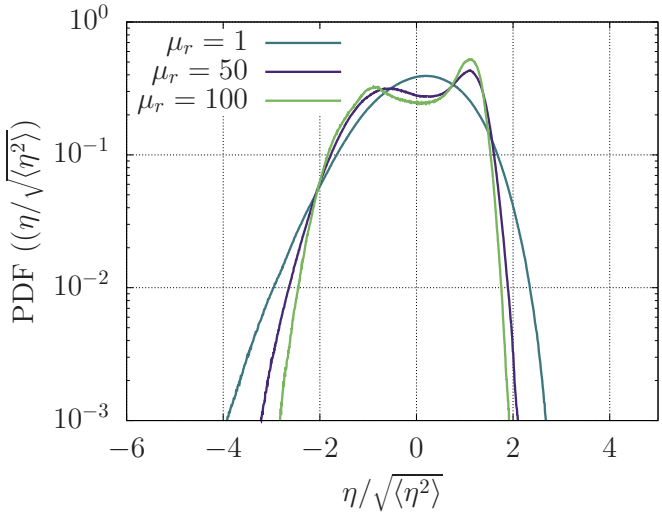


FIGURE 3.6 – Probability Density Function (PDF) of the interface elevation $\eta$, normalized by the root mean square (RMS) of the interface elevation, $\sqrt{\langle\eta^2\rangle}$. The different cases are reported with different colors: $\mu_r = 1$ (blue), $\mu_r = 50$ (violet) and $\mu_r = 100$ (green).

3.7a refers to $\mu_r = 1$, Fig. 3.7b refers to $\mu_r = 50$ and Fig. 3.7c refers to $\mu_r = 100$. Beside the three dimensional rendering of the liquid-liquid interface (left column) we now show the contour maps of the entire interface elevation, $\eta(x, y)$ (right column), for the three different values of the viscosity ratio. Compared to the case $\mu_r = 1$, for which the interface deformation does not show a regular pattern, for the cases $\mu_r = 50$ and $\mu_r = 100$ the interface deformation looks much more regular and quasi-1D (along $x$), with only little perturbations along $y$. This is properly quantified in Fig. 3.8, by looking at the two-dimensional time-averaged wavenumber power spectra of wave elevation $\overline{S_\eta\,(k_x, k_y)}$. This quantity represents the distribution of energy at the different wavenumbers $k_x$–$k_y$. For $\mu_r = 1$, the power spectrum appears isotropic, with almost no sign of preferential distribution. On the other hand, for $\mu_r = 50$ the energy distribution is more focused along the streamwise direction, $k_x$. This effect is even more pronounced for $\mu_r = 100$, where we can also observe the presence of spectral peaks at certain discrete wavenumbers.

To compare more closely the structure of the interface deformation for the three different $\mu_r$, we average the two-dimensional power spectra of wave elevation, $\overline{S_\eta\,(k_x, k_y)}$, along the y direction, so to obtain the streamwise spectra of the interface elevation, $\overline{\langle S_\eta\,(k_x)\rangle}$. Results are shown in Fig. 3.9. We observe that, unlike the smooth distribution of energy as a function of the streamwise wavenumber $k_x$ at $\mu_r = 1$, the wave energy for the cases $\mu_r = 50$ and $\mu_r = 100$ is concentrated at specific discrete wavenumbers. This suggests that the wave field is dominated by the presence of a "parent" wave, on top of which other less energetic waves (having wavenumber that is a multiple of that of the parent wave) can propagate. The peak wavenumber is $k_{x,peak} = 1.5$ for $\mu_r = 50$ and $\mu_r = 100$ (or, in terms of wavelength, $\lambda_{peak} = 4\pi/3$) and corresponds to the presence of $N \approx 3$ waves inside a domain of length $L_x = 4\pi$. This is

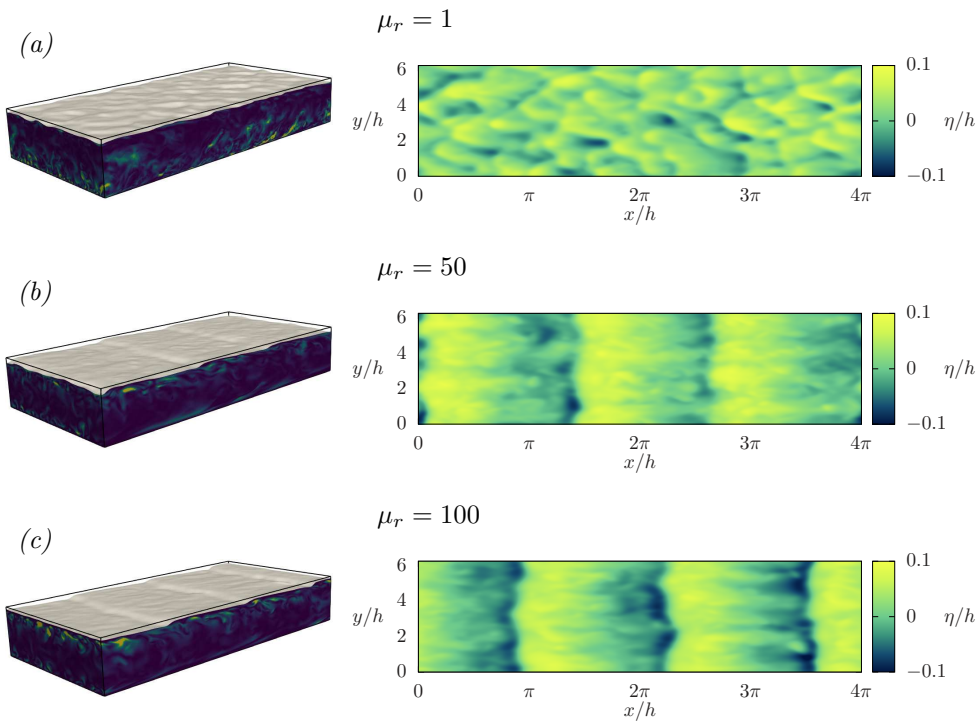


FIGURE 3.7 – Three-dimensional rendering of the instantaneous interface deformation $\eta$ (left), and corresponding two-dimensional contour maps of $\eta$ (right). Each panel refers to a different case: $\mu_r = 1$ (panel *a*), $\mu_r = 50$ (panel *b*) and $\mu_r = 100$ (panel *c*)

in agreement with the patterns shown in Fig. 3.5*b*,c and 3.7*b*, *c*. This suggests a highly anisotropic situation and agrees with the qualitative observation of waves developing only across the streamwise direction and being self-similar across the channel span.

### 3.3.2 Temporal characterization of the interface deformation

So far, we examined the spatial behaviour interface waves. We now move to the time characterization of waves. Note that, since the interface is advected at a mean velocity (see Fig. 3.3*a*) wave frequencies are Doppler shifted to higher frequencies. The mean advection velocities for the three cases are: $\langle u_i \rangle \approx 16.5$ ($\mu_r = 1$), $\langle u_i \rangle \approx 1.9$ ($\mu_r = 50$) and $\langle u_i \rangle \approx 0.9$ ($\mu_r = 100$). Therefore, in order to isolate the wave frequencies, a shift of the interface elevation signal is applied as $\eta'(x,t) = \eta(x + dx_{shift}, t)$, where $dx_{shift} = \langle u_i \rangle / df_{samp}$ and $df_{samp}$ is the frequency at which the interface elevation is sampled [90]. Space-averaged frequency power spectra of wave elevation $\langle S_\eta(\omega) \rangle$ of the shifted wave signals for each case are reported in Fig. 3.10. The minimum angular frequency on the x-axis ($\omega_{min} = 0.628$) corresponds to the overall duration of the recorded wave signal. We note even here a remarkable difference between the case $\mu_r = 1$ and the other two cases at higher viscosity ratio. In particular, while for $\mu_r = 1$ energy is evenly distributed over a broad range of frequencies – before it

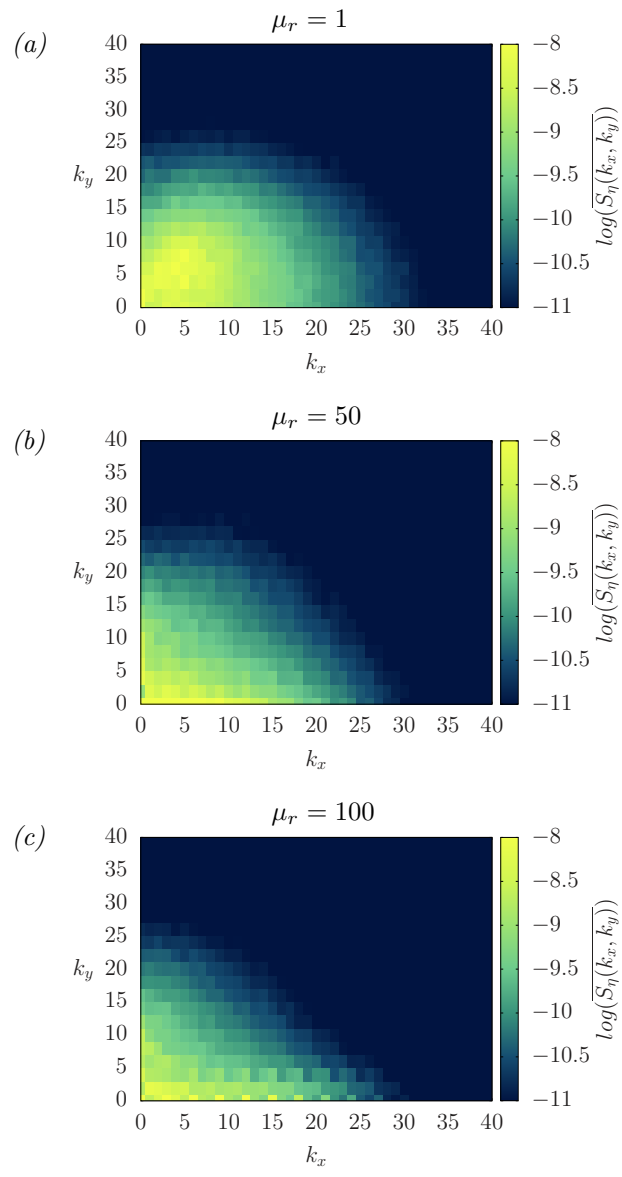


FIGURE 3.8 – Two-dimensional time-averaged wavenumber power spectra of the interface elevation, $\overline{S_\eta\,(k_x, k_y)}$. Each panel refers to a different case: $\mu_r = 1$ (panel *a*), $\mu_r = 50$ (panel *b*), $\mu_r = 100$ (panel *c*).

starts diminishing at higher frequencies – for $\mu_r = 50$ and $\mu_r = 100$ the energy is concentrated over a narrow range in the low-frequency region of the spectrum, and it vanishes rapidly as the frequency increases. This suggests that at large viscosity ratio the waves oscillate so slowly that their oscillation is not even perceived, and waves

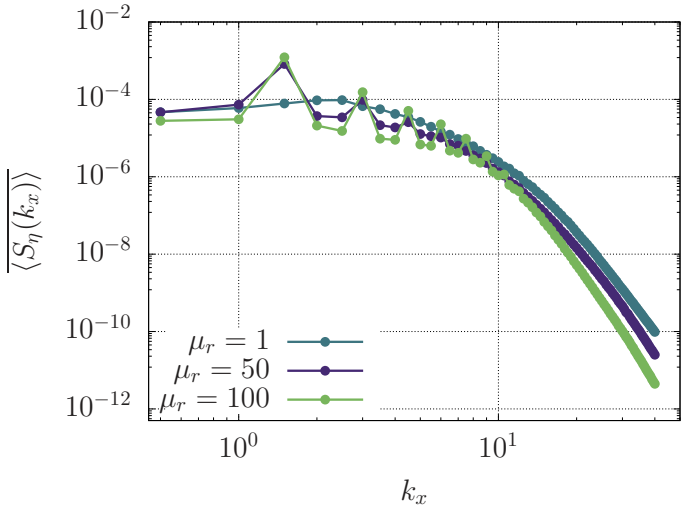


FIGURE 3.9 – Streamwise wavenumber power spectra of the interface elevation, $\overline{\langle S_\eta\,(k_x)\rangle}$, averaged in space (over the spanwise direction) and in time. Results are shown for $\mu_r = 1$ (blue), $\mu_r = 50$ (violet) and $\mu_r = 100$ (green).

seem rigidly advected by the flow.

We will now proceed to characterize the wave propagation based on two-dimensional space-time spectral analysis. Note that in the case $\mu_r = 1$ the interface is advected with a mean advection velocity of $\langle u_i^{\mu_r=1}\rangle \approx 16.5$. The corresponding velocities for the cases $\mu_r = 50$ and $\mu_r = 100$ are $\langle u_i^{\mu_r=50}\rangle \approx 1.9$ and $\langle u_i^{\mu_r=50}\rangle \approx 0.9$, respectively. This means that the wave speed is doppler shifted and therefore a proper shift has to be applied to the interface elevation data in order to obtain the dispersion relation. The velocity of propagation or celerity of a wave with a known frequency and wavenumber is defined as: $c = \omega/k$. For waves of moderate and low wave steepness or linear waves [125, 137] the linear dispersion relation (LDR) describes the frequency as a function of the wavenumber and therefore predicts the wave celerity. The LDR for waves propagating at the interface between two fluids of the same density, over a finite depth $d$ (in our case $d = 0.15h$) can be expressed in its non-dimensional form as follows:

$$\omega^2 = \frac{k^3}{2We}\tanh(0.15k) \tag{3.3}$$

To obtain information on the wave propagation, based on our numerical results, we resort to two-dimensional frequency-wavenumber power spectra of wave elevation $S_\eta\,(k_x, \omega)$, which are presented in Fig. 3.11. Note that the procedure, described above, concerning the shift of the wave signal in an advection-free frame of reference has been applied here prior to transforming the signals to the wavenumber-frequency space. In Fig. 3.11*a* the results for case $\mu_r = 1$ show that the maximum of the wave energy (marked with black crosses) is localized near the prediction of the LDR (red dashed line). This indicates that the individual wavelengths, which are formed at the interface between the two fluids, propagate at a velocity that can be well predicted by the linear

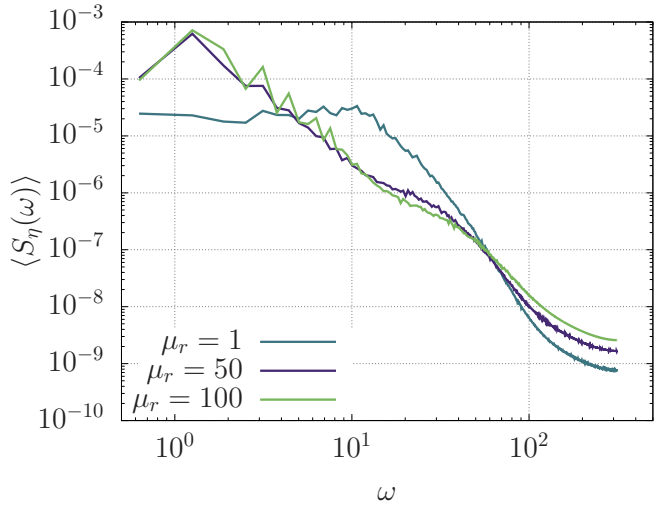


FIGURE 3.10 – Space-averaged frequency power spectra of wave elevation, $\langle S_\eta(\omega)\rangle$ computed using the shifted wave signal. The different cases are reported with different colors: $\mu_r = 1$ (blue), $\mu_r = 50$ (violet) and $\mu_r = 100$ (green).

wave theory. The situation is different for the two cases with high viscosity ratio. In particular, for the case $\mu_r = 50$ we observe a very narrow-band energy distribution in terms of wave frequencies, while the frequency range becomes even narrower for the case $\mu_r = 100$, where the energy of all the discrete wavenumber modes, is concentrated at the same low frequency. Therefore, for the cases with high viscosity ratio the higher wavenumber modes do not satisfy the dispersion relation, but instead propagate at a low speed that is similar to the celerity of the dominant wave mode.

## 3.4 Conclusions

In this chapter, the DNS results from a stratified flow configuration, in which a thin layer of oil flows on top of a thick layer of water were presented. Three different values of the oil-to-water viscosity ratio, $\mu_r = 1$, $\mu_r = 50$ and $\mu_r = 100$ are used, and their influence on the turbulence modulation and on the dynamics of the liquid-liquid interface is considered. Results show that, compared to the reference single-phase turbulent flow, the introduction of a thin fluid layer, characterized by a viscosity equal or larger than that of the thick layer, modifies the overall velocity profiles and the turbulence behaviour. In particular, the mean flow rate increases significantly for $\mu_r = 1$ and decreases significantly for $\mu_r = 50$ and $\mu_r = 100$. This is associated to a corresponding change of the drag coefficient. When the viscosity contrast between the two fluids is large, the liquid-liquid interface is perceived as a solid boundary by the thick water layer, leading to high shear stress and a local increase in turbulent kinetic energy production around it. We also observe that the near-wall turbulent cycle at the bottom wall (at the bottom of the thick layer) is influenced as well by

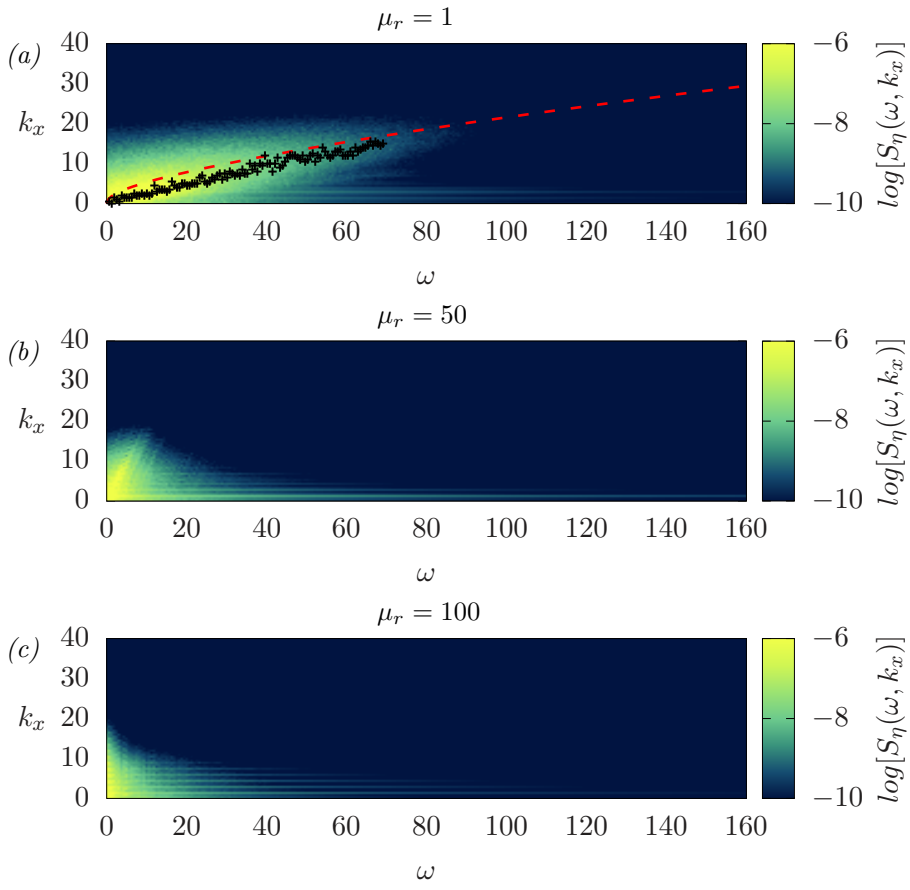


FIGURE 3.11 – Frequency-wavenumber power spectra of wave elevation for $\mu_r = 1$ (panel *a*), $\mu_r = 50$ (panel *b*), $\mu_r = 100$ (panel *c*). The dashed red line corresponds to the Linear Dispersion Relation (LDR) for capillary waves while the black crosses correspond to the maxima of the numerical results.

the thin layer viscosity. In addition, the structure and the dynamics of the liquid-liquid interface show remarkable changes by changing the viscosity ratio between the two fluids. Specifically, we observe a transition from a regime characterized by the presence of an almost isotropic wave field for the matched viscosity case $\mu_r = 1$, to a regime characterized by regular long waves with short crests and long troughs for high viscosity ratios. The wave structure in these latter cases seems to resemble the so-called "bamboo waves" observed in oil-water pipe flows. Finally, the temporal analysis of the wave signals reveals that while for the matched viscosity case $\mu_r = 1$ waves oscillate at different frequencies over a rather broad range of values, for high viscosity ratios waves oscillate at a specific very low frequency, thus generating an interface deformation that seems purely advected by the mean flow velocity. Indeed, space-time analysis of the wave signals reveals that for the matched viscosity case waves propagate at celerities that can be well predicted by the linear dispersion relation, while for the high viscosity

ratio cases, waves are almost rigidly advected by the mean flow velocity.

# 4

# Conclusions and future developments

Throughout this thesis numerical simulations of two-phase liquid-liquid flows in a plane channel configuration have been performed using a coupled Direct Numerical Simulation (DNS) - Phase-Field Method (PFM) technique. First, the case of capillary waves forced by hydrodynamic turbulence in a two-layer oil-water channel flow configuration was examined. Second, the flow of a thin laminar layer over a thick turbulent layer in a channel was examined. Finally, a multiple resolution strategy for the improvement of the performance of the DNS-PFM technique has been proposed and tested and its ability to decrease the computational time and memory usage up to 40% was demonstrated.

In Chap. 2, two sets of parametric studies have been performed. The first study was performed at a variable viscosity ratio between the two fluid layers. It was found that the wave dynamics are primarily depended on the interaction between inertial and surface tension forces and not on viscous forces. The frequency and the wavenumber spectra of wave elevation of the capillary waves in both cases showed the same scaling laws for both viscosity ratio cases examined. Namely, at larger scales a scaling of $S_\eta(k) \sim k^{-1}$, compatible with the large-scale energy equipartition assumption was found. At smaller scales an initially mild slope which is close to the prediction of the weak wave turbulence theory, $S_\eta(k) \sim k^{-4}$, is observed over a very short range and transitions to a much steeper slope, $S_\eta(k) \sim k^{-6}$, with the transition occurring close to the Kolmogorov-Hinze scale, where inertial and surface tension forces are balanced. The frequency-wavenumber spectra reveal that waves propagate according to the prediction of the linear dispersion relation. The energy analysis reveals that only a small part of the total injected power by the mean pressure gradient goes to the waves. The second parametric study was performed at a variable Weber number. Keeping the rest of the parameters fixed the increase of the Weber number is equivalent to a decrease of the magnitude of surface tension forces with respect to the magnitude of inertial forces. Unlike, the viscosity, surface tension plays a crucial role on the behaviour of the liquid-liquid interface. Both wave height and wave steepness increase substantially with the increase of the Weber number. Reducing surface tension corresponds to a shift of the critical Kolmogorov-Hinze scale to shorter wavelengths. The wavenumber spectra show that the inertial regime is extended to higher wavenumbers, following

this shift.
In Chap. 3, the flow of a thick turbulent layer over a thin laminar layer at variable viscosity ratio was examined. A single parametric study has been performed based on the viscosity ratio between the layers. The shift of the flow and interface statistics was found to be dramatic when the viscosity ratio is increased by one order of magnitude. When the two layers have the same viscosity, waves of multiple wavelengths propagate at the interface with a celerity that is closely predicted by the dispersion relation for capillary waves. When the viscosity of the thin layer is increased, a nearly rigid monochromatic wave pattern is formed and is passively advected by the mean flow.
A major future development of this work is the study of turbulence-induced breaking of waves in the liquid-liquid configuration. Indeed, the turbulence-induced wave breaking is an unaddressed problem in scientific literature, despite the fact that dispersion of oil and water can originate from such initially stratified configurations. The prediction of a wavelength based critical Weber number, $We_{cr}$, in liquid/liquid flow configurations could therefore be catalytic for the design of industrial flows. Based on our present knowledge, a detailed database containing a space-time quantification of turbulence-induced wave breaking has not been obtained neither from a numerical nor from an experimental study. On the other hand, recent results from DNS of wave breaking due to gravity [171, 172] show that the latest advancements in computer power in combination with sophisticated numerical techniques, finally allow for the exploration of such complex physical phenomena of multiphase turbulent flow. Indeed, exploiting the recent development of the multiple resolution strategy, we performed preliminary simulations to test the capacity of the method to tackle complex problems involving phenomena of breakage and coalescence. In particular, the breakage of a thin fluid layer by a surrounding turbulent flow was examined using different resolution levels. These results are presented in Appendix D.

# A

# Single-phase shear-driven turbulent flow

The flow field solver decoupled from the phase-field solution is benchmarked here for the case of a single-phase plane turbulent Couette flow. Plane turbulent Couette flow has been a topic of interest for many studies over the past [173, 174, 175], but also more recent [176, 177, 178] years. Despite its simplicity, this type of shear-driven flow configuration, with two parallel walls of a plane channel moving at different speeds and no imposed pressure gradient, has been proven challenging to simulate. The main reason for this is that unlike the case of plane Poiseuille flow, which has been readily accessible to DNS [59], plane Couette flow is characterized by the onset of large-scale structures, which are correlated across the streamwise direction of the channel. These structures take the form of large-scale, counter-rotating pairs of weak vortexes/rollers occupying the full height and width of the channel. For this reason, box sizes of at least $L_x > 19\pi h$ and $L_y > 5\pi h$, with $h$ being the half-channel height, are needed to accommodate at least one complete wavelength of the large-scale rollers across the streamwise direction and a representative number of roller pairs across the spanwise [173, 175].

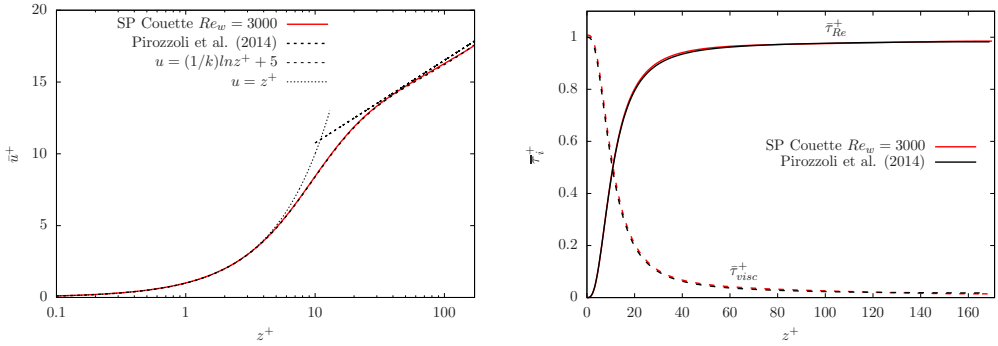


FIGURE A.1 – Mean velocity profile (left) and stress behaviour (right) from the simulation of the single-phase Couette flow. Results are compared to those of Pirozzoli et al. [177].

A plane Couette flow has been preformed to examine the agreement of the solution of

the Navier-Stokes equations in a single-flow configuration to existing literature results. In this setup, the two-channel walls move in parallel, but in opposite directions, with non-dimensional velocities, $u_w = +1$, at the top wall and $u_w = -1$, at the bottom wall. A Reynolds number of $Re_w = 3000$ has been selected considering the wall velocity as a reference and the half-channel height as a characteristic length scale. This results to a corresponding shear Reynolds number of $Re_\tau \approx 171$ [177]. The simulation parameters used are summarized in table A.1.

| Simulation | $Re_w$ | $N_x$ | $N_z$ | $N_y$ | $L_x$ | $L_y$ | $L_z$ | $\Delta_x^+$ | $\Delta_y^+$ | $\Delta_z^+$ |
|---|---|---|---|---|---|---|---|---|---|---|
| $SP - Couette$ | 3000 | 2048 | 513 | 512 | $16\pi h$ | $4\pi h$ | $2h$ | 4.2 | 4.2 | 1.0 |

TABLE A.1 – Overview of the main simulation parameters used for the simulation of the single-phase Couette flow.

In Fig. A.1 (left) the mean velocity profile is shown, while in Fig. A.1 (right) the viscous and Reynolds stress profiles are shown. Note that the box size used is smaller the one prescribed in literature [173, 175], however both the mean and the fluctuating flow field properties, agree almost perfectly with those of Pirozzoli et al. [177], which were obtained for the same Reynolds number $Re_w = 3000$, but with a channel of dimensions, $L_x = 18\pi h$, $L_y = 8\pi h$, $L_z = 2h$. The channel width accommodates three pairs of counter-rotating vortexes, as it can be observed by looking at the patterns of the high and low streamwise velocity regions at the vertical crossplane shown in Fig. A.2a and at the high and low speed streak structures at the horizontal centreplane shown in Fig. A.2b.

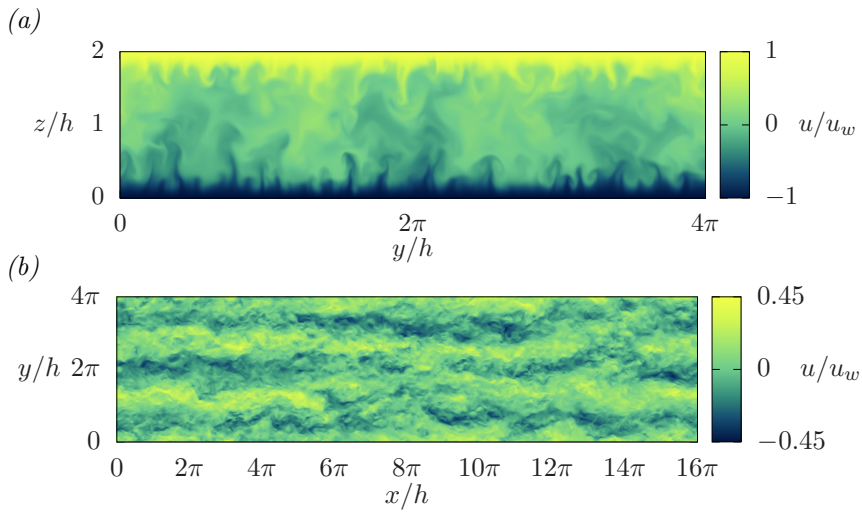


FIGURE A.2 – (a) Instantaneous map of the steamwise velocity, $u$ over a cross-section of the channel. (b) Instantaneous map of the steamwise velocity, $u$ over the horizontal centreplane at $z/h = 1$.

# B

# Coarsening, shrinkage and domain size effects

The accuracy of the simulation results in terms of the applied grid resolution and the adequacy of the selected domain size is examined here. First, we examine the presence of shrinkage of the phase-field for the resolution that was used for all simulations i.e. a Cahn number of $Ch = 0.02$. As it was discussed in Sec. 1.1, shrinkage is one of the main drawbacks of the PFM and high resolutions or special techniques are required to prevent shrinkage from taking place in problems involving breakage and coalescence of droplets in turbulence. Here, we examine the level of shrinkage in the simulations with non-breaking capillary waves presented in Chap. 2. The problem of shrinkage is directly associated with spurious mass transfer from one phase into the other. Therefore, in order to quantify the mass conservation of each phase, we monitor the evolution of the mass of one of the two phases (oil) during the simulation. In Fig. B.1, we show the results for the different cases. The percentage change of the mass of oil with respect to its initial mass, $M_0$ is reported as a function of the simulation time expressed in wall-units, $t^+$. It is clear that for all simulations the mass is conserved. Therefore, for the simulations of non-breaking capillary waves, where the interface remains continuous without undergoing arbitrary topological modulations the phase-field equilibrium profile is retained accurately throughout the whole simulation time. This also implies that the variation of the thermophysical properties across the thin transition layer between the two phases are well captured, while surface tension forces are also well represented.

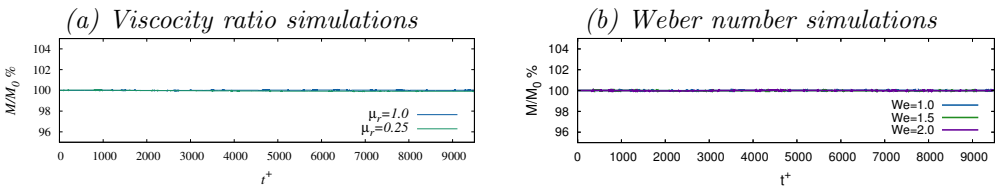


FIGURE B.1 – Mass conservation for the different two-layer flow simulations. Left: simulations at variable viscosity ratio, right: simulations at variable Weber number.

The effect of the domain size is examined next. Indeed, the use of a finite domain size

restricts the maximum wavelength that can be captured by the simulations. To check the adequacy of the selected domain size i.e. $L_x = 8\pi h$ and $L_y = 2\pi h$, a simulation with a domain of double the size, i.e. $L_x = 16\pi h$ and $L_y = 4\pi h$, was performed. In addition, in order to check for effects of coarsening, due to the finiteness of the interfacial layer thickness, we performed an additional simulation with a transition layer of half the thickness (double the resolution) i.e. a Cahn number of $Ch = 0.01$. The multiple resolution strategy presented in Sec. 1.5 was used so to maintain the same resolution level for the Navier Stokes equations, while adopting a finer grid for the solution of the Cahn-Hilliard equation. The simulation with $Re_\tau = 300$, $\mu_r = 1.00$ and $We = 1.0$ was selected as the reference. The parameters for the the two validation simulations, together with those of the reference simulation, are summarized in Tab. B.1. Note that the grid size that is reported in Tab. B.1 for the simulation with $Ch = 0.01$ corresponds to the grid that is used for the phase-field transport equation, while the grid used for the momentum equation is the same as the one used for the reference simulation.

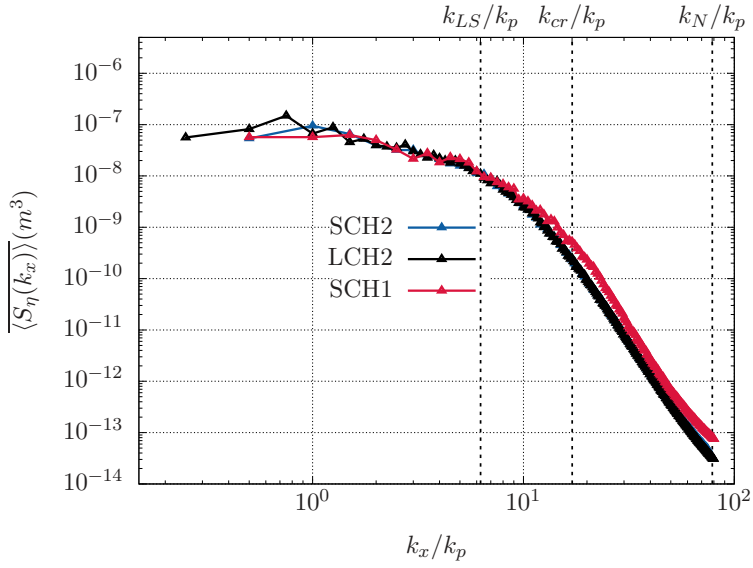


FIGURE B.2 – Streamwise wavenumber power spectra of wave elevation, $\overline{\langle S_\eta\,(k_x)\rangle}$, averaged in space (over the spanwise direction) and in time. Blue triangles correspond to the reference simulation (SCH2), black triangles to the simulation with double the domain size (LCH2) and red triangles to the simulation with $Ch = 0.01$ (SCH1).

The resulting wavenumber power spectra of wave elevation, $\overline{\langle S_\eta\,(k_x)\rangle}$ from the two validation simulations, together with the one from the reference simulation are shown in Fig. B.2. The domain size does not have any influence on the wave spectra besides the addition of a lower wavenumber (bigger wavelength), which is half (double) compared to the lowest wavenumber in simulation SCH2. The two spectra from the simulations LCH2 and SCH2 completely overlap in the rest of the wavenumber range. The results from the simulation SCH1 are also in very good agreement with those of the simulation SCH2. An increase of the wave energies of the smaller scale waves can

| Simulation | $Ch$ | $L_x$ | $L_y$ | $N_x$ | $N_y$ | $N_z$ | $\Delta_x^+$ | $\Delta_y^+$ | $\Delta_z^+$ |
|---|---|---|---|---|---|---|---|---|---|
| SCH2 | 0.02 | $8\pi$ | $2\pi$ | 1024 | 256 | 513 | 7.37 | 7.37 | 1.84 |
| LCH2 | 0.02 | $16\pi$ | $4\pi$ | 2048 | 1024 | 513 | 7.37 | 3.68 | 1.84 |
| SCH1 | 0.01 | $8\pi$ | $2\pi$ | 2048 | 512 | 1025 | 7.37 | 7.37 | 1.84 |

TABLE B.1 – Overview of the main simulation parameters for the reference simulation (SCH2), the simulation with double the domain size (LCH2) and the simulation with Ch=0.01 (SCH1). The number of grid points and the corresponding grid spacings in wall units are also reported.

be notices, which is indeed to be expected since smaller scale dynamics are captured better with a transition layer that is thinner. Note that the transition from the slope $k^{-4}$ to the slope $k^{-6}$ tends to become more distinct and even gets closer to the critical wavenumber $k_{cr}$ in simulation SCH1. In conclusion, the lack of shrinkage effects, the absence of a finite domain size influence and the small amount of coarsening effects suggest that the setup used for the simulations of Chap. 2 is adequate to capture accurately the dynamics of non-breaking waves in turbulence.

Finally, the adequacy of the domain size is tested for the case of the simulations of the thin laminar layer over the thick turbulent layer presented in Chap. 3. In order to ensure that even in this case the results are independent of the selected box size, a simulation using double the streamwise length, namely $L_x = 8\pi h$ instead of $L_x = 4\pi h$, was performed. The case of $\mu_r = 100$ was selected for this validation test, since in this case the most energetic wave appears at a large scale (at the wavenumber of $k_{x,peak} = 1.5$). A snapshot of the resulting interface deformation in the original simulation and in the simulation with double channel length is shown in Fig. B.3. The red box highlights the result of the simulation with $L_x = 4\pi h$, while the black box shows the result of the simulation with $L_x = 8\pi h$, but only over half of the streamwise length. One can observe that there is no difference in the dominant wave, which is similar between the two simulations and corresponds to a wavelength of $\lambda_{peak} = 4\pi/3$. The latter suggests that there are no finite-box effects associated to the onset of the dominant wavelength in the simulations presented in Chap. 3.

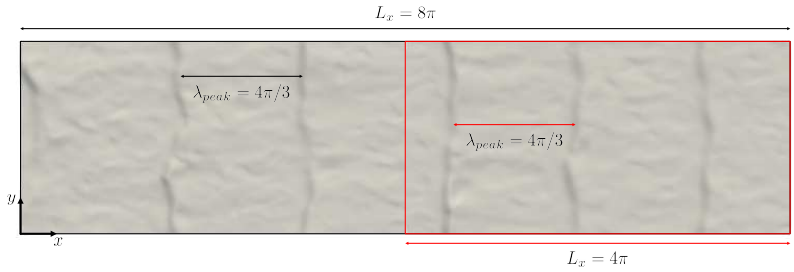


FIGURE B.3 – Snapshot of interface deformation for simulations with $L_x = 4\pi h$ and $L_x = 8\pi h$ at $\mu_r = 100$. The red box highlights the result of the simulation with $L_x = 4\pi h$, while the black box shows the result of the simulation with $L_x = 8\pi h$ over half of the streamwise length of the domain. The arrows highlight the dominant wavelength, which is in both cases approximately equal to $\lambda_{peak} = 4\pi/3$.

# C

# Validity of the matched densities assumption

To test the validity of the assumption of matched fluid densities that was used to describe the two-phase stratified oil-water flow, a simulation with a non-unitary density ratio was performed. In particular, the density ratio in this simulation was set to the realistic value of the density ratio between oil and water, namely $\rho_r = 0.9$. Therefore, buoyancy forces are also anticipated to influence the dynamics of the flow to a certain degree. Fig. C.1*a* shows the mean streamwise velocity profiles obtained in the case with $\rho_r = 1.0$ and $\mu_r = 100$ (green line) compared to the new case with $\rho_r = 0.9$ and $\mu_r = 100$ (violet points).

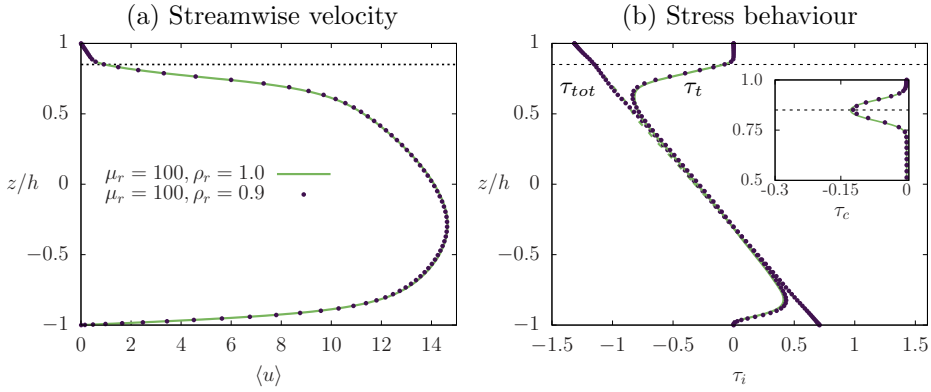


FIGURE C.1 – Panel *a* shows the wall-normal behaviour of the mean streamwise velocity $\langle u \rangle$, while panel *b* shows the behaviour of the total stress, the Reynolds stress, and the capillary stress (inset). Results that refer to the case with $\mu_r = 100$ and $\rho_r = 1.0$ are reported using green lines, while those referring to the case with $\mu_r = 100$ and $\rho_r = 0.9$ are reported using purple points. Only a subset of the available points is reported in the latter case so to increase the clarity of the comparison.

We can observe that the mean streamwise velocity profiles perfectly overlap. Fig. C.1*b* shows the behaviour of the total stress, the Reynolds stress, and the capillary stress (inset) along the wall-normal direction for the two cases. Also in this case there is almost a perfect overlap for every curve. Finally, the Probability Density Function (PDF) of the interface elevation $\eta$ is shown in Fig. C.2. A very small increase in

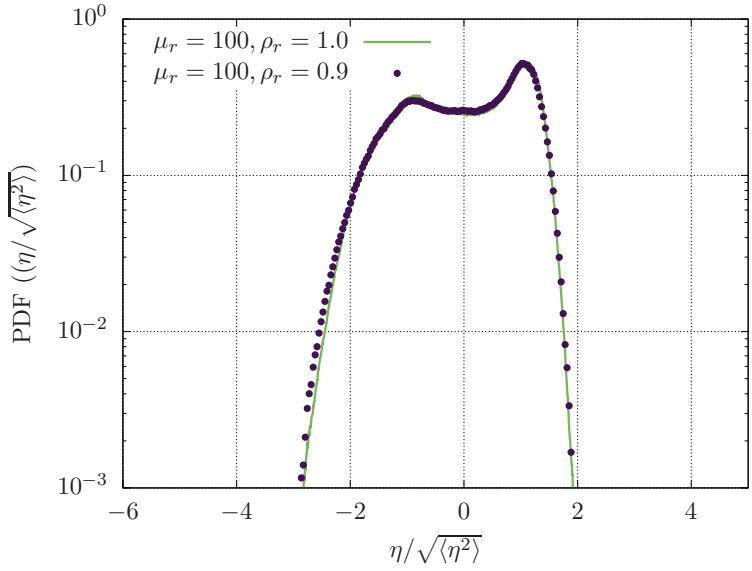


FIGURE C.2 – Probability Density Functions (PDF) of the interface elevation $\eta$, normalized by the root mean square (RMS) of the interface elevation $\sqrt{\langle\eta^2\rangle}$. Results that refer to the case $\mu_r = 100$ and $\rho_r = 1.0$ are reported using green lines, while those referring to $\mu_r = 100$ and $\rho_r = 0.9$ with purple points. Only a subset of the available points is reported in the latter case so to increase the clarity of the comparison.

the probability of negative rare events can be observed for the case with $\rho_r = 0.9$ compared to the case with $\rho_r = 1.0$.

# D

# Breakage of a thin liquid layer in turbulence

**Reproduced in part from:**
M. Schenk, G. Giamagas, A. Roccon, F. Zonta & A. Soldati, (2023) *Computationally efficient and interface accurate dual-grid phase-field simulation of turbulent drop-laden flows*, J. Fluids Eng. (in preparation)

Turbulent flows laden with drops are commonly encountered in a number of natural and industrial processes. Examples include the formation of raindrops in the atmosphere [179], wave breaking at the ocean surface [180, 181], the atomization and spray generation in fuel injection and combustion [182, 183, 184], the transmission of respiratory diseases [185, 186, 187] and many other flow instances [188, 189]. As an extension of our present work, we are aiming at studying the problem of turbulence-induced wave breaking at the interface between two liquids with properties similar to those of oil and water. This is a problem that is relevant in a series of industrial applications, in which upon varying the flow conditions dispersion of one fluid phase into the other in the form of droplets may occur and therefore it needs to be predicted and controlled [5, 6, 7].
The applicability of the multiple resolution strategy (dual-grid approach) proposed in Sec. 1.5 to a more computationally intensive and scientifically relevant case is considered here, by studying the breakage of a liquid layer in turbulence [190, 182, 191]. A thin liquid layer of thickness $0.15h$ is initially located at the centre of a pressure-driven turbulent channel, as sketched in Fig. D.1. At the two walls, no-slip and no-flux boundary conditions are enforced for the velocity field and for the phase-field variable and its second derivative, while periodicity is implicitly applied along $x$ and $y$ for all variables. The initial condition for the flow field is taken from a preliminary DNS of a single-phase fully developed turbulent channel flow at $Re_\tau = 150$, complemented by a proper definition of the initial distribution of the phase $\phi$, so that a thin liquid layer (thickness $0.15h$) is placed at the channel centreline. The liquid layer and the carrier fluid have the same density ($\rho_r = 1$) and viscosity ($\mu_r = 1$), while the value of the Weber number is set to $We = 3$.
We perform three different simulations (see table D.1) considering a computational domain having dimensions $L_x \times L_y \times L_z = 2\pi h \times \pi h \times 2h$ along the streamwise ($x$),

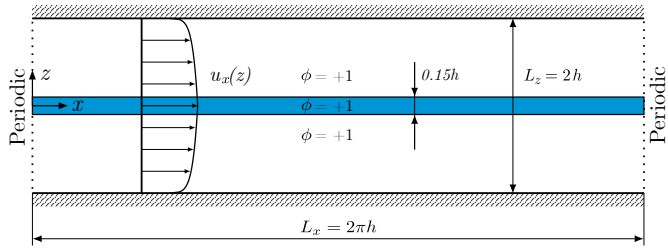


FIGURE D.1 – Sketch of the simulation setup used to simulate the breakage of a liquid layer in a turbulent channel flow. A thin liquid layer, thickness $0.15h$, is initially placed at the centre of a three-dimensional turbulent channel (the initial shape and location of the layer are represented in blue). The domain is three-dimensional, with dimensions $L_x \times L_y \times L_z = 2\pi h \times \pi h \times 2h$.

| Code | Refinement, $M_i$ | Grid NS | Grid CH | Ch | Pe |
|---|---|---|---|---|---|
| G1 | $1 \times 1 \times 1$ | $256 \times 128 \times 513$ | $256 \times 128 \times 513$ | 0.020 | 50 |
| G2 | $2 \times 2 \times 2$ | $256 \times 128 \times 513$ | $512 \times 256 \times 1025$ | 0.010 | 100 |
| G4* | $4 \times 4 \times 3$ | $256 \times 128 \times 513$ | $1024 \times 512 \times 1537$ | 0.0075 | 150 |

TABLE D.1 – Parameters for the simulations of the liquid layer breakage in a turbulent channel flow. By keeping fixed the resolution of the Navier-Stokes equation, the grid resolution used for the Cahn-Hilliard equation is increased. Simulations are labeled based on the employed refinement factor: case $G1$ (unitary refinement factor, same grid for NS and CH); case $G2$ (refinement factor equal to 2 in each direction); case $G4*$ (refinement factor of 4 along $x$ and $y$ directions, and 3 along $z$).

spanwise ($y$) and wall-normal direction ($z$), respectively. For all three simulations, the flow field is solved onto a computational grid consisting of $N_x \times N_y \times N_z = 256 \times 128 \times 513$ points, which guarantees a resolution of the flow field down to the Kolmogorov scale. The Cahn-Hilliard equation is discretized on progressively refined grids. In particular, we employ $N_x \times N_y \times N_z = 256 \times 128 \times 513$ for $G1$ (refinement factor of 1 in each direction, $M_i = 1$), $N_x \times N_y \times N_z = 512 \times 256 \times 1025$ for $G2$ (refinement factor of 2 in each direction, $M_i = 2$), and $N_x \times N_y \times N_z = 1024 \times 512 \times 1537$ for $G4^*$ (refinement factor of 4 along x and y, $M_x = M_y = 4$, and of 3 along z, $M_z = 3$). This corresponds to a Cahn number (and a corresponding Peclet number, $Pe = 1/Ch$) $Ch = 0.02$ ($Pe = 50$) for $G1$, $Ch = 0.01$ ($Pe = 100$) for $G2$ and $Ch = 0.0075$ ($Pe = 150$) for $G4^*$, so to guarantee that the transition layer between the two phases is represented by at least 3 grid points for all cases. We recall that the computational grid is uniform along $x$ and $y$, whereas it is non-uniform across $z$ (see section Sec. 1.4.2). An overview of the simulation parameters is given in Tab. (D.1), while the principal concept of the dual-grid approach is visualized in Fig. D.2.

The turbulent flow exerts shear forces on the thin liquid layer and leads to its fragmentation in drops of different sizes (atomization process). To characterize this transient dynamics, we consider behaviour of the normalized interfacial area $A(t)/A_0$ (defined as the area separating the two liquid phases, with $A_0$ its initial value). The resulting behaviour is shown in Fig. D.3, for the three different simulations. Note that the interface reconstruction and the computation of the transient evolution of the interfacial

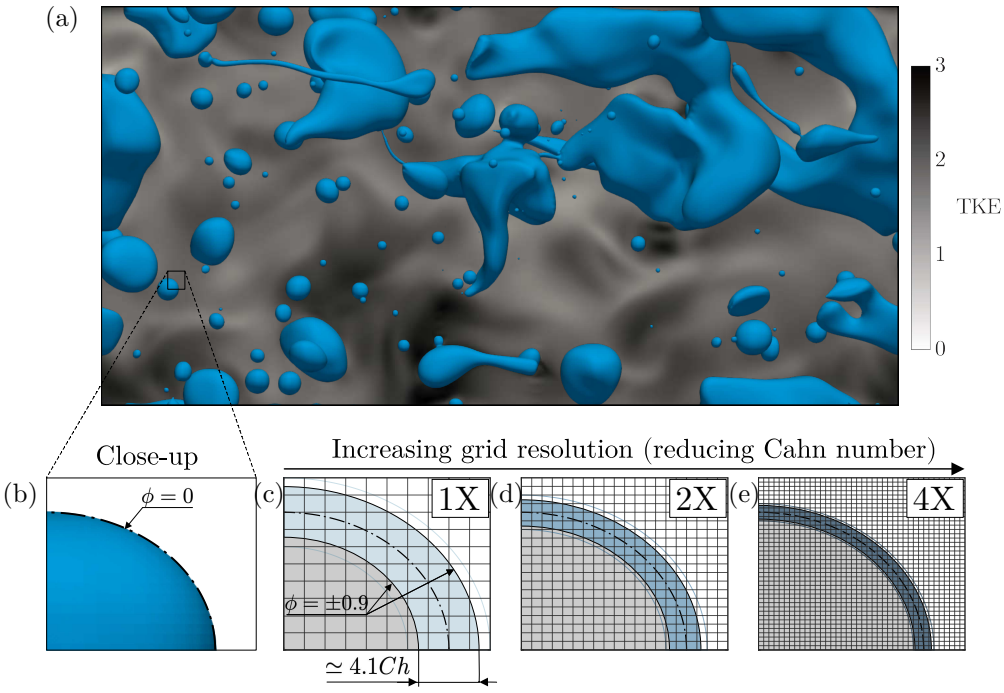


FIGURE D.2 – Panel a shows a three-dimensional rendering of liquid drops in turbulence: drops are visualized by the iso-countour $\phi = 0$ of the phase-field. The contour shows the turbulent kinetic energy, TKE=$(u'^2 + v'^2 + w'^2)/2$, in a mid-plane of the channel ($z = 0$). Panel b shows a close-up view of the rendering where the iso-level $\phi = 0$ is explicitly highlighted. In panel c-e, we show the effect of increasing the grid resolution (and thus the adoption of smaller the Cahn numbers) on the interface representation in the context of the phase-field method for different values of the refinement factor (panel c - $M = 1$; panel d - $M = 2$; panel d - $M = 4$). In particular, a coloured band identifies the region in which the phase-field method undergoes a transition between the values $\phi = \pm 0.9$. Clearly, increasing the grid resolution – thus decreasing the Cahn number, this band narrows around the dot-dashed line ($\phi = 0$) since the characteristic width of the thin transition layer is about $\simeq 4.1Ch$. For computational reasons, this layer has to be discretized with at least 3 grid points (using a pseudo-spectral method).

area in this high temporal resolution is possible thanks to the marching cubes algorithm described in section Sec. 1.6.2. All three simulations give qualitatively similar results. Starting from the flat and straight initial condition, the thin liquid layer is first stretched and deformed by the flow. This induces the initial increase of the value of the interfacial area $A(t)$, with the maximum of $A(t)$ at about $t^+ \simeq 30$. After this point, the thin liquid layer is stretched to the degree that it begins to break forming ligaments and drops (primary breakup). This induces a sharp decrease in the interface area $A(t)$. Later in time, when previously generated drops break up into smaller drops, the overall interfacial area increases again (at about $t^+ \simeq 400$). Finally, a statistically steady state is reached ($t^+ > 2000$, white area), during which breakup and coalescence of drops occur simultaneously, and dynamically balance each other. During this phase the interfacial area fluctuates around a constant mean value.

We can observe that the grid resolution employed for the solution of the Cahn-Hilliard

equation, and thus the value of the Cahn number that can be adopted, has an influence on the dynamics. In particular, from a vis-a-vis comparison between the profiles obtained for $G1$, $G2$ and $G4*$, we notice that the smaller is $Ch$, the larger the increase of area during the initial transient, and also the larger the increase of the area at steady-state. Indeed, thanks to the higher resolution (and the resulting smaller Cahn number that can be employed), higher deformations and finer/smaller drops and structures can be better described. It is also worth noticing that for the case $G4*$ (Ch=0.0075), the thickness of the thin transition layer, which in wall units can be estimated as $4.1ChRe_\tau$ is only slightly larger than the Kolmogorov length-scale evaluated at the channel centre, where most of the drops migrate ($\eta_k^+ = 3.45$ for the Reynolds number here considered).

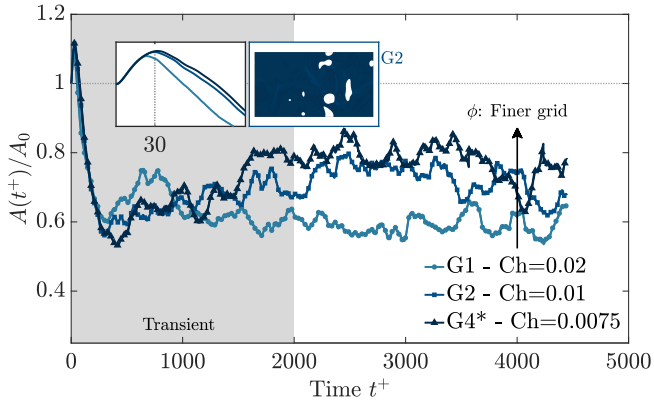


FIGURE D.3 – Evolution of total interfacial area $A(t^+)$, normalized by the initial area $A_0$. Results from the three simulations $G1$, $G2$ and $G4^*$ are shown using different colours, from light to dark blue. The grey area represents the initial transient, after which a statistically steady condition is reached.

The behaviour of the interfacial area described above reflects into a corresponding evolution of the number of drops, $N(t^+)$, shown in Fig. D.4. In particular, we notice an increase in the number of drops by decreasing the Cahn number. This is due to the fact that a finer grid allows for the description of smaller drops with respect to a coarser grid. In addition, $N(t^+)$ fluctuates remarkably, in particular after the end of the initial transient atomization (shaded area) and the statistically steady state is reached. These fluctuations of $N(t^+)$ can be traced back to the drop dynamics, which is characterized by the simultaneous occurrence of breakage and coalescence events (hence strongly modifying the number of drops present in the domain). Indeed, the number of drops is the result of the ultimate competition between breakage events (which increase the number of drops) and coalescence events (which reduce the number of drops). Following this idea, we can write a population balance equation for the number of drops in the channel [192, 193, 67, 194]:

$$\frac{dN(t^+)}{dt^+} = \dot{N}_b(t^+) - \dot{N}_c(t^+), \tag{D.1}$$

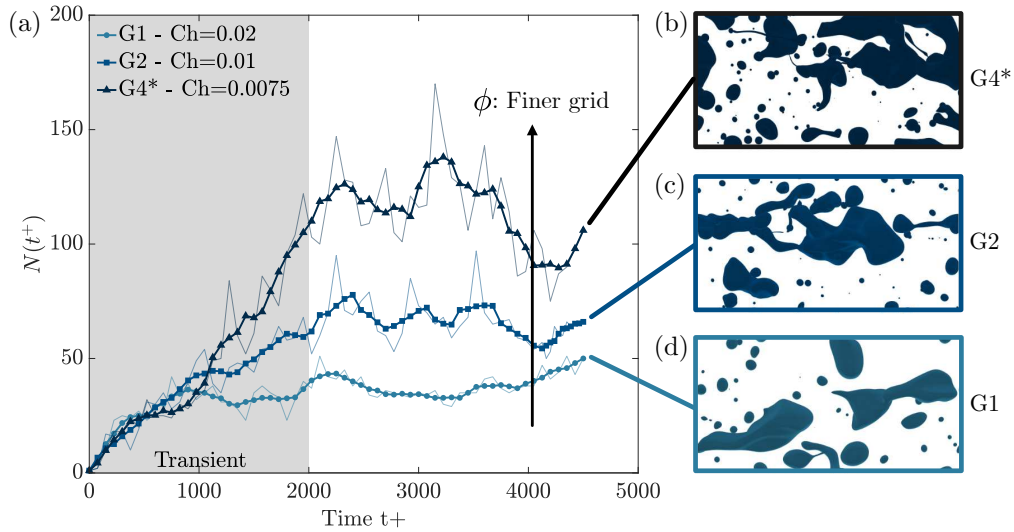


FIGURE D.4 – Time behaviour of the number of drops, $N(t^+)$, for the three simulations considered here, ($G1$, $G2$ and $G4^*$). The shaded area indicates the extension of the initial transient, after which a steady-state condition is reached ($t^+ > 2000$). Qualitative pictures (panels b-d), show a snapshot of the drops near the channel centre, at the end of the simulation ($t^+ = 4500$).

where $\dot{N}_b(t^+)$ and $\dot{N}_c(t^+)$ are the drops breakup and coalescence rates, which can be estimated by counting the number of breakup and coalescence events over a given time interval $\Delta t^+$. From the above equation, we can appreciate how the competition between two events determines the number of drops present in the channel. Likewise, the fluctuations of these two rates influence the time behaviour of the number of drops present in the channel. In addition, it must be also pointed out that the number of breakup and coalescence events (and thus the rates) depends on the number of drops $N(t^+)$ present at a certain time instant, in such a way that larger $dN(t^*)/dt^+$ are expected for larger $N(t^+)$ [96, 32].

A quantity of fundamental importance in the study of mass/momentum and heat exchanges in a drop-laden turbulent flow is the drop size distribution (DSD). The DSD provides a measure of the number of drops as a function of their characteristic size. As in the present case drops can undergo large deformations and obtain shapes of arbitrary morphology. In order to obtain a standard drop size classification measure, we consider the equivalent diameter as the characteristic size of each drop, defined as:

$$d_{eq}^+ = \left( \frac{6V_i^+}{\pi} \right)^{\frac{1}{3}}, \tag{D.2}$$

where $V_i^+$ is the dimensionless volume of the $i$-th drop expressed in wall-units. Compared to the overall number of drops presented above, the DSD provides a more insightful picture of the topology of the dispersed phase, as it evaluates more precisely the number of drops for each characteristic size. For instance, for a fixed volume fraction, a large number of small drops identify a larger surface-to-volume ratio, hence

maximizing the transport processes across their surface. A wide range of different drop diameters is expected as a consequence of coalescence (drop-drop interaction) and breakage (drop-turbulence interaction) events. In particular, the breakage of a drop is the result of the action of shear forces and turbulent fluctuations, which by stretching and elongating the drop can lead to its breakage once surface tension forces are not strong enough to restore the drop shape. By opposite, a coalescence event is observed when two drops come close to each other, and the small liquid film that separates the drops drains thus leading to the formation of a coalescence bridge.

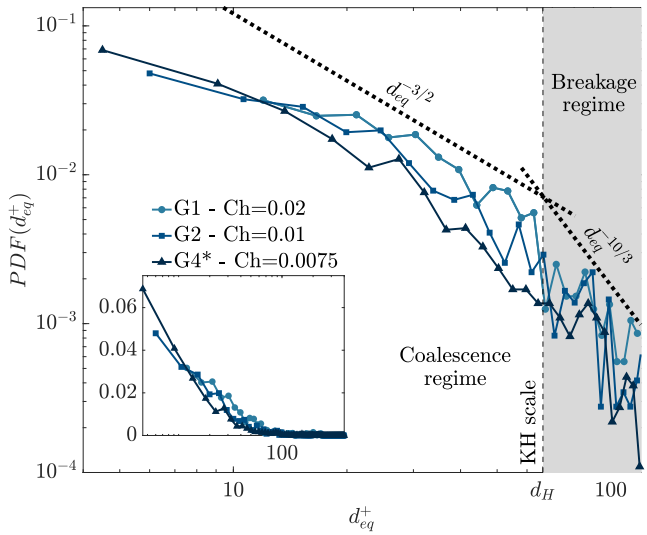


FIGURE D.5 – Drop size distribution (DSD) in log-log scale, for the three simulations $G1$ (light blue line and symbols), $G2$ (blue line and symbols) and $G4^*$ (dark blue line and symbols). The theoretical scalings, $d^{-3/2}$ and $d^{-10/3}$, for the coalesce-dominated and the breakage-dominated regimes are also reported with a dashed and dotted line, respectively. The Kolmogorov-Hinze scale, $d_H^+$, is indicated with a vertical dashed line. The inset shows the DSD in log-linear scale.

Considering the breakage, from a balance between stabilizing actions (surface tension forces) and destabilizing actions (shear forces and turbulent fluctuations), the maximum size of a drop that can be transported by turbulence without breaking, the Kolmogorov-Hinze diameter [195, 132], can be computed. For a turbulent channel flow configuration, the Kolmogorov-Hinze scale can be computed as follows [196, 197, 96]:

$$d_H^+ = 0.725 \left( \frac{We}{Re_\tau} \right)^{-3/5} |\epsilon_c|^{-2/5}, \tag{D.3}$$

where $\epsilon_c$ is the turbulent dissipation at the centre of the channel, where deformable drops migrate. The Kolmogorov-Hinze scale is not an exact threshold and should be taken more as a reference scale about which the dynamics of drops change behaviour (from surface tension to the inertia-dominated regime). Results of the DSD obtained by present simulations are shown in Fig. D.5. In particular, we compare the DSDs

– which are computed once the steady-state condition is attained ($t^+ > 2000$) – for the three different grid resolutions employed in this study. The value of the reference Kolmogorov-Hinze diameter, $d_H^+$, is explicitly indicated by the vertical dashed line. Also shown in Fig. D.5 are the theoretical behaviours proposed in the literature [198, 199, 200, 31]· In particular, Garrett et al. 200 proposed a power-law scaling for drops smaller than the Kolmogorov-Hinze scale (coalescence-dominated regime),

$$P(d^+) \propto d^{+-3/2}, \tag{D.4}$$

and a power-law scaling with a different exponent for drops larger than the Kolmogorov-Hinze scale (breakage-dominated regime):

$$P(d^+) \propto d^{+-10/3}. \tag{D.5}$$

Results are shown in Fig. D.5. We note that regardless of the grid resolution, all DSDs present a similar behaviour, characterized by a transition between the two theoretical scalings occurring around the Kolmogorov-Hinze diameter, $d_H^+$. The main effect of using a finer grid (in particular $G4^*$) is the presence of a larger number of smaller drops (with diameter equal to $\simeq 6$ wall units), given the better representation obtained for these drops.

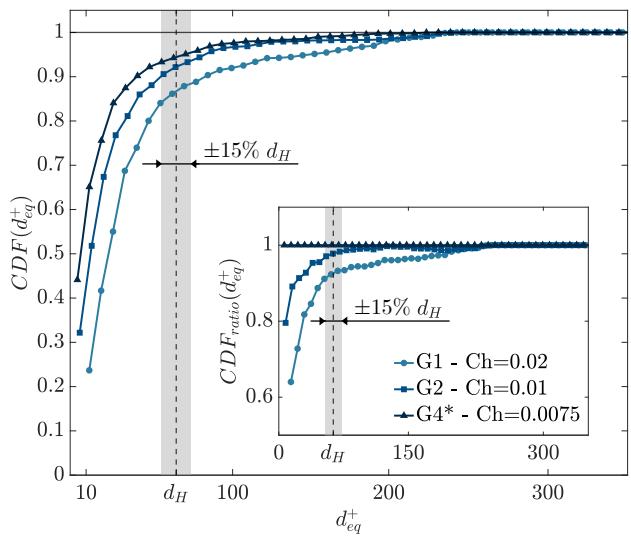


FIGURE D.6 – Cumulative distribution function (CDF) of the equivalent drop diameter, measured based on the DSD distribution of Fig. D.5. The ratio between the CDF measured for the different simulations, i.e. CDF($G1$)/CDF($G4^*$) and CDF($G2$)/CDF($G4*$) is shown in the inset. The grey area in the picture indicates drops diameter in the range $0.85d_H^+ < d_{eq}^+ < 1.15d_h^+$.

The preservation of the smaller drops with the grid refinement can also be qualitatively assessed by looking at the insets of Fig. D.4, which show the distribution of drops

at the channel centre for the different cases ($G1$, $G2$, $G4^*$), at the time instant ($t^+ = 4500$). The capability of finer grids ($G4^*$, Fig. D.4b) to capture small scales dynamics (see for example the formation of thin liquid bridges/ligaments) is clearly visible. We finally note that, based on current results, a simulation with $Ch = 0.01$ seems to nicely capture the drops dynamics at a reasonable computational cost, hence representing a convenient solution for most of the computations. The latter is also confirmed by looking at the cumulative distribution function (CDF) of the equivalent drop diameter, shown in Fig. D.6. The CDF is obtained by a progressive integration of the DSD starting from the smallest and reaching to the largest equivalent diameter. The range between $\pm 15\%$ of the Kolmogorov-Hinze scale is highlighted by the grey area. The results show that the two curves corresponding to simulations $G2$ with $Ch = 0.01$ and $G4^*$ with $Ch = 0.0075$ nearly overlap for diameters larger than the Kolmogorov-Hinze scale, indicating that the large drop dynamics are captured very well even at $Ch = 0.01$. The two curves diverge in the range of the smaller droplets, which is expected given that the thinner transition layer enables a more accurate representation of phenomena occurring at the smallest scales. Therefore, the large drop dynamics, which are significant in most engineering applications can be resolved with a satisfying level of accuracy while using a moderate resolution level, which is attainable at a reduced computational cost using the dual-grid approach.

# E

# Publications, courses and projects

## E.1 Referred journals

J1 **Giamagas G.**, Zonta F., Roccon, A. and Soldati, A. Propagation of capillary waves in two-layer oil–water turbulent flow, *J. Fluid Mech.*, 960, A5, 2023

J2 **Giamagas G.**, Zonta, F., Roccon, A. and Soldati, A.. Turbulence and interface waves in stratified oil-water channel flow at large viscosity ratio, *Flow Turbul. Combust.*, 2023.

J3 Schenk M., **Giamagas G.**, Roccon A., Zonta, F. and Soldati, A. Computationally efficient and interface accurate dual-grid phase-field simulation of turbulent drop-laden flows, *J. Fluids Eng.*, in preparation.

## E.2 Referred conferences

C1 **Giamagas G.**†, Zonta F., Roccon A. and Soldati A., Turbulent Poiseuille flow of two immiscible liquid layers inside a channel, *International Conference on Numerical Methods in Multiphase Flow (ICNNMF-4)*, Venice (IT), September 28-30, 2022.

C2 **Giamagas G.**, Zonta F.†, Roccon A. and Soldati A., Turbulent Poiseuille flow of two immiscible liquid layers inside a channel, *Direct and Large Eddy Simulation (DLES13)*, Udine (IT), October 26-28, 2022.

C3 **Giamagas G.**†, Zonta F., Roccon A. and Soldati A., Turbulent Poiseuille flow of two immiscible liquid layers inside a channel, *APS-DFD Annual Meeting*, Indianapolis (IN, USA), November 20-22, 2022.

C4 **Giamagas G.**†, Zonta F., Roccon A. and Soldati A., Interaction between capillary waves and hydrodynamic turbulence in a two-layer oil-water flow, *19th Multiphase Flow Conference and Short Course*, Dresden (DE), June 19-23, 2023.

C5 Schenk M.†, **Giamagas G.**, Zonta F. and Soldati A., A dual-grid approach for dispersed-flow simulations in turbulence, *Spanish Fluid Mechanics Conference*, Barcelona (ES), July 2-5, 2023.

C6 **Giamagas G.**, Zonta F.†., Roccon A. and Soldati A., Interaction between capillary waves and hydrodynamic turbulence in a two-layer oil-water flow, *18th European Turbulence Conference*, Valencia (ES), September 4-6, 2023.

C7 **Giamagas G.**, Zonta F.†, Roccon A. and Soldati A., Interaction between capillary waves and hydrodynamic turbulence in a two-layer oil-water flow, *10th GACM Colloquium on Computational Mechanics 2023*, Vienna (AT), September 10-13, 2023.

C8 **Giamagas G.**†, Zonta F., Roccon A. and Soldati A., Interaction between capillary waves and hydrodynamic turbulence in a two-layer oil-water flow, *THMT'23 - 10th International Symposium*, Rome (IT), September 11-15, 2023.

† Presentation speaker.

## E.3 Co-supervised projects

T1 "Viscosity stratification effects on thin-layer oil-water stratified turbulent channel flows" - Student: Maximilian Reiter (Batchelor thesis - TU Wien)

T2 "A multiple-resolution strategy for two-phase flow simulations using the Phase Field Method" - Student: Maximilian Schenk (Master thesis - TU Wien)

T3 "Energetics of two-layer oil-water flow - numerical analysis" - Student: Francesco Chirico (Master thesis - University of Pisa/ TU Wien)

T4 "Numerical simulation of non-newtonian turbulent channel flow" - Student: Emanuele Milocco (Master thesis - University of Udine/ TU Wien)

## E.4 HPC projects

P1 **Interfacial capillary WAve growth and breakup characterisation in a two-layer turbulent channel FLOw - WAFLO**, Project ID: ISCRA B HP10BBOP14, 1 mln CPU Hours, MARCONI-100 (Tier 0), CINECA Supercomputing Centre, Bologna (IT), 2021.

P2 **Validation of phase-field based method for INterface decription of a two-layer turbulent channel FLOw - INFLO**, Project ID: ISCRA C HP10CJSA91, CINECA Supercomputing Centre, MARCONI-100 (Tier 0), Bologna (IT), 2020.

P3 **Growth and Spectra of CApillaRy wAVEs in viscosity stratified turbuLence - CARAVEL**, Project ID: EHPC-REG-2022R01-020, 24 mln CPU Hours, LUMI-C (Tier 0), Finnish IT centre for science, Kajaani (FI), 2021.

## E.5 Advanced courses

A1 **Introduction to Working on the VSC Clusters***, Vienna Scientific Cluster (VSC), Vienna (Austria), January 14, 2021.

A2 **Introduction to High Performance Computing with OpenMp and MPI***, University Of Lubliana, Lubliana (Slovenia), February 1-4, 2021. Coordinated by: Prof. L. Kos

A3 **High Performance Computing Course On Handling Of Data And I/O Processes**†, Maison De La Simulation, Paris (France), March1-2, 2021.

A4 **Heterogeneous Programming on GPUs with MPI & OmpSs***, Barcelona Scientific Center, Barcelona (Spain), March 8-12, 2021.

A5 **Advanced Parallel Programming***, CSC – IT Center for Science, Helsinki (Finland), March 10-12, 2021.

A6 **From Lagrangian Chaos To Turbulence In Dilute Polymer Solution***, Basque Center For Applied Mathematics, Bilbao (Spain), March 15-26, 2021. Coordinated by: Prof. I. Fouxon

A7 **GPU Programming Course***, Julich Supercomputing Center, Aachen (Germany), April 26-30, 2021.

A8 **Parallel I/O***, Vienna Scientific Cluster (VSC), Vienna (Austria), May 18-19, 2021.

A9 **Uncertainty Quantification***, Maison De La Simulation, Paris (France), May 10-12, 2021.

A10 **Introduction To Quantum Computing***, CINECA HPC Center, Bologna (Italy), June 21-25, 2021. Coordinated by: Dr. D. Ottaviani

A11 **Physics of Granular Suspensions: Micro-Mechanics of Geophysical Flows***, International Centre for Mechanical Sciences (CISM), Udine (Italy), July 14-18, 2021. Coordinated by: Prof. M. Mazzuoli and Prof. L. Lacaze

A12 **MPI-OpenMP Advanced Programming***, HLRS, Stuttgart (Germany), October 11-15, 2021. Coordinated by: Dr. Rolf Rabenseifner and Prof. Rainer Keller

A13 **Virtual School on Numerical Methods for Parallel CFD***, CINECA HPC Center, Bologna (Italy), December 13-27, 2021. Coordinated by: Dr. G. Amati

A14 **Complex Flows and Complex Fluids**, International Centre for Mechanical Sciences (CISM), Udine (Italy), April 4-8, 2022. Coordinated by: Prof. F. Toschi

A15 **Sports Physics and Technology**, International Centre for Mechanical Sciences (CISM), Udine (Italy), September 19-23, 2022. Coordinated by: Prof. C. Clanet and Prof. A. Hosoi

A16 **Liquid Interfaces, Drops and Sprays**, International Centre for Mechanical Sciences (CISM), Udine (Italy), June 26-30, 2023. Coordinated by: Prof. A. Amirfazli, Prof. V. Bertola and Prof. M. Marengo

* Online course.

# Acknowledgments

I would like to express my gratitude to my supervisors, Prof Cristian Marchioli, Dr Francesco Zonta, and Prof Alfredo Soldati, for providing me with the opportunity to work in an excellent and dynamic scientific environment at both the University of Udine and the Technische Universität Wien. Their guidance and motivation were essential throughout the whole time of my PhD studies. I am also grateful to Dr Alessio Roccon for his assistance in the early stages of my research and for always being willing to provide his support when needed. I would like to thank Prof Guillaume Ducrozet and Prof Luc Deike, who took the time to carefully review my thesis. Their observations and feedback have been greatly appreciated and have helped to improve the quality of my work. Moreover, I feel fortunate to have had the chance to collaborate with many fellow students and especially Max Schenk, Emanuele Milocco, Francesco Chirico, Maximilian Reiter and Charlotte Gottschalk. A special thanks goes to all the colleagues both in Udine and in Vienna and to the kindest of secretaries, Kathi and Christina, for contributing to a positive working atmosphere. Finally, I want to thank my family for always being there for me. I dedicate this work to Eunjilee for all that we shared together.

# Bibliography


[1] Joseph D. D., Renardy M. and Renardy, Y. Instability of the flow of two immiscible liquids with different viscosities in a pipe. *J. Fluid Mech.*, 141, 309–317, 1984.

[2] Hu H. H., Lundgren T. S. and Joseph D. D. Stability of core-annular flow with a small viscosity ratio. *Phys. Fluids*, 2(11), 1945–1954, 1990.

[3] Joseph D. D., Bai R., Chen K. P. and Renardy Y. Y. Core-Annular Flows. *Annu. Rev. Fluid Mech.*, 29(1), 65–90, 1997.

[4] Roccon A., Zonta F., and Soldati A. Turbulent drag reduction by compliant lubricating layer. *J. Fluid Mech.*, 863, 447-464, 2019

[5] Al Wahaibi T. and Angeli P. Experimental study on interfacial waves in stratified horizontal oil-water flow. *Int. J. Multiph. Flow*, 37, 930–940, 2011.

[6] Barral A. and Angeli P. Interfacial characteristics of stratified liquid-liquid flows using a conductance probe. *Exp. Fluids*, 54, 2013.

[7] De Castro M.S. and Rodriguez O. M. H. Interfacial waves in stratified viscous oil-water flow. *Exp. Therm. Fluid Sci.*, 62, 85–98, 2015.

[8] Sotgia G.,Tartarini P. and Stalio E. Experimental analysis of flow regimes and pressure drop reduction in oil-water mixtures. *Int. J. Multiph. Flow*, 34(12), 1161–1174, 2008.

[9] Thais L. and Magnaudet J. Turbulent structure beneath surface gravity waves sheared by the wind. *J. Fluid Mech.*, 328, 313–344, 1996.

[10] Falcon E., Laroche C. and Fauve S. Observation of Gravity-Capillary Wave Turbulence. *Phys. Rev. Lett.*, 98, 094503, 2007.

[11] Düring G. and Falcon C. Symmetry Induced Four-Wave Capillary Wave Turbulence. *Phys. Rev. Lett.*, 103(17):174503, 2009.

[12] Berhanu M. and Falcon E. Space-time-resolved capillary wave turbulence. *Phys. Rev. E.*, 87, 033003, 2013.

[13] Aubourg Q. and Mordant N. Investigation of resonances in gravity-capillary wave turbulence. *Phys. Rev. Fluids*, 1, (2), 023701, 2016.

[14] Issenmann B., Laroche C. and Falcon E. Wave turbulence in a two-layer fluid: Coupling between free surface and interface waves. *Europhys. Lett.*, 116, 64005, 2015.

[15] Issa R.I. Prediction of turbulent, stratified, two-phase flow in inclined pipes and channels. *Int. J. Multiph. Flow*, 14(2), 141–154, 1988.

[16] Al-Yaari M. and Sharkh A. CFD Prediction of stratified oil-water flow in a horizontal pipe. *Eng. Trans.*, 01(05), 2011.

[17] Burlutskii E. CFD study of oil-in-water two-phase flow in horizontal and vertical pipes. *J. Pet. Eng.*, 162, 524–531, 2018.

[18] Pouraria H., Park K. H. and Seo Y. Numerical Modelling of Dispersed Water in Oil Flows Using Eulerian-Eulerian Approach and Population Balance Model. *Processes*, 9, 1345, 2021.

[19] Gao H., Gu H. Y. and Guo L. J. Numerical study of stratified oil-water two-phase turbulent flow in a horizontal tube. *Int. J. Heat Mass Transf.*, 46(4), 749–754, 2003.

[20] Hohne T., Rayya A., Montoya G. Numerical Modelling of Horizontal Oil-Water Pipe Flow. *Energies*, 13(19), 5042, 2020.

[21] Kjolaas J., Schumann H., Gonzalez D. and Johansen S. T. Modelling of dispersed oil/water flow in a near-horizontal pipe. *Chem. Eng. Sci.*, 263, 118074, 2022.

[22] Pushkarev A. and Zakharov V. Turbulence of capillary waves. *Phys. Rev. Lett.*, 76, 3320–3323, 1996.

[23] Pan Y. and Yue D. K. P. Direct numerical investigation of turbulence of capillary waves. *Phys. Rev. Lett.*, 113, 094501, 2014.

[24] Deike L., Fuster D., Berhanu M. and Falcon E. Direct Numerical Simulations of Capillary Wave Turbulence. *Phys. Rev. Lett.*, 112, 234501, 2014.

[25] Lin M. Y., Moeng C. H., Tsai W. T., Sullivan P. P. and Belcher S. E. Direct numerical simulation of wind-wave generation processes *J. Fluid Mech.*, 616, 1–30, 2008.

[26] Guo X. and Shen L. Interaction of a deformable free surface with statistically steady homogeneous turbulence. *J. Fluid Mech.*, 658, 33–62, 2010.

[27] Zonta F., Soldati A. and Onorato M. Growth and spectra of gravity-capillary waves in countercurrent air/water turbulent flow. *J. Fluid Mech.*, 777, 245-259, 2015.

[28] Li T. and Shen L. The principal stage in wind-wave generation. *J. Fluid Mech.*, 934, A41, 2022

[29] Wu J, Popinet S, Deike L. Revisiting wind wave growth with fully coupled direct numerical simulations. *J. Fluid Mech.*, 951, A18, 2022.

[30] Ahmadi S., Roccon A., Zonta F. and Soldati, A. Turbulent drag reduction by a near wall surface tension active interface. *Flow. Turbul. Combust.*, 100, 1–15, 2018.

[31] Soligo G., Roccon A. and Soldati A. Turbulent Flows With Drops and Bubbles: What Numerical Simulations Can Tell Us—Freeman Scholar Lecture. *ASME. J. Fluids Eng.*, 143(8): 080801, 2021.

[32] Mangani F., Soligo G., Roccon A. and Soldati A. Influence of density and viscosity on deformation, breakage, and coalescence of bubbles in turbulence. *Phys. Rev. Fluids*, 7, 053601, 2022.

[33] Elghobashi S. Direct Numerical Simulation of Turbulent Flows Laden with Droplets or Bubbles. *Annu. Rev. Fluid Mech.*, 51, 1, 217-244, 2019.

[34] Zonta F., Marchioli C. and Soldati, A. Modulation of turbulence in forced convection by temperature-dependent viscosity. *J. Fluid Mech.*, 697:150-174, 2012.

[35] Scarbolo L., Bianco F. and Soldati A. Coalescence and breakup of large droplets in turbulent channel flow. *Phys. Fluids*, 27, 073302, 10.1063/1.4923424, 2015.

[36] Hirt C. and Nichols B. Volume of fluid (VOF) method for the dynamics of free boundaries. *J. Comput. Phys.*, 39(1), 201–225, 1981.

[37] Osher S. and Sethian J. A Level Set Approach for computing solutions to incompressible Two-Phase Flow. *J. Comput. Phys.*, 114, 12–49, 1994.

[38] Tryggvason G., Bunner B., Esmaeeli A., Juric D., Tauber W., Han J., Nas S. and Jan Y. A front-tracking method for the computations of multiphase flow. *J. Comput. Phys.*, 175, 708–759, 2001.

[39] Cahn J.W. and Hilliard J.E. Free Energy of a Nonuniform System. i. Interfacial Free Energy. *J. Chem. Phys.*, 28:258–267, 1958.

[40] J.W. Cahn and J.E. Hilliard. Free energy of a nonuniform system. ii. thermodynamic basis. *J. Chem. Phys*, 30(5):1121–1124, 1959.

[41] Cahn J.W. and Hilliard J.E. Free energy of a nonuniform system. iii. nucleation in a two-component incompressible fluid. *J. Chem. Phys.*, 31:688, 1959.

[42] Anderson D.M., McFadden G.B. and Wheeler A.A. Diffuse interface methods in fluid mechanics. *Annu. Rev. Fluid Mech.*, 30(1):139–165, 1998.

[43] Jacqmin D. Calculation of Two-Phase Navier-Stokes Flows Using Phase-Field Modeling. *J. Comput. Phys.*, 155, 1, 96-127, 1999.

[44] Badalassi V.E., Ceniceros H.D. and Banerjee S. Computation of multiphase systems with phase field models. *J. Comput. Phys.*, 190(2):371–397, 2003.

[45] Kim J. A continuous surface tension force formulation for diffuse-interface models. *J. Comput. Phys.*, 204, 784-804, 2005.

[46] Prosperetti A. and Tryggvason G. Computational Methods for Multiphase Flow. *Cambridge University Press*, 2009.

[47] Roccon A., Zonta F. and Soldati A. Phase-field modeling of complex interface dynamics in drop-laden turbulence. *Phys. Rev. Fluids*, 8, 2023.

[48] Lamorgese A.G., Molin D. and Mauri R. Phase field approach to multiphase flow modeling. *Milan J. Math.*, 79(2):597–642, 2011.

[49] Ding H. and Yuan C.J. On the diffuse interface method using a dual-resolution cartesian grid. *J. Comput. Phys.*, 273:243–254, 2014.

[50] Yue P., Zhou C. and Feng J. Spontaneous shrinkage of drops and mass conservation in phase-field simulations. *J. Comput. Phys.*, 223(1), 1–9, 2007.

[51] Wang Y., Shu C., Shao J. Y. and Wu, J. A mass-conserved diffuse interface method and its application for incompressible multiphase flows with large density ratio. *J. Comput. Phys.*, 290, 2015.

[52] Soligo G., Roccon A. and Soldati A. Mass-conservation-improved phase field methods for turbulent multiphase flow simulation, *Acta Mech.*, 230, 2019.

[53] Van Der Waals J. D. The thermodynamic theory of capillarity under the hypothesis of a continuous variation of density. *J. Stat. Phys.*, 20, 200, 1979.

[54] Ding H., Spelt P.D.M. and Shu C. Diffuse interface model for incompressible two-phase flows with large density ratios. *J. Comput. Phys.*, 226(2):2078–2095, 2007.

[55] Korteweg D.J. Sur la forme que prennent les equations du mouvements des fluides si l'on tient compte des forces capillaires causées par des variations de densité considérables mais continues et sur la théorie de la capillarité dans l'hypothèse d'une variation continue de la densité. *Arch. Neerl. Sci. Exact. Nat.*, 6, 1–24, 1901.

[56] Pope S. Turbulent Flows. *Cambridge University Press*, 2000.

[57] Yue P., Zhou C. and Feng J.J. Sharp-interface limit of the Cahn–Hilliard model for moving contact lines. *J. Fluid Mech.*, 645, 279, 2010.

[58] Magaletti F., Picano F., Chinappi M., Marino L. and Casciola C.M. The sharp-interface limit of the Cahn–Hilliard/Navier–Stokes model for binary fluids. *J. Fluid Mech.*, 714, 95–126, 2013.

[59] Kim J., Moin P. and Moser R. Turbulence statistics in fully developed channel flow at low Reynolds number. *J. Fluid Mech.*, 177, 133–166, 1987.

[60] *Speziale C. G.* On the advantages of the vorticity-velocity formulation of the equations of fluid dynamics. *J. Comput. Phys.*, 73(2), 476-480, 1987.

[61] Yue P., Feng J., Liu C. and Shen J. A diffuse-interface method for simulating two-phase flows of complex fluids. *J. Fluid Mech.*, 515, 293-317, 2004

[62] Ascher U. M., Ruuth S. J. and Spiteri R. J. Implicit-explicit Runge-Kutta methods for time-dependent partial differential equations. *Appl. Numer. Math* ., 25, 2, 151-167, 1997.

[63] Canuto C., Hussaini M.Y., Quarteroni A.M. and Zang T.A. Spectral Methods in Fluid Dynamics. *Springer-Verlag*, 1959.

[64] Tryggvason G., Thomas J., Lu S. and Aboulhasanzadeh B. Multiscale issues in DNS of multiphase flows. *Acta Math. Sci.*, 30B(2), 551–562, 2010.

[65] Thomas S., Esmaeeli A. and Tryggvason G. Multiscale computations of thin films in multiphase flows. *Int. J. Multiph. Flow*, 36, 71–77, 2010.

[66] Dodd M. S. and Ferrante A, On the interaction of Taylor length scale size droplets and isotropic turbulence. *J. Fluid Mech.*, 806, 356–412, 2016.

[67] Soligo G., Roccon A. and Soldati A. Breakage, coalescence and size distribution of surfactant-laden droplets in turbulent flow. *J. Fluid Mech.*, 881, 244-282, 2019.

[68] Berger M. J. and Oliger J. Adaptive mesh refinement for hyperbolic partial differential equations. *J. Comput. Phys.*, 53(3), 484–512, 1984.

[69] Berger M. J. and Colella P. Local adaptive mesh refinement for shock hydrodynamics. *J. Comput. Phys.*, 82(1), 64–84, 1989.

[70] Popinet S. Gerris: a tree-based adaptive solver for the incompressible Euler equations in complex geometries. *J. Comput. Phys.*, 190(2), 572–600, 2003.

[71] Greaves D. A quadtree adaptive method for simulating fluid flows with moving interfaces. *J. Comput. Phys.*, 194(1), 35–56, 2004.

[72] Fuster D., Bagué A., Boeck T., Le Moyne L., Leboissetier A., S. Popinet, Ray P., Scardovelli R. and Zaleski S. Simulation of primary atomization with an octree adaptive mesh refinement and VOF method. *Int. J. Multiph. Flow*, 35(6), 550–565, 2009.

[73] Laurmaa V., Picasso M. and Steiner G. An octree-based adaptive semi-Lagrangian VOF approach for simulating the displacement of free surfaces. *Comput. Fluids*, 131, 190–204, 2016.

[74] Sussman M., Almgren A. S., Bell J. B., Colella P., Howell L. H. and Welcome M. L. An adaptive level set approach for incompressible two-phase flows. *J. Comput. Phys.*, 148(1), 81–124, 1999.

[75] Strain J. Tree methods for moving interfaces. *J. Comput. Phys.*, 151(2), 616–648, 1999.

[76] Losasso F., Gibou F. and Fedkiw R. Simulating water and smoke with an octree data structure. *ACM Trans. Graph.*, 457–462, 2004.

[77] Losasso F., Fedkiw R., and Osher S. Spatially adaptive techniques for level set methods and incompressible flow. *Comput. Fluids*, 35(10), 995–1010, 2006.

[78] Herrmann M., A balanced force refined level set grid method for two-phase flows on unstructured flow solver grids. *J. Comput. Phys.*, 227(4), 2674–2706, 2008.

[79] Mirzadeh M., Guittet A., Burstedde C. and Gibou F. Parallel level-set methods on adaptive tree-based grids. *J. Comput. Phys.*, 322, 345–364, 2016.

[80] Gibou F., Fedkiw R. and Osher S. A review of level-set methods and some recent applications. *J. Comput. Phys.*, 353, 82–109, 2018.

[81] Fakhari A., Bolster D. and Luo L. S. A weighted multiple-relaxation-time lattice Boltzmann method for multiphase flows and its application to partial coalescence cascades. *J. Comput. Phys.*, 341, 22–43, 2017.

[82] Watanabe S. and Aoki T. Large-scale flow simulations using lattice Boltzmann method with AMR following free-surface on multiple GPUs. *Comput. Phys. Commun.*, 264, 107871, 2021.

[83] Ceniceros H. D., Nos R. L., and Roma A. M. Three-dimensional, fully adaptive simulations of phase-field fluid models. *J. Comput. Phys.*, 229(17), 6135–6155, 2010.

[84] Khanwale M. A., Lofquist A. D., Sundar H., Rossmanith J. A. and Ganapathysubramanian B. Simulating two-phase flows with thermodynamically consistent energy stable Cahn-Hilliard Navier-Stokes equations on parallel adaptive octree based meshes. *J. Comput. Phys.*, 419, 109674, 2020.

[85] Ostilla-Monico R., Yang Y., Van Der Poel E., Lohse D. and Verzicco R. A multiple-resolution strategy for Direct Numerical Simulation of scalar turbulence. *J. Comput. Phys.*, 301, 321, 2015.

[86] Liu H. R., Ng C. S., Chong K. L., Lohse D. and Verzicco R. An efficient phase-field method for turbulent multiphase flows. *J. Comput. Phys.*, 446, 110659, 2021.

[87] Bazesefidpar K., Brandt L. and Tammisola O. A dual resolution phase-field solver for wetting of viscoelastic droplets. *Int. J. Numer. Methods Fluids*, 94, 1541, 2022.

[88] Feng W., Yu P., Hu S., Liu Z. K., Du Q. and Chen L. Q. Spectral implementation of an adaptive moving mesh method for phase-field equations. *J. Comput. Phys.*, 220(1), 498–510, 2006.

[89] Burstedde C., Wilcox L. C. and Ghattas O. p4est: Scalable algorithms for parallel adaptive mesh refinement on forests of octrees. *SIAM J. Sci. Comput.*, 33(3), 1103–1133, 2011.

[90] Giamagas G., Zonta F., Roccon A. and Soldati A. Propagation of capillary waves in two-layer oil–water turbulent flow. *J. Fluid Mech.*, 960, 5, 2023.

[91] Giamagas G., Zonta F., Roccon A. and Soldati A. Turbulence and Interface Waves in Stratified Oil–Water Channel Flow at Large Viscosity Ratio. *Flow Turbul. Combust.*, 2023

[92] Lorensen W. and Cline H. Marching Cubes: A High Resolution 3D Surface Construction Algorithm. *Comput. Graph.*, 21(4):163-178, 1987.

[93] Schenk M., Giamagas G., Roccon A., Zonta F. and Soldati A. Assessing grid size resolution for reliable simulations of turbulent dispersed flows via phase-field method and dual-grid approach. *J. Fluids Eng.*, (in preparation)

[94] Andreussi P. and Soldati A. Fluidodinamica di processo. Elementi di teoria ed eserciz. *Forum Editrice*, 2001

[95] Pecnik R. and Patel A. Scaling and modelling of turbulence in variable property channel flows. *J. Fluid Mech.*, 823, R1, 2017.

[96] Soligo G., Roccon A. and Soldati A. Coalescence of surfactant-laden drops by Phase Field Method. *J. Comput. Phys.*, 376, 2019.

[97] Taylor G.I. The viscosity of a fluid containing small drops of another fluid. *Proc. R. Soc. Lond.*, 138(834), 41–48, 1932.

[98] Taylor G.I. The formation of emulsions in definable fields of flow. *Proc. R. Soc. Lond.*, 146(858), 501–523, 1934.

[99] Shapira M. and Haber S. Low Reynolds number motion of a droplet in shear flow including wall effects. *Int. J. Multiph. Flow*, 16(2), 305–321, 1990.

[100] Zhou H. and Pozrikidis C. The flow of suspensions in channels: single files of drops. *Phys. Fluids*, 5(2), 311–324, 1993.

[101] Tang H., Wrobel L. and Fan Z. Tracking of immiscible interfaces in multiple-material mixing processes. *Comput. Mater. Sci.*, 29(1), 103–118, 2004.

[102] Soligo G., Roccon A. and Soldati A. Deformation of clean and surfactant-laden droplets in shear flow. *Meccanica*, 55, 371–386, 2020.

[103] Barmak I., Gelfgat A., Ullmann A., Brauner N. and Vitoshkin, H. Stability of stratified two-phase flows in horizontal channels. *Phys. Fluids*, 28, 044101, 2016.

[104] Barmak I., Gelfgat A., Ullmann A. and Brauner N. Non-modal stability analysis of stratified two-phase channel flows. *Int. J. Multiph. Flow*, 111, 122-139, 2019.

[105] Conan C., Masbernat O., Decarre S. and Line, A. Local hydrodynamics in a dispersed-stratified liquid-liquid pipe flow. *AIChE Journal*, 53(11), 2754–2768, 2007.

[106] Morgan R., Markides C. N., Zadrazil I. and Hewitt, G. Characteristics of horizontal liquid-liquid flows in a circular pipe using simultaneous high-speed laser-induced fluorescence and particle velocimetry. *Int. J. Multiph. Flow*, 49, 99–118, 2013.

[107] Ayati A.A., Kolaas J., Jensen A. and Johnson G.W. A PIV investigation of stratified gas–liquid flow in a horizontal pipe. *Int. J. Multiph. Flow*, 61, 129-143, 2014.

[108] Ayati A.A., Kolaas J., Jensen A. and Johnson G.W. Combined simultaneous two-phase PIV and interface elevation measurements in stratified gas/liquid pipe flow. *Int. J. Multiph. Flow*, 74, 45-58, 2015.

[109] Ayati A.A., Kolaas J., Jensen A. and Johnson, G.W. The effect of interfacial waves on the turbulence structure of stratified air/water pipe flow. *Int. J. Multiph. Flow*, 78, 104-116, 2016.

[110] Zadrazil I. and Markides C.N. An experimental characterization of liquid films in downwards co-current gas–liquid annular flow by particle image and tracking velocimetry. *Int. J. Multiph. Flow*, 67, 42-53, 2014.

[111] Ibarra R., Zadrazil I., Matar O.K. and Markides C.N. Dynamics of liquid–liquid flows in horizontal pipes using simultaneous two–line planar laser–induced fluorescence and particle velocimetry. *Int. J. Multiph. Flow*, 101, 47-63, 2018.

[112] Ibarra R., Matar O.K. and Markides C.N. Experimental investigations of upward-inclined stratified oil-water flows using simultaneous two-line planar laser-induced fluorescence and particle velocimetry. *Int. J. Multiph. Flow*, 135, 103502, 2021.

[113] Popinet S. Numerical Models of Surface Tension. *Annu. Rev. Fluid Mech.*, 50(1), 49–75, 2018.

[114] Xie F., Zheng X., Triantafyllou M., Constantinides Y., Zheng Y. and Karniadakis, G. Direct Numerical Simulations of Two-Phase Flow in an Inclined Pipe. *J. Fluid Mech.*, 825, 189–207, 2017.

[115] Kim K. and Choi H. Direct numerical simulation of a turbulent core-annular flow with water-lubricated high viscosity oil in a vertical pipe. *J. Fluid Mech.*, 849, 419–447, 2018.

[116] Roccon A., Zonta F., and Soldati A. Energy balance in lubricated drag-reduced turbulent channel flow. *J. Fluid Mech.*, 911, A37, 2021.

[117] Zakharov V. E. and Filonenko N. N. Weak turbulence of capillary waves. *J. Appl. Mech. Tech. Phys.*, 8, 37-40, 1967.

[118] Zakharov V. E., L'vov V. S. and Falkovich G. Kolmogorov Spectra of Turbulence I: Wave Turbulence. *Springer-Verlag*, 1992.

[119] Newell A. C. and Rumpf, B. Wave Turbulence. *Annu. Rev. Fluid Mech.*, 43(1), 59–78, 2011.

[120] Falcon E. and Mordant N. Experiments in Surface Gravity-Capillary Wave Turbulence. *Annu. Rev. Fluid Mech.*, 54, 1-25, 2022.

[121] Higgins M.S. L. The generation of capillary waves by steep gravity waves. *J. Fluid Mech.*, 16(1), 138–159, 1963.

[122] Phillips O.M. The dynamics of the upper ocean. In *Cambridge University Press*, 1977.

[123] Berhanu M., Falcon E., Michel G., Gissinger C. and Fauve S. Capillary wave turbulence experiments in microgravity. *Europhys. Lett.*, 128(3):34001, 2019.

[124] Iwamoto K., Suzuki Y. and Kasagi N. Reynolds number effect on wall turbulence: toward effective feedback control. *Int. J. Heat Fluid Flow*, 23, 678-689, 2002.

[125] G. G. Stokes. On the Theory of Oscillatory Waves. Trans. Cambridge Philos. Soc., 8, 441-455, 1847.

[126] Monin A., and Yaglom A. Statistical Fluid Mechanics, Volume II: Mechanics of Turbulence. *MIT Press, Cambridge, MA*, 2007.

[127] Balkovsky E., Falkovich G., Lebedev V. and Shapiro I. Y. Large-scale properties of wave turbulence. *Phys. Rev. E.*, 52, 4, 4537-4540, 1995.

[128] Michel G., Pétrélis F. and Fauve S. Observation of Thermal Equilibrium in Capillary Wave Turbulence. *Phys. Rev. Lett.*, 118, 144502, 2017.

[129] Savelsberg R. and Van De Water W. Turbulence of a Free Surface. *Phys. Rev. Lett.*, 100, 034501, 2008.

[130] Deike, L., Berhanu M. and Falcon E. Decay of capillary wave turbulence. *Phys. Rev. E.*, 85, 2015.

[131] Kolmogorov A. N. On the breakage of drops in a turbulent flow. *Dokl. Akad. Nauk SSSR*, 66, 1-25, 1949.

[132] Hinze J. O. Fundamentals of the hydrodynamic mechanism of splitting in dispersion processes. *AIChE Journal*, 1, 289-295, 1955.

[133] Phillips O. On the generation of waves by turbulent wind. *J. Fluid Mech.*, 2, (5), 417–445, 1957.

[134] Miles, J.W. On the generation of surface waves by shear flows. *J. Fluid Mech.*, 3, (2), 185-204, 1957

[135] Belcher, S.E. and Hunt, J.C.R. Turbulent shear flow over slowly moving waves. *J. Fluid Mech.*, 251, 109-148

[136] Hoepffner J., Blumenthal R. and Zaleski S. Self-Similar Wave Produced by Local Perturbation of the Kelvin-Helmholtz Shear-Layer Instability. *Phys. Rev. Lett.*, 106, 104502, 2011.

[137] Lamb H. Hydrodynamics. *Springer-Verlag*, 1932.

[138] Crapper G. D. An exact solution for progressive capillary waves of arbitrary amplitude. *J. Fluid Mech.*, 2, 532-540, 1957.

[139] Kumar K. and Tuckerman L. S. Parametric instability of the interface between two fluids. *J. Fluid Mech.*, 279:49-68, 1994.

[140] Nazarenko S. Wave turbulence. *Springer-Verlag*, 2011.

[141] Miquel B. and Mordant N. Nonlinear dynamics of flexural wave turbulence. *Phys. Rev. E.*, 84(6), 2011.

[142] Ricco P., Ottonelli C., Hasegawa Y. and Quadrio M. Changes in turbulent dissipation in a channel flow with oscillating walls. *J. Fluid Mech.*, 700, 77–104, 2012.

[143] Gatti D., Cimarelli A., Hasegawa Y., Frohnapfel B. and Quadrio M. Global energy fluxes in turbulent channels with flow control. *J. Fluid Mech.*, 857, 345–373, 2018.

[144] Rosti M. E., Ge Z., Jain S. S., Dodd M. S. and Brandt L. Droplets in homogeneous shear turbulence. *J. Fluid Mech.*, 876, 962–984, 2019.

[145] Reynolds O. On the Dynamical Theory of Incompressible Viscous Fluids and the Determination of the Criterion. *Philosophical Transactions of the Royal Society of London*, 186, 123-164, 1895.

[146] Monin A., and Yaglom A. Statistical Fluid Mechanics, Volume I: Mechanics of Turbulence. *MIT Press, Cambridge, MA*, 2007.

[147] Mansour N. N., Kim J., and Moin P. Reynolds-stress and dissipation-rate budgets in a turbulent channel flow, *J. Fluid Mech.*, 194, 15–44, 1988.

[148] Li Z. and Jaberi F. Turbulence-interface interactions in a two-fluid homogeneous flow. *Phys of Fluids*, 21, 2009.

[149] Joseph D. D., Stability of fluid motions II. *Springer Tracts Nat. Philos.*, 28, 1976.

[150] Deike L., Berhanu M. and Falcon, E. Energy flux measurement from the dissipated energy in capillary wave turbulence. *Phys. Rev. E.*, 89(2), 023003, 2014.

[151] Stewart R. H. Introduction to physical oceanography. *Am. J. Phys.*, 2008.

[152] Shannon C. E. Communication in the Presence of Noise. *Proceedings of the IRE*, 37, 10-21, 1949.

[153] Craik, A. D.D. The origins of water wave theory. *Annu. Rev. Fluid Mech.*, 36(1), 1-28, 2004.

[154] Berhanu M., Falcon E. and Deike, L. Turbulence of capillary waves forced by steep gravity waves. *J. Fluid Mech.*, 850, 803–843, 2018.

[155] Miles J. W Surface-wave damping in closed basins. *Proc. R. Soc. Lond.*, 297, 459-475, 1967.

[156] Preziosi L., Chen K. and Joseph D. D. Lubricated pipelining: stability of core-annular flow. *J. Fluid Mech.*, 201, 323–356, 1989.

[157] Joseph D. D., Bai R., Chen K. and Renardy, Y. Core-annular flows. *Annu. Rev. Fluid Mech.*, 29, 65–90, 2003.

[158] Huang A. and Joseph D.D. Stability of eccentric core–annular flow. *J. Fluid Mech.*, 282, 233–245, 1995.

[159] Kujawinski E.B., Kido Soule M.C., Valentine D.L., Boysen A.K., Longnecker K. and Redmond, M.C. Fate of dispersants associated with the deepwater horizon oil spill. *Environ. Sci. Technol.*, 45(4), 1298–1306, 2011.

[160] Beyer J., Trannum H.C., Bakke T., Hodson P.V. and Collier T.K. Environmental effects of the deepwater horizon oil spill: a review. *Mar. Pollut. Bull.*, 110(1), 28–51, 2016.

[161] Bannwart A.C. Modeling aspects of oil–water core–annular flows. *J. Pet. Sci. Eng.*, 32(2-4), 127–143, 2001.

[162] Alpers W. and Hühnerfuss H. The damping of ocean waves by surface films: A new look at an old problem. *J. Geophys. Res. Oceans*, 94(C5), 6251–6265, 1989.

[163] Cheng Y., Tournadre J., Li X., Xu Q. and Chapron B. Impacts of oil spills on altimeter waveforms and radar backscatter cross section. *J. Geophys. Res. Oceans*, 122(5), 3621–3637, 2017.

[164] Li, H., Pourquie, M., Ooms, G., Henkes, R. Simulation of turbulent horizontal oil-water core-annular flow with a low-reynolds number k$-\epsilon$ model. *Int. J. Multiph. Flow*, 142, 103744, 2021.

[165] Bochio G. and Rodriguez O.M. Modeling of laminar-turbulent stratified liquid–liquid flow with entrainment. *Int. J. Multiph. Flow*, 153, 104122, 2022.

[166] Fulgosi M., Lakehal D., Banerjee S. and De Angelis V. Direct numerical simulation of turbulence in a sheared air–water flow with a deformable interface. *J. Fluid Mech.*, 482, 319–345, 2003.

[167] Scardovelli R. and Zaleski S. Direct numerical simulation of free-surface and interfacial flow. *Annu. Rev. Fluid Mech.*, 31(1), 567–603, 1999.

[168] Ahmadi S., Roccon A., Zonta F. and Soldati A. Turbulent drag reduction in channel flow with viscosity stratified fluids. *Comput. Fluids*, 176, 260–265, 2018.

[169] Von Kármán T. Mechanical similitude and turbulence. *Nachr. Ges. Wiss. Göttingen*, 1931.

[170] Kouris C. and Tsamopoulos J. Dynamics of axisymmetric core-annular flow in a straight tube. I. The more viscous fluid in the core, bamboo waves. *Phys. Fluids*, 13(4), 841–858, 2001.

[171] Mostert W., Popinet S. and Deike, L. High-resolution direct simulation of deep water breaking waves: Transition to turbulence, bubbles and droplets production. *J. Fluid Mech.*, 942, A27, 2022.

[172] Di Giorgio S., Pirozzoli S. and Iafrati A. On coherent vortical structures in wave breaking. *J. Fluid Mech.*, 947, A44, 2022.

[173] Komminaho J., Lundbladh A. and Johansson A. Very large structures in plane turbulent Couette flow. *J. Fluid Mech.*, 320, 259-285, 1996.

[174] Papavassiliou D. V. and Hanratty T. J. Interpretation of large-scale structures observed in a turbulent plane Couette flow. *Int. J. Heat Fluid Flow*, 18, 55-69, 1997.

[175] Tsukahara T., Kawamura H. and Shingai K. DNS of turbulent Couette flow with emphasis on the large-scale structure in the core region. *J. Turb.*, 7, 1–16, 2006.

[176] Avsarkisov V., Hoyas S., Oberlack M. and García-Galache J. Turbulent plane Couette flow at moderately high Reynolds number. *J. Fluid Mech.*, 751, R1, 2014.

[177] Pirozzoli S., Bernardini M. and Orlandi P. Turbulence statistics in Couette flow at high Reynolds number. *J. Fluid Mech.*, 758, 327-343, 2014.

[178] Lee M. and Moser R. Extreme-scale motions in turbulent plane Couette flows. *J. Fluid Mech.*, 842, 128-145, 2018.

[179] Villermaux E. and Bossa B. Single-drop fragmentation determines size distribution of raindrops. *Nat. Phys.*, 5, 702, 2009.

[180] Melville W. K. The Role of Surface-Wave Breaking in Air-Sea Interaction. *Annu. Rev. Fluid Mech.*, 28(1), 279-321, 1996.

[181] Deike L. Mass transfer at the ocean–atmosphere interface: the role of wave breaking, droplets, and bubbles. *Annu. Rev. Fluid Mech.*, 54, 191–224, 2022.

[182] Ling Y., Fuster D., Tryggvason G. and Zaleski S. A two-phase mixing layer between parallel gas and liquid streams: multiphase turbulence statistics and influence of interfacial instability. *J. Fluid Mech*, 859, 307, 2019.

[183] Karathanassis I. K., Koukouvinis F. P. and Gavaises M. Multiphase Phenomena in Diesel Fuel Injection Systems. *Energ. Env. Sustain.*, 2019.

[184] Gorokhovski M. and Herrmann M. Modeling primary atomization. *Annu. Rev. Fluid Mech.*, 40, 366, 2008.

[185] Bourouiba L., Dehandschoewercker E. and Bush J. W. Violent expiratory events: on coughing and sneezing. *J. Fluid Mech.*, 745, 537–563, 2014.

[186] Balachandar S., Zaleski S., Soldati A., Ahmadi G. and Bourouiba L. Host-to-host airborne transmission as a multiphase flow problem for science-based social distance guidelines. *Int. J. Multiph. Flow*, 132, 103439–103439, 2020.

[187] Wang J., Alipour M., Soligo G., Roccon A., De Paoli M., Picano F., and Soldati A. Short-range exposure to airborne virus transmission and current guidelines. *Proc. Natl. Acad. Sci. U.S.A.*, 118, e2105279118, 2021.

[188] Magar V. and Pedley T. J. Average nutrient uptake by a self-propelled unsteady squirmer. *J. Fluid Mech.*, 539, 93–112, 2005.

[189] Metselaar L., Yeomans J. M., and Doostmohammadi A. Topology and morphology of self-deforming active shells. *Phys. Rev. Lett.*, 123(20), 208001, 2019.

[190] Sander W. and Weigand B. Direct numerical simulation and analysis of instability enhancing parameters in liquid sheets at moderate Reynolds numbers. *Phys. Fluids*, 20, 053301–18, 2008.

[191] Kozul M., Costa P. S., Dawson J. R. and Brandt L. Aerodynamically driven rupture of a liquid film by turbulent shear flow. *Phys. Rev. Fluids*, 5, 124302, 2020.

[192] Lasheras J., Eastwood C., Martınez-Bazán C. and Montanes J. A review of statistical models for the break-up of an immiscible fluid immersed into a fully developed turbulent flow. *Int. J. Multiph. Flow*, 28(2), 247–278, 2002.

[193] Eastwood C. D., Armi L. and Lasheras J. The breakup of immiscible fluids in turbulent flows. *J. Fluid Mech.*, 502, 309–333, 2004.

[194] Ruiz-Rus J., Ern P., Roig V. and Martínez-Bazán C. Coalescence of bubbles in a high Reynolds number confined swarm. *J. Fluid Mech.*, 944, A13, 2022.

[195] Kolmogorov A. N. The local structure of turbulence in incompressible viscous fluid for very large Reynolds numbers. *Proc. Math. Phys. Eng. Sci.*, 434(1890), 9–13, 1991.

[196] Perlekar P., Biferale L. and Sbragaglia M. Droplet size distribution in homogeneous isotropic turbulence. *Phys. Fluids*, 065101, 1–10, 2012.

[197] Roccon A., De Paoli M., Zonta F. and Soldati A. Viscosity-modulated breakup and coalescence of large drops in bounded turbulence. *Phys. Rev. Fluids*, 2, 083603, 2017.

[198] Garrett C., Li M. and Farmer D. The Connection between Bubble Size Spectra and Energy Dissipation Rates in the Upper Ocean. *J. Phys. Oceanogr.*, 30(9), 2163–2171, 2000.

[199] Deane G. B. and Stokes M. D. Scale dependence of bubble creation mechanisms in breaking waves. *Nature*, 418, 844, 2002.

[200] Deike L., Melville W. and Popinet S. Air entrainment and bubble statistics in breaking waves. *J. Fluid Mech.*, 801, 91–129, 2016.

[201] Boyd J. Chebyshev and Fourier Spectral Methods. *Courrier Dover Publications*, 2000.